Results from the AUSTRAL Geodetic VLBI Network

A thesis submitted in fulfilment of the requirements for the degree of

Master of Science (MSc) under the supervision of

Prof Sergei Gulyaev and Dr Lucia Plank

presented at the Auckland University of Technology

School of Engineering, Computer and Mathematical Sciences

by

Jia (Vicky) Liu

Student ID: 1252372

14th December, 2016

Acknowledgements

This thesis has been made possible with help and support from many people.

My sincere thanks goes to my supervisor **Prof Sergei Gulyaev**, Director, Institute of the Radio Astronomy and Space Research (IRASR), Auckland University of Technology, who has always been there to give me advice. I am deeply grateful to him for the long discussions that helped me to sort out both technical and theoretical details of my work and all the help along the way.

I would also like to express my sincere gratitude to my supervisor **Dr Lucia Plank**, Post Doctoral Research Fellow, School of Physical Science University of Tasmania, Australia, for suggesting the topic of this thesis, teaching me how to use VieVS software, sharing her wisdom in the field of space geodesy, helping me to improve my background in this area and answering my numerous questions with patience.

I thank all the staff of IRASR, and all the staff of the Land Information New Zealand (LINZ). Without their kind endless help and generous advice, this thesis could not have been successfully conducted.

A special thank you goes to my best friend **Surabhi Date**. I want to express my very profound gratitude to her for providing me with unfailing support and continuous encouragement throughout my research period. You are the reason that I can achieve this accomplishment.

Finally, I would like to extend my thanks to my friends – the AUT City Fitness group for their joyful gatherings and moral support.

Abstract

Very Long Baseline Interferometry (VLBI) is a space geodesy technique used to determine the Celestial Reference Frame (CRF); it contributes to the definition of the Terrestrial Reference Frame (TRF) and it is the only space geodetic technique that provides the full set of Earth Orientation Parameters (EOPs), which are important for positioning and navigation on Earth and in space. Contribution of the southern hemisphere geodetic VLBI stations in the International VLBI Service for Geodesy and Astrometry (IVS) expanded significantly since the AUSTRAL VLBI program was started in 2011. The AUSTRAL geodetic VLBI network consists of five radio telescopes: WARK12M in New Zealand, three AuScope 12-m antennas (Hobart, Katherine and Yarragadee) in Australia, and HART15M in South Africa.

There are theoretical models which determine coordinates and velocities of AUSTRAL stations. However, one can expect that their accuracy is not high, because they are based on limited and sparse time series of first years of AUSTRAL observations (2012–2013 for VieTrf13 and 2012–2014 for ITRF2014-IVS). Here, I include two more years of observations (up to mid-2016) to test quality of the theoretical models of the AUSTRAL stations. The latest version Vienna VLBI Software VieVS (version 2.3) is used to process and analyse geodetic VLBI observational data from the global (IVS-R1/R4) and the regional (AUSTRAL) sessions for the period from 2012 to the mid of 2016. I find that there is discrepancy between Global Navigation Satellite Systems (GNSS) and VLBI results. In some cases,

there is indication that VLBI models need improvement.

I compute the horizontal coordinates (NEU). I find that horizontal (North and East) components are more stable (smaller errors) than the vertical (Up) component. I find that the WARK12M VLBI Up-residual shows vertical motion about -2 cm/yr. The co-located GNSS does not show noticeable motion – much less than 1 cm/yr. The local tie survey for the same period did not show distance change between GNSS and radio telescope. I conclude that the *a priori* model needs adjustment. In some cases, more obervations with the Warkworth 12-m radio telescope are required.

I calculate the velocities of VLBI and GNSS stations, and the baseline rates of change for both of VLBI and GNSS stations of the AUSTRAL array. I found that the ITRF2014 describes baseline rates of change is better than the VieTrf13. In some cases discrepancies between models and observations are significant. I conclude that the models of our AUSTRAL stations need to be adjusted.

It is the troposphere that is one of the most important error sources for space geodetic techniques which rely on radio signals (VLBI and GNSS). To achieve accuracy of telescope coordinate determination at the millimetre level, an accurate troposphere delay modelling is needed. I investigate the tropospheric zenith wet delay (ZWD) for the AUSTRAL stations. I discuss the seasonal variations (signals) of the ZWD. I compare the ZWD results obtained from VLBI with the ZWD results based on the GNSS measurements for the Warkworth Global Geodetic Observing System (GGOS) station. I find that the geodetic results for VLBI and GNSS present a good agreement. I conclude that the AUSTRAL sessions are suitable to measure ZWD.

I consider VLBI sessions which involve AUSTRAL stations only and sessions that include AUSTRAL station and other IVS stations. I compute and compare the

EOPs and demonstrate that the more stations are involved and the more regular is the distribution of IVS stations on the globe, the higher the accuracy of EOPs determined in these sessions.

Contents

"I hereby declare that this submission is my own work and that, to the best of my knowledge and belief, it contains no material previously published or written by another person (except where explicity defined in the acknowledgements), nor material which to a substantial extent has been submitted for the award of any other degree or diploma of a university or other institution of higher learning."

Jia Vicky Liu

Chapter 1

Introduction

Space geodesy is a branch of geosciences which provides in-depth study of the deformation of the Earth's crust, inter- and intra-plate tectonics, loading effects, variations in the Earth's orientation and rotation, as well as spatial and temporal variations of water vapour in the atmosphere in a 3-dimensional time varying space. It uses the space geodetic techniques, such as Very Long Baseline Interferometry (VLBI), Global Navigation Satellite Systems (GNSS), Satellite Laser Ranging (SLR) and the Doppler Orbitography and Radio-Positioning by Integrated Satellite (DORIS) (Figure 1.1).
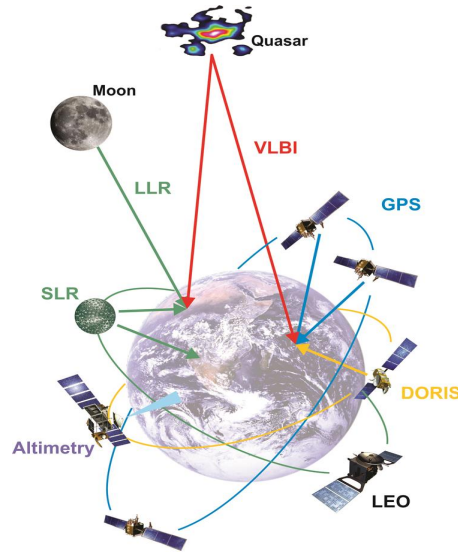
Figure 1.1: Space geodetic techniques (by courtesy of [Rothacher et al., 2010])

Over 40-years, the VLBI technique has been significantly contributing to the progress made in geodesy. VLBI measures the time difference in the arrival of microwave signals from extragalactic radio sources as received at two or more radio antennas. VLBI continuously monitors earth orientation parameters and crustal movements in order to maintain global reference frames, coordinated within the International VLBI Service for Geodesy and Astrometry (IVS). Geodetic VLBI provides an important contribution to the realization of the International Terrestrial Reference Frame (ITRF) and uniquely supports realization and maintenance of the International Celestial Reference Frame (ICRF). VLBI is the only space-geodetic technique that determine the full set of Earth Orientation Parameters (EOPs), which are needed for the transformation between the terrestrial and celestial reference frames (CRF-EOP-TRF). The VLBI technique also uniquely estimates the long-period variation in $UT1 - UTC$ and nutation parameters [Schuh and Böhm, 2013b].

Among the space geodetic techniques, GNSS also provide critical geodetic measurements and allows accurate modelling of the ITRF and tectonic plate motion and intra-plate deformation. It includes the Global Positioning System (GPS), the Russian Globalnaja Nawigazionnaja Sputnikowwaja Sistema (GLONASS), and the European Union's Galileo system, which is scheduled to be fully operational by 2020 at the earliest.

The new VLBI and GNSS networks are distributed across continental Australia in the framework of the AuScope project. AuScope is the infrastructure system – a Geoscience and Geospatial Infrastructure System that combines traditional research infrastructure with applied science infrastructure. AuScope aims to study dynamics of the Australian Tectonic Plate. According to this project approximately 100 new GNSS stations were built. Each site has one instrument package including GNSS receiver, antenna and meteorology equipment. This complements the existing Australian Regional Geodetic Network and State networks [AuScope, 2015].

New Zealand GNSS network is operated by the Land Information New Zealand (LINZ) and the Geological and Nuclear Science Research Institute (GNS Science). LINZ is responsible for land titles, geodetic and cadastral survey systems, topographic information, hydrographic information and other functions.

1.1   The AUSTRAL observing program

Since late 2011, more than 150 dedicated AUSTRAL VLBI sessions have been undertaken with the aim to strengthen the terrestrial and celestial reference frame in the southern hemisphere. Observations are made with the three 12-m antennas from the Australian AuScope array in Hobart (HOBART12), Katherine

(KATH12M) and Yarragadee (YARRA12M) observing together with the Warkworth 12-m antenna (WARK12M) in New Zealand and the new 15-m antenna (HART15M) at Hartebeesthoek in South Africa. These small and fast antennas are observed with a data rate of 1Gbps, which is four times the data rate of the usual observations within the IVS [Plank et al., 2015a].

The AUSTRAL observing program is divided into three streams focused on high priority geodetic and astrometric aims in the southern hemisphere [Lovell et al., 2013]:

1. astrometric observations to monitor and enhance the southern hemisphere reference frame in preparation for ICRF3;

2. regular observations to improve the density of the geodetic time series for the southern radio telescopes and to measure and monitor the motion and deformation of the Australian plate;

3. four 15-day CONT-like campaigns [1] sessions over two years to demonstrate the full capabilities of the array, characterize the level of systematic errors are caused by the troposphere and source structure and develop and trial error mitigation strategies. One session was held in 2013 and another in 2014, and two were scheduled for 2015.

1.2 VLBI/ GNSS co-location: Warkworth station

The WARK12M geodetic radio telescope was established by the Institute for Radio Astronomy and Space Research (IRASR) of Auckland University of Technol-

---

[1]CONT campaigns are continuous VLBI campaigns of typically 2 weeks duration which have been organised by the IVS at irregular intervals since 1994 [Plank et al., 2016].

ogy (AUT) in 2008. It is the first and only research radio telescope in New Zealand. It became an IVS station, and it is used for different VLBI sessions from the middle of 2010, mainly for the global IVS-R1/R4 sessions and later for the AUSTRAL sessions. It is aimed for radio astronomy, space geodesy, and space science (spacecraft tracking) [Gulyaev et al., 2011].

1.2.1   Technical information

The WARK12M antenna is installed near the township of Warkworth, approximately 60 km north of the city of Auckland. Table 1.1 provides the specifications of the WARK12M antenna. This 12-m antenna is operated at S-band (2.1-2.4 GHz) and X-band (8.1-9.1 GHz), equipped with an S/X dual-band dual-circular polarization feed at the secondary focus and an L-band feed at the prime focus. The telescope backend is equipped with a Digital Base Band Converter (DBBC) manufactured by the HAT-Lab, Catania, Italy. A new DBBC was received and used to replace the original one in April 2014 for the 12-m antenna. Since installation of the new DBBC on the 12-m, a significant improvement in System Equivalent Flux Density (SEFD) figures occurred: from previously 6000 Jy to now approximately 3800 Jy, comparable with the AuScope 12-m radio telescopes [Weston et al., 2014]. The data recorders used in WARK12M are Mk5B+ and Mk5C [Gulyaev et al., 2011].

Table 1.1: Specifications of the WARK12M

Antenna type:	Fully-steerable, dual-shaped Cassegrain
Manufacturer:	Cobham/Patriot, USA
Main dish diam.:	12.1 m
Secondary refl. diam.:	1.8 m
Focal length:	4.538 m
Surface accuracy:	0.35 mm
Pointing accuracy:	$18\,\mathrm{sec}$
Potential frequency range:	1.4 to 43 GHz
Mount:	alt-azimuth
Azimuth axis range:	$90° \pm 270°$
Elevation axis range:	$7.2°$ to $88°$
Azimuth axis max speed:	$5°/s$
Elevation axis max speed:	$1°/s$
Main dish F/D ratio:	0.375

1.2.2 Contribution to geodetic research

New Zealand is located on the boundary of two tectonic plates: the Australian Plate and the Pacific Plate. This geographic location makes New Zealand one of the most active geological areas in the world. Figure 1.2 shows the map of New Zealand and indicates tectonic plate motions. Generally, the Australian plate is heading north while the Pacific plate is heading west. The combination of these motions means that the tectonic plate motion in New Zealand is about 40 mm/yr in a southwest direction [Blick and Sarib, 2010]. Therefore, Christchurch is moving towards Hobart approximately 4 metres every century.

Figure 1.2: NZ geological situation (by courtesy of GNS Science [GNS, 2016])

New Zealand GNSS network is operated by the PositioNZ and the GeoNet. These two continuous networks are used to monitor New Zealand geological processes. The PositioNZ network consists of 37 reference stations which are located throughout mainland New Zealand including two stations in the Chatham Islands and three stations in Antarctica (PositioNZ) (Figure 1.3). LINZ operates the PositioNZ network, principally established to support the New Zealand Geodetic Datum 2000 (NZGD2000). The network provides GNSS carrier phase and code

range measurements in support of three dimensional positioning activities throughout New Zealand. The PositioNZ network enables users to position points with an accuracy that approaches a few centimetres relative to the NZGD2000, both horizontally and vertically. For geodetic VLBI stations operated as IVS network stations a much higher accuracy (1 mm) is expected when the VLBI Global Observing System (VGOS) is implemented [Petrachenko et al., 2013]. Warkworth GNSS station (WARK) is one of the PositioNZ network stations and one out of four IGS stations in New Zealand [Gulyaev et al., 2010].
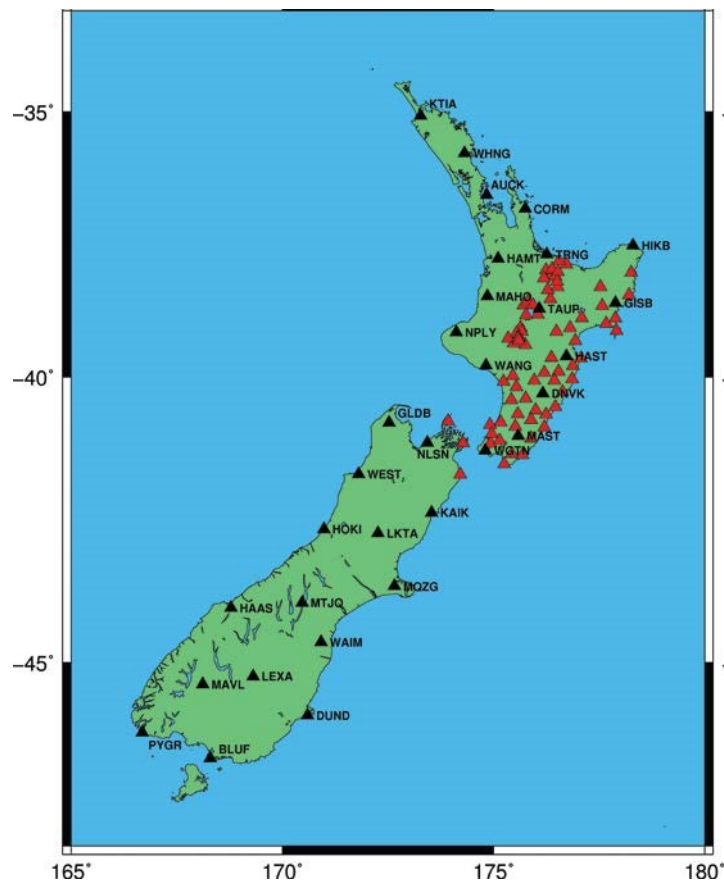

Figure 1.3: PositioNZ and GeoNet Networks (by courtesy of [Palmer, 2010])

A local tie survey conducted by LINZ determined the coordinates of the invariant point of the 12-m antenna (the interception of the azimuth and elevation) [Gulyaev

and Natusch, 2009].

$$\text{Latitude} = 36°26'\ 03.87406"\ S, \text{Longitude} = 174°39'46.00833"\ E$$

or using the geocentric coordinates:

$$X = -5115333.3149 \text{ m}, Y = 477886.8944 \text{ m}, Z = -3767147.3447 \text{ m}$$

The coordinates are given in terms of ITRF2000 at the epoch of the survey (2012). The survey was conducted in close collaboration with the New Zealand GNS Science and LINZ.

In global geodetic VLBI observations, WARK12M plays an important role in improving the geographic distribution of VLBI stations in the southern hemisphere and contributing to the definition of ICRF and ITRF. WARK12M is engaged in joint geodetic research with the National Institute of Information and Communications Technology (NICT), Japan and the AuScope project [Takiguchi et al., 2013]. As located on the Australian tectonic plate, both WARK12M and AuScope three 12-m radio telescopes are placed for measurements of intra-plate deformation. The six baselines between WARK12M and AuScope are long enough to contribute to EOPs observations [Titov et al., 2014].

1.3 AUSTRAL stations

There are three 12-m diameter AuScope VLBI observatories on the Australian continent located near Hobart (Tasmania), Yarragadee (Western Australia), and Katherine (Northern Territory). Same as Warkworth station, each AuScope VLBI radio telescope is equipped with a 12.1-m diameter main dish designed and manufactured by Cobham/Patriot, USA. Also, these three observatories have the same

technical characteristics as Warkworth station (see Table 1.1) except for fast slewing rates ($5°/s$ in azimuth and $1.25°/s$ in elevation), and acceleration of ($1.3°/s/s$) [Lovell et al., 2013]. Figure 1.4 shows four 12-m stations and their location.

Figure 1.4: Warkworth (NZ) and Auscope (Australia) VLBI array and location

South Africa is represented in the AUSTRAL network by a 15-m radio telescope which is located near Hartebeesthoek, 65 km northwest of Johannesburg. Table 1.2 contains the technical parameters of the HART15M radio telescope and Table 1.3 shows the technical parameters of the HART15M receivers [Nickola et al., 2013].

Table 1.2: HART15M radio telescope technical parameters

Parameter	HART15M
Owner and operating agency:	HartRAO
Year of construction:	2007
Radio telescope mount:	Az-El
Receiving feed:	Prime focus
Diameter of main reflector d:	15 m
Focal length f:	7.5 m
Focal ratio f/d:	0.5
Surface error of reflector (RMS):	1.6 mm
Short wavelength limit:	2 cm
Point resolution:	0.001°
Point repeatability:	0.004°
Slew rate on each axis:	Az: $2°/s$
	El: $1°/s$

Table 1.3: Parameters of HART15M co-axial receivers

Parameter	X-band	S-band
Feeds:	stepped horn	wide-angle corrugated horn
Amplifier type:	cryo HEMT [2]	cryo HEMT
$T_{sys}(K)$:	40	42
$S_{SEFD}(Jy)$:	1400	1050
Point source sensitivity (Jy/K):	35	25
3 dB beamwidth (°):	0.16	0.57

---

[2]cryogenic high-electron-mobility transistor

1.4 VLBI delay model

VLBI is a primary microwave-based technique for space geodesy that measures the difference of arrival time between at least two antennas receiving radio signals from distant extragalactic radio sources, usually a compact extragalactic object, such as quasars. The signals arrive at the Earth as plane wave fronts. The signals are reflected by the primary dish to the secondary reflector, then to the feedhorn at the focus position. Past the feed horn, the signal undergoes an initial stage of amplification, either by transistor amplifiers such as field-effect or high-electron-mobility transistors or by a traveling wave maser [Sovers et al., 1998a]. For geodetic VLBI the radio signals are split into two frequency bands, they are, S-band and X-band at which the wavelengths are 13 and 3.5 cm, respectively, and the system temperature range from 20 to 100 K for these two bands. Millimetres and picoseconds (connected by the speed of light = 299,792,458 m/s ≈ 1 mm/3 ps) and nanoradians are the most convenient units which are used in astrometric and geodetic VLBI [Böhm and Schuh, 2012]. Figure 1.5 presents a simple geometric principle of VLBI:
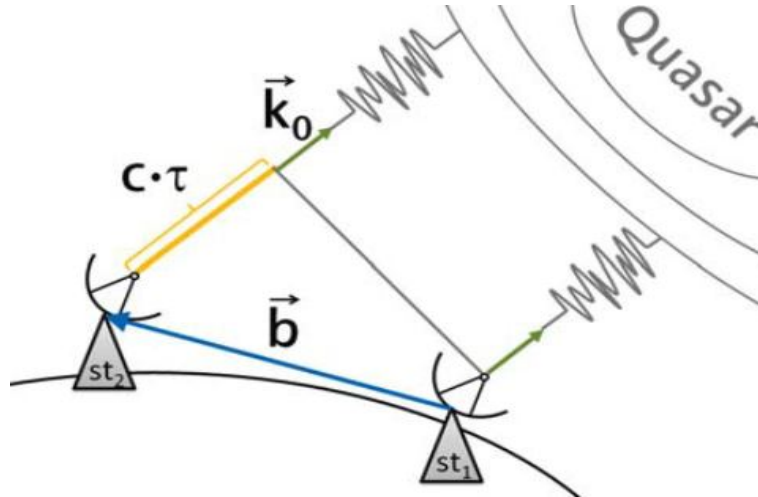

Figure 1.5: Basic geometric VLBI model (by courtesy of [Plank, 2013])

The VLBI delay model equation can be written as [Schuh and Behrend, 2012]:

$$-c \cdot \tau = \overrightarrow{b} \cdot \overrightarrow{k} + \Delta_g + \Delta_{clock} + \Delta_{trop} + \Delta_{ion} + ... \qquad (1.1)$$

the distance $c \cdot \tau$ is the projection of the baseline onto the source vector, where c is the speed of light, the time delay τ is the time difference between the radio signals arrival at station 1 and 2; $\overrightarrow{b}$ is the spatial distance of the Cartesian coordinates (baseline); $\overrightarrow{k}$ is the direction to the radio source (quasar); Δ_g is the geometric delay; Δ_{clock} is a contribution to the signal delay arising from the mis-synchronization of the reference clocks at each observatory; Δ_{trop} is the troposphere delay correction; Δ_{ion} is the ionosphere delay correction.

Two main streams in the geodetic VLBI system are shown in Figure 1.6, one containing the actual observations which experience instrumental calibration and environmental corrections (e.g., ionosphere, troposphere, source structure, thermal deformation and axis offsets) to obtain the reduced observed delay (named τ_0), the theoretically computed delay (named τ_c) is produced by the other stream, starting with the precise *a priori* values, a set of initial values for the parameters of the VLBI model [Böhm and Schuh, 2015]. The 'observed minus computed' values are formed while both streams converge at the entrance to the parameter estimation algorithm 'least-squares adjustment'.

In the Vienna VLBI Software (VieVS), geodetic parameters are estimated with the least square adjustment based on the Gauss Markov model from VLBI observations by using Continuous Piece-Wise Linear Offsets (CPWLO) functions [Böhm, 2014a].
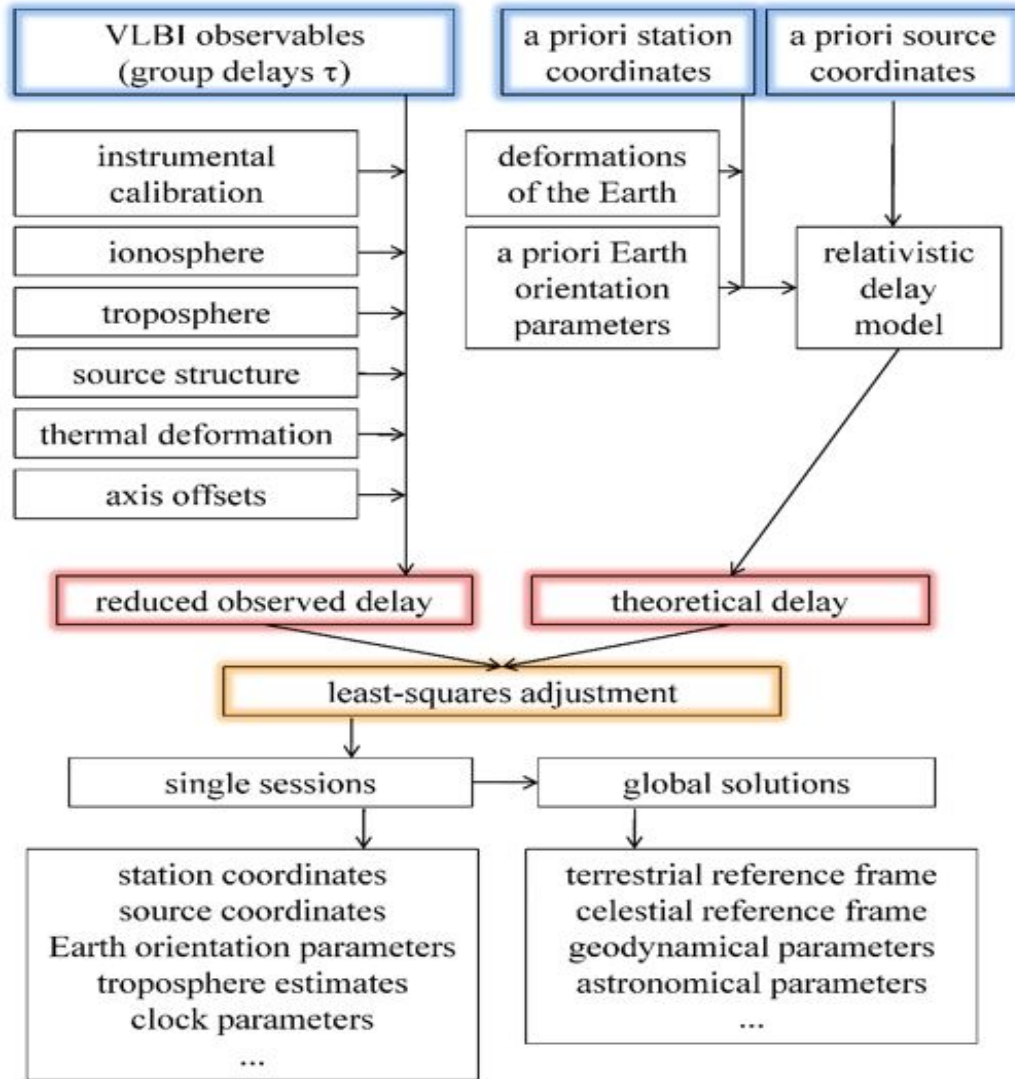
Figure 1.6: Schematic of the geodetic VLBI data analysis (by courtesy of [Böhm and Schuh, 2015])

1.5 Vienna VLBI Software (VieVS)

In this work, I use VieVS to analyse VLBI data. VieVS is a new geodetic VLBI data analysis software which has been developed and maintained by the Department of

Geodesy and Geoinformation, Vienna University of Technology since 2008 [Böhm et al., 2012]. The development of VieVS was not started from the scratch but is based on algorithms used in the OCCAM software [Titov et al., 2004]. VieVS software is designed for the analysis of geodetic VLBI observation data, for scheduling and simulating different VLBI sessions. It includes state of the art models that concur with the most recent International Earth Rotation and Reference System Service (IERS) conventions. It is written in programming language Matlab which is easy to use and the source code easy to understand and to modify [Böhm et al., 2014a].

1.5.1 The structure of VieVS

VieVS has three main structures, they are, VIE-INIT, VIE-MOD and VIE-LSM (Figure 1.7).
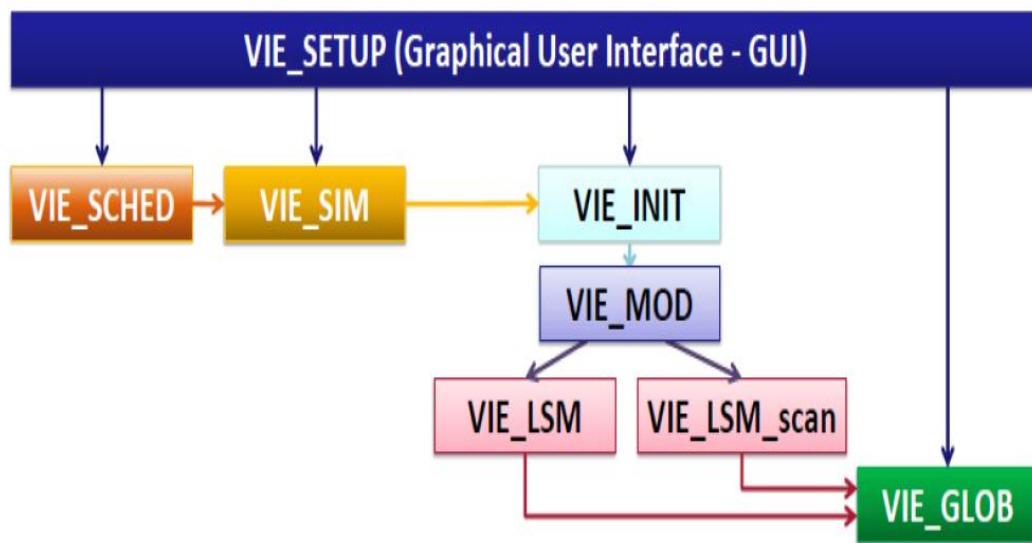

Figure 1.7: Vienna VLBI Software (VieVS) structure (by courtesy of [Böhm et al., 2014b])

VIE-INIT (where INIT represents initialising), is mainly used to read the data from the data file which has Next Generation Sequencing (NGS) extension. These data are freely available on the website http://lupus.gsfc.nasa.gov/sess/. VIE-INIT also reads station coordinates and velocities from the TRF/*superstations* file and reads source coordinates from CRF/*supersource* file. Data is stored in the LEVEL 0 folder [Kwak, 2015].

VIE-MOD (MOD denotes modelling), is used to compute the theoretical delays which include Earth Orientation Parameters such as oceanic and gravitational high frequency terms and nutation corrections, as well as solid Earth tides, troposphere delay, tidal ocean loading, thermal antenna deformation, axis offset, tidal and non-tidal atmosphere loading, as well as their partial derivatives $\frac{d\tau}{dVAR}$. Modelling is performed according to the IERS conventions. Data for VIE-MOD is created and saved in LEVEL 1 folder [Hellerschmied, 2015].

VIE-LSM (LSM indicates least squares matching), is responsible for the geodetic parameters with least squares estimation from VLBI observations. All the parameters such as EOPs (mas and ms), zenith wet delay (cm), TRF coordinates (cm), CRF coordinates (declinations in mas and right ascensions in ms) and clock offsets (cm) etc. can be estimated as Piece-Wise Linear Offsets (PWLO). They are saved in the LEVEL 3 folder for further investigation [Teke and Böhm, 2015].

Apart from three primary (main) structure modules, VieVS operates three secondary modules, namely VIE-SCHED, VIE-SIM and VIE-GLOB:

VIE-SCHED (SCHED for scheduling) is the scheduling program of VieVS. An observation plan for a specific time and network can be created by this module [Mayer, 2015].

VIE-SIM (SIM represents simulating) creates simulated observations for an observation plan. It combines the theoretical delay with simulated values for tro-

posphere Zenith Wet Delay (ZWD), station clocks and observation noise at each epoch, in order to create data that simulate realistic observations. The output is saved in the NGS-files and can then be analysed with the main VieVS methods [Plank et al., 2015b].

VIE-GLOB (GLOB denotes global) combines the normal equations of several sessions into a global solution in order to calculate reference frames (TRF and CRF) and global parameters (EOPs) using the least squares method [Krásná and Mayer, 2015].

1.5.2   VieVS Graphical User Interface (GUI)

A Graphical User Interface (GUI) for VieVS is provided by VIE-SETUP. Figure 1.8 shows the latest VieVS version graphical user interface. All the different modules are integrated in the GUI and can be easily selected with the drop down menu. The GUI can be started by typing vievs in the command window of Matlab (before start GUI, the $VieVS/WORK$ directory must be set as current directory in Matlab).
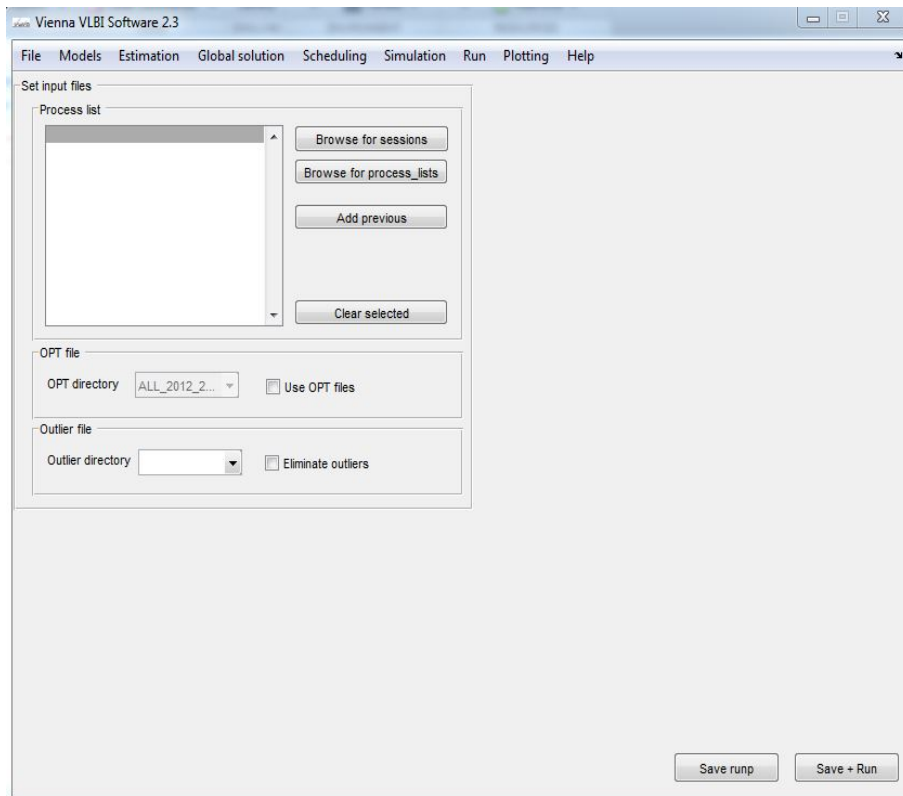
Figure 1.8: VieVS Graphical User Interface

The final purpose of the interface before processing is to save the required files at their required destination (prepare processing). Matlab allows using more than one core, so if the user needs to speed up the processing of several sessions with the same parametrization, parallel computing mode can be used (click *Run* parallel). This can be done in *Run → Run options* (Figure 1.9). Next I create subdirectories and click *Save + Run* in the GUI.
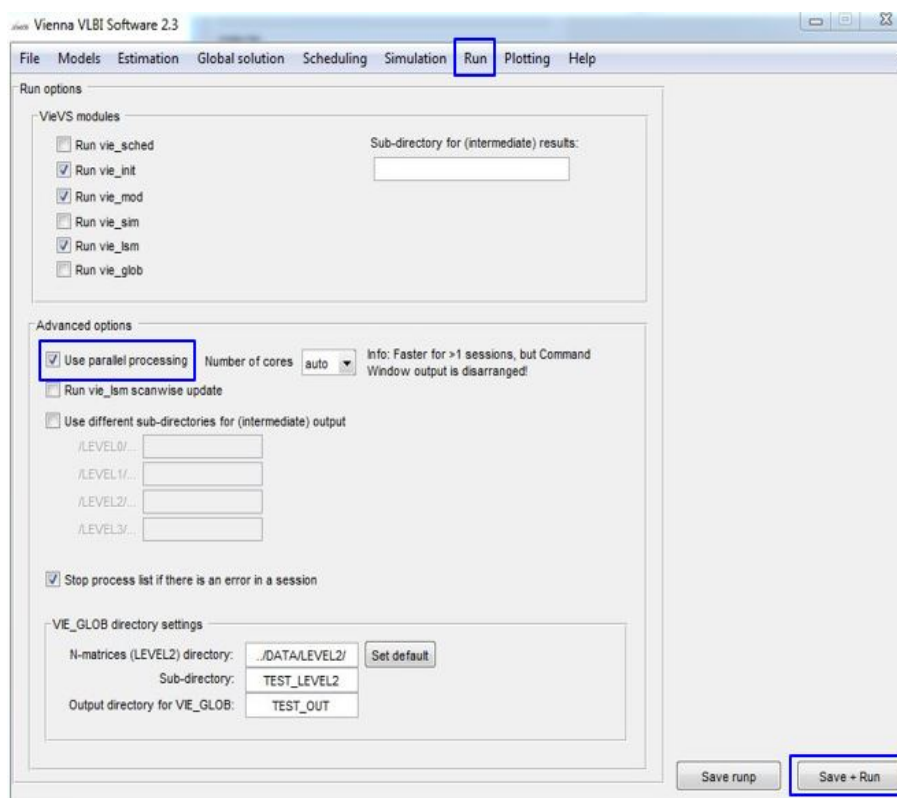
Figure 1.9: VieVS parallel computing

There are two important files: *parameter file* and *process − list*. The former is of type *.mat* which is Matlab internal binary format and it contains the VieVS processing options. This file can be used in the processing and in the interface for loading the parameters into the GUI. The latter is also a *.mat* file, which contains multiple sessions to be processed. The *process − list* is loaded by *vie − batch* and the sessions written in that file are processed. This file can be loaded and saved in the interface of VieVS.

1.6   Thesis aims and structure

The IVS relies on a global network of radio telescopes engaged in regular observations. Traditionally, the northern hemisphere is better represented in geodetic measurements than the southern hemisphere [Plank et al., 2016]. Recently, contribution of the southern hemisphere geodetic VLBI stations in the IVS expanded significantly since the AUSTRAL VLBI program started in 2011 [Plank, 2014].

The aim of this thesis is to estimate the importance and contribution of AUSTRAL geodetic VLBI network in global and regional (Australasia) space geodesy. For this reason, in this thesis I consider basic geodetic results arising from the AUSTRAL observations:

1. I test how accurate and precise are the models of the new AUSTRAL geodetic VLBI network; I compare VLBI results with analogues results from co-located GNSS stations;

2. I investigate the influence of the troposphere (tropospheric ZWD) and how accurate it can be determined in the case of VLBI and GNSS – in particular for Warkworth GGOS station;

3. I estimate the accuracy of the EOPs for the AUSTRAL geodetic VLBI network.

There is one more (rather local) aim of this work, which is important for development of space geodesy research at AUT. The AUT's Warkworth Radio Astronomical Observatory is one of the IVS network station, it participates in IVS and AUSTRAL observations on a regular basis. However, AUT has never been involved in processing IVS or AUSTRAL data. It is important, therefore, for AUT, IRASR and Warkworth Observatory to get engaged in processing and analysis of geodetic (space geodesy – VLBI and GNSS) data.

In this thesis I use a geodetic VLBI software, VieVS, introduced by the Geodepartment in the Viena University of Technology. I use the latest version of VieVS (version 2.3) with Matlab to process and analyse geodetic VLBI data from global IVS-R1/R4 and AUSTRAL sessions. In particular, I work with data for the array of five stations: WARK12M in New Zealand; HOBART12, KATH12M and YARRA12M in Australia as well as HART15M in South Africa, overall ten baselines, for the period from 2012 to mid 2016.

In Chapter 2, I determine geocentric coordinates of five AUSTRAL stations using VieVS. From the whole set of global geodetic VLBI data, I extract VLBI sessions where AUSTRAL stations participated. I compute geocentric (XYZ) and local horizontal (NEU) coordinates of AUSTRAL stations and plot time series of these coordinates for the period of study. I study specifically the behaviour of NEU residuals for Warkworth GGOS station. In addition, I compute the ITRF2014 velocities of VLBI stations and co-located GNSS stations. Using station velocities and coordinates, I study baselines and their rates of change for the AUSTRAL array. I compare rates of change of VLBI baselines – for both theoretical and observed – and baselines formed by co-located GNSS stations.

In Chapter 3, I deal with the AUSTRAL and the IVS measurements of atmospheric (tropospheric) delays. I expect that AUSTRAL provides higher accuracy, as I have much more observations per time unit than in the IVS sessions [Plank et al., 2016]. I start from a brief introduction of troposphere parameters (mainly ZWD), Vienna Mapping Function 1 (VMF1), and tropospheric horizontal gradients. I investigate the tropospheric ZWD for 5 AUSTRAL stations. Particularly, I focus on the Warkworth GGOS station. I randomly choose several 24-hour sessions; I compute and compare the ZWD results obtained with VLBI techniques vs. the ZWD results based on the GNSS measurements with time interval of 60 minutes at same dates. I discuss seasonal variations of the ZWD.

In Chapter 4, I estimate the accuracy of the EOPs that can be derived from the AUSTRAL VLBI stations. I compute and plot the EOPs residuals for the AUSTRAL sessions, as well as for the IVS-R1/R4 sessions where the AUSTRAL stations participated in the period from 2012-2016. Parameter $dUT1$, the difference between time defined from the Earth rotation and atomic time, is a very important EOPs. It is used to correct GNSS orbits and it is uniquely determined by VLBI technique. In Chapter 4, I investigate whether the AUSTRAL network can be used for rapid measurements of $dUT1$. I fix the polar motion and calculate the errors of the $dUT1$ for both the AUSTRAL sessions and the IVS-R1/R4 sessions and compare them.

Finally, Chapter 5 summarizes our results, gives conclusions and discusses possible future work.

Chapter 2

AUSTRAL stations: geographic coordinates, velocities and baselines

To specify the position of points on the Earth's surface or in space is a complicated process due to many factors, such as relativity theory, forces acting on the satellite, the atmosphere, Earth rotation, solid Earth and ocean tides and tectonic motions, etc. The Earth is constantly changing shape and it is in motion around the sun, the so-called fixed stars are not fixed in space but are also in motion at any point in time. The Earth has an instantaneous astronomic axis of rotation, an instantaneous astronomic equator, and an instantaneous astronomic meridian. Hence, a well-defined spatial reference frame is necessary to create accurate maps. It defines the coordinate system and datum in which all landmarks have unique coordinates. A Terrestrial Reference Frame (TRF) provides a set of coordinates of radio telescopes located on the Earth's surface. It can be used to measure tectonic plates and regional subsidence. Also, it is used to represent the Earth when measuring its rotation in space. This rotation is measured with respect to a frame

tied to distant quasar, called a Celestial Reference Frame (CRF). The realization of reference frames is one of the main responsibilities of geodesy, it is the platform of all kind of measurements around the Earth.

2.1 Geodetic reference frames

Geodetic reference frames are the basis for the tri-dimensional (space), time-dependent positioning in global, regional and national geodetic networks, for spatial applications such as the geodetic cadastre, engineering construction, precise navigation, geo-information acquisition, geodynamics, sea level and other geoscientific studies. They are necessary to consistently reference or tag parameters using geodetic observations, such as, station coordinates, crustal motion, Earth orientation information, etc. Ground observations of GNSS and other satellites, or radio telescope observations of distant quasars, enable us to realize the reference frame and to derive other parameters, for example [GGOS, 2011]:

Crustal motions: The long-term changes in coordinates can be derived by estimating the coordinates of continuously operating GNSS reference stations. As these are caused by the tectonic plates' motion, therefore, by monitoring these ground reference stations, the velocities of the tectonic plates can be estimated.

Earth Orientation Parameters: reference frames are essential for the determination of parameters, for example, the direction of the Earth's rotation axis, the Earth's rotational velocity and its variation.

Geocentric Motion: an origin is needed for a reference frame. This is typically taken to be at the centre of mass of the Earth, however the location of this origin relative to the solid Earth is not constant. The geocentric motion with respect to the Earth surface is monitored by the satellite techniques.

2.1.1 Conventional Terrestrial Reference Systems and Frames

The International Terrestrial Reference System (ITRS) is a global spatial reference system, adopted by the International Union of Geodesy and Geophysics (IUGG) in Vienna, 1991 [Petit and Luzum, 2013a]. The ITRS is co-rotating with the Earth in its diurnal motion in space. Station coordinates have small temporal variations with time caused by geophysical effects. The ITRS origin being the Earth's center of mass (including oceans and atmosphere), the unit of length is the meter. The orientation is equatorial as the Z-axis points to the Earth rotation axis and X-axis is identical to the direction of Greenwich mean meridian and adopted by BIH (Bureau International de l'Heure – The International Time Bureau) at the epoch 1984.0 (Figure 2.1) [Petit and Luzum, 2010b]:
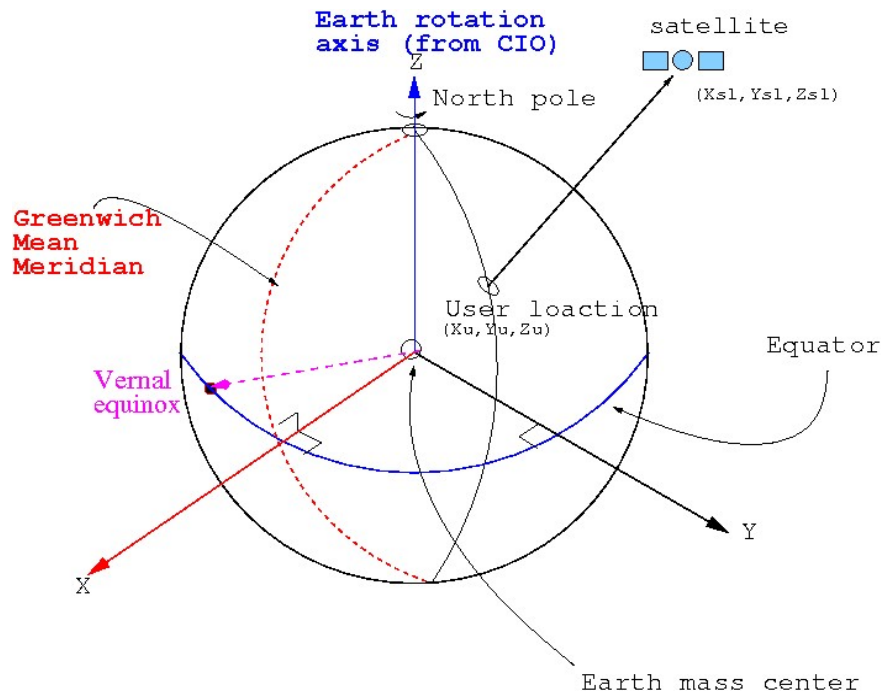

Figure 2.1: Terrestrial Reference System (TRS) (by courtesy of [Subirana et al., 2011a])

X: is the intersection between the equatorial plane and Greenwich mean meridian;

Y: is orthogonal to the X- and Z-axis, which creates a right-handed Cartesian coordinate system;

Z: is coincident with the Earth's rotational axis with direction towards the Celestial Intermediate Origin (CIO) [Szabova and Duchon, 2016].

The ITRF is a realization of the ITRS. It provides a set of precise coordinates of geodetic stations located on the Earth's surface. Since 1988, twelve ITRF versions have been produced, the ITRF2014 is the latest realization of the ITRF. For ITRF construction, time series and EOPs of different space geodetic techniques are used as input data [Altamimi et al., 2016].

In the past, in ITRF88 and ITRF89 realizations, constant positions were used as the models. The linear motion was incorporated in later as conventional corrections derived from a tectonic plate motion model.

The modern ITRF is modelled linearly. In the ITRF, there are XYZ coordinates $(\overrightarrow{X_0})$ at a reference epoch t_0 and their velocities $\dot{\overrightarrow{X}}$. To get a station position, one has to apply as:

$$\overrightarrow{X}(t) = \overrightarrow{X_0} + \dot{\overrightarrow{X}} \cdot (t - t_0) \tag{2.1}$$

These coordinates are calculated for regularized positions to remove high frequency time variations. To obtain positions for a given moment of time with higher accuracy, $\sum_i \Delta \overrightarrow{X}_i(t)$ have to be added to remove high frequency time variations. Therefore, a station position at an epoch t with the current ITRF model is expressed as [Petit and Luzum, 2010b]:

$$\overrightarrow{X}(t) = \overrightarrow{X_0} + \dot{\overrightarrow{X}} \cdot (t - t_0) + \sum_i \Delta \overrightarrow{X}_i(t) \tag{2.2}$$

It is important to note that there are non-linear variations of station coordinates and baselines. For example, seasonal station variations are not taken into account in the linear model. One can study non-linear variations after the linear component of the model is removed from observational data [Petit and Luzum, 2010b].

2.1.2   Conventional Celestial Reference Systems and Frames

The International Celestial Reference System (ICRS) was prepared by the IERS and was adopted by the International Astronomical Union (IAU) General Assembly in 1997 (23rd IAU GA, Resol. B2). ICRS is a barycentric system, with the axes non-rotating with respect to the extragalactic sources, mainly quasars. It is used to define the positions of the Earth, seven planets and other astronomical objects. The IAU recommends that the principle plane of the ICRS is as close as possible to the mean equator and the origin of right ascension should be close to the dynamical equinox, both at J2000.0. The second realization of the ICRF provides the most precise access to the ICRS in radio wavelengths, which was constructed in 2009. It contains accurate positions of 3414 compact extragalactic radio sources, including 295 new defining sources. The noise floor is found to be approximately 40 micro-arc-seconds (μas) and the axes stability of about 10 micro-arc-seconds (μas). The IERS EOPs provide the tie of the ICRF to the ITRF with an accuracy of $\pm$ 0.1 mas daily. The other ties are established by differential VLBI observations of solar system probes, galactic stars relative to quasars and other astrometry projects [Petit and Luzum, 2010a].

A next realisation of the ICRF (ICRF-3) is in preparation, it was reported in the IAU GA XXIX in 2015, and it will be introduced in 2018 [Jacobs et al., 2013].

2.2 Local NEU (North, East, Up) coordinate system

A local *NEU* (North, East, Up) coordinate system is far more intuitive and practical than geodetic Earth Center Earth Fixed (ECEF) X, Y, Z coordinates. The local *NEU* coordinates are formed from a plane tangent to the Earth's surface fixed to a specific location, therefore, it is known as a Local Tangent or local geodetic plane. By convention, the East axis is labelled X, the North axis is represented by Y and the Up axis is described by Z (Figure 2.2).
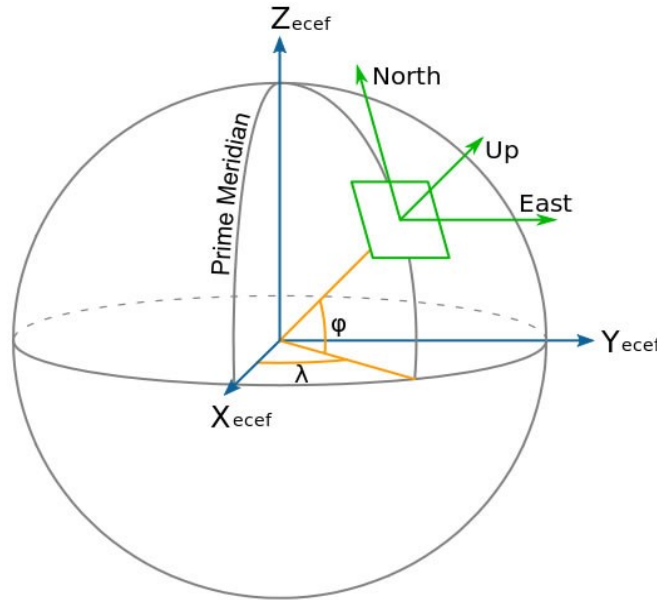
Figure 2.2: Geodetic, ECEF and NEU coordinate systems (by courtesy of [Cai et al., 2011]). See description in the text.

To convert geocentric coordinates $(X,\ Y,\ Z)$ into local horizontal coordinates (NEU – North, East, Up), the simplest way is to multiply with the rotation

matrix $R(\lambda, \varphi)$ (Equation (2.3)) [Subirana et al., 2011b]:

$$
\begin{pmatrix} E \\ N \\ U \end{pmatrix} = R(\lambda, \varphi) \cdot \begin{pmatrix} X \\ Y \\ Z \end{pmatrix}
\tag{2.3}
$$

where, λ denotes longitude, φ presents latitude.

The rotation matrix $R(\lambda, \varphi)$ in transformation matrix Equation (2.3) is the transpose of matrix:

$$
R(\lambda, \varphi) = \begin{pmatrix} -\sin\lambda & \cos\lambda & 0 \\ -\cos\lambda\sin\varphi & -\sin\lambda\sin\varphi & \cos\varphi \\ \cos\lambda\cos\varphi & \sin\lambda\cos\varphi & \sin\varphi \end{pmatrix}
\tag{2.4}
$$

where, the three rows are the unit vectors E, N and U in ECEF coordinates.

2.3 Computing geographic locations

Model (*a priori*) coordinates $(XYZ)_{mod}$ and model (*a priori*) velocities $(V_X V_Y V_Z)_{mod}$ are extracted from the Vienna Terrestrial Reference Frame (VieTrf13) [Kásná et al., 2014]. It is saved in VieVS TRF superstation file. They are presented for the epoch of $JD = 2451544.5$ (year 2000.0) in Table 2.1.

Table 2.1: The VieTrf13 model (*a priori*) geocentric coordinates and model (*a priori*) velocities at the epoch of 2000.0.

Stations	Model geocentric coordinates, m			Model velocities, m/yr			Standard deviation, m/yr		
	X	Y	Z	V_X	V_Y	V_Z	σ_{V_X}	σ_{V_Y}	σ_{V_Z}
WARK12M	-5115323.9690	477843.2660	-3767193.0945	-0.0351	0.0022	0.0199	0.0021	0.0008	0.0016
HOBART12	-3949990.2843	2522421.1037	-4311708.5713	-0.0383	0.0083	0.0414	0.0001	0.0001	0.0001
YARRA12M	-2388895.4227	5043349.7808	-3078591.4047	-0.0535	0.0164	0.0427	0.0007	0.0010	0.0008
KATH12M	-4147354.0879	4581542.4894	-1573303.9497	-0.0422	-0.0074	0.0567	0.0007	0.0007	0.0005
HART15M	5085490.8195	2668161.2328	-2768692.8349	-0.0003	0.0192	0.0167	0.0001	0.0001	0.0000

Using VieVS, I processed observational data for five stations listed in Table 2.1 and found observational values of XYZ coordinates. Using computed $(XYZ)_{obs}$ and model values (VieTrf13) calculated for appropriate dates, I found residuals $\Delta(XYZ)=(XYZ)_{obs}-(XYZ)_{mod}$ and their errors $\sigma(XYZ)$. I plotted coordinate residuals ΔX, ΔY, ΔZ and their errors (Figures 2.3–2.7).

Based on Equations (2.3) and (2.4), I converted geocentric coordinates (XYZ) to local horizontal coordinates (NEU). The transformation between geocentric coordinate residuals and local horizontal residuals is presented in matrix form as:

$$\begin{pmatrix} \Delta E \\ \Delta N \\ \Delta U \end{pmatrix} = \begin{pmatrix} -\sin\lambda & \cos\lambda & 0 \\ -\cos\lambda\sin\varphi & -\sin\lambda\sin\varphi & \cos\varphi \\ \cos\lambda\cos\varphi & \sin\lambda\cos\varphi & \sin\varphi \end{pmatrix} \cdot \begin{pmatrix} \Delta X \\ \Delta Y \\ \Delta Z \end{pmatrix} \qquad (2.5)$$

which is equivalent to:

$$\Delta E = (-\sin\lambda) \cdot \Delta X + (\cos\lambda) \cdot \Delta Y + 0 \cdot \Delta Z \qquad (2.6)$$

$$\Delta N = (-\cos\lambda\sin\varphi) \cdot \Delta X + (-\sin\lambda\sin\varphi) \cdot \Delta Y + (\cos\varphi) \cdot \Delta Z \qquad (2.7)$$

$$\Delta U = (\cos\lambda\cos\varphi) \cdot \Delta X + (\sin\lambda\cos\varphi) \cdot \Delta Y + \sin\varphi \cdot \Delta Z \qquad (2.8)$$

2.3.1 Error propagation for XYZ to NEU transformation

Geocentric coordinates (XYZ) and their residuals $(\Delta X, \Delta Y$ and $\Delta Z)$ are determined with corresponding standard deviations σ_X, σ_Y and σ_Z. The North, East and Up (NEU) components contain the uncertainties/standard deviations $(\sigma_E, \sigma_N$ and $\sigma_U)$. The standard deviations are computed by applying the error propagation rule in order to get accurate NEU components.

Assume a function of 3 variables, $f = f(x, y, z)$, each variable is determined with uncertainties $(x \pm \sigma_x, y \pm \sigma_y, z \pm \sigma_z)$, the uncertainty of f is given by:

$$\sigma_f = \sqrt{(\sigma_x)^2 \cdot \left(\frac{\partial f}{\partial x}\right)^2 + (\sigma_y)^2 \cdot \left(\frac{\partial f}{\partial y}\right)^2 + (\sigma_z)^2 \cdot \left(\frac{\partial f}{\partial z}\right)^2} \qquad (2.9)$$

Applying this general error propagation rule to Equations (2.6)–(2.8), I get:

$$\sigma_E = \sqrt{[(-\sin\lambda)\cdot\sigma_X]^2 + (\cos\lambda\cdot\sigma_Y)^2} \tag{2.10}$$

$$\sigma_N = \sqrt{[(-\cos\lambda\sin\varphi)\cdot\sigma_X]^2 + [(-\sin\lambda\sin\varphi)\cdot\sigma_Y]^2 + [(\cos\varphi)\cdot\sigma_Z]^2} \tag{2.11}$$

$$\sigma_U = \sqrt{[(\cos\lambda\cos\varphi)\cdot\sigma_X]^2 + [(\sin\lambda\cos\varphi)\cdot\sigma_Y]^2 + [(\sin\varphi)\cdot\sigma_Z]^2} \tag{2.12}$$

In this thesis, I use the data from 124 AUSTRAL sessions, 176 IVS-R1 sessions and 154 IVS-R4 sessions. These VLBI observational data are stored in the NGS files as the main input file and are analysed using the latest VieVS software (version 2.3). These files are pre-processed, which means the data are already correlated, fringe fitting was done, both S- and X- bands are combined for group delays as well as ambiguities have been resolved. I processed regional sessions and IVS R-sessions from 2012 to the mid of 2016.

The IVS-R1/R4 and AUSTRAL session results for XYZ and NEU coordinates of WARK12M, HOBART12, YARRA12M, KATH12M and HART15M are displayed in Figures 2.3–2.7. Three plots on the left side of each figure show residuals of geocentric X, Y and Z coordinates, that is the difference between the measured and model coordinates.

The right side plots of each figure shows residuals for North, East, Up (NEU) components of VLBI station position as a function of time. The data are provided for five stations both in IVS-R1/R4 and AUSTRAL sessions from 2012 to 2016. The y-axis values in the plots are in centimetres.

From Figures 2.3–2.7 I can see that data from IVS-R1/R4 and AUSTRAL sessions are complementary to each other and they have similar errors. For example, in Figure 2.8, HOBART12 Up residuals, dispersion (WRMS with 1σ) for IVS-R1 is 0.30 ± 0.18 cm/yr, it is -0.19 ± 0.15 cm/yr for IVS-R4 sessions and 0.11 ± 0.24cm/yr

for AUSTRAL. Horizontal (East and North) positions of stations are more stable than vertical (Up) positions, variations of Up are more than 2 times greater than for East and North. For example, for HOBART12, the WRMS in East and North residuals are 0.05 ± 0.03 cm/yr and -0.12 ± 0.04 cm/yr, while the WRMS for Up is 0.27 ± 0.11 cm/yr (Figure 2.9).
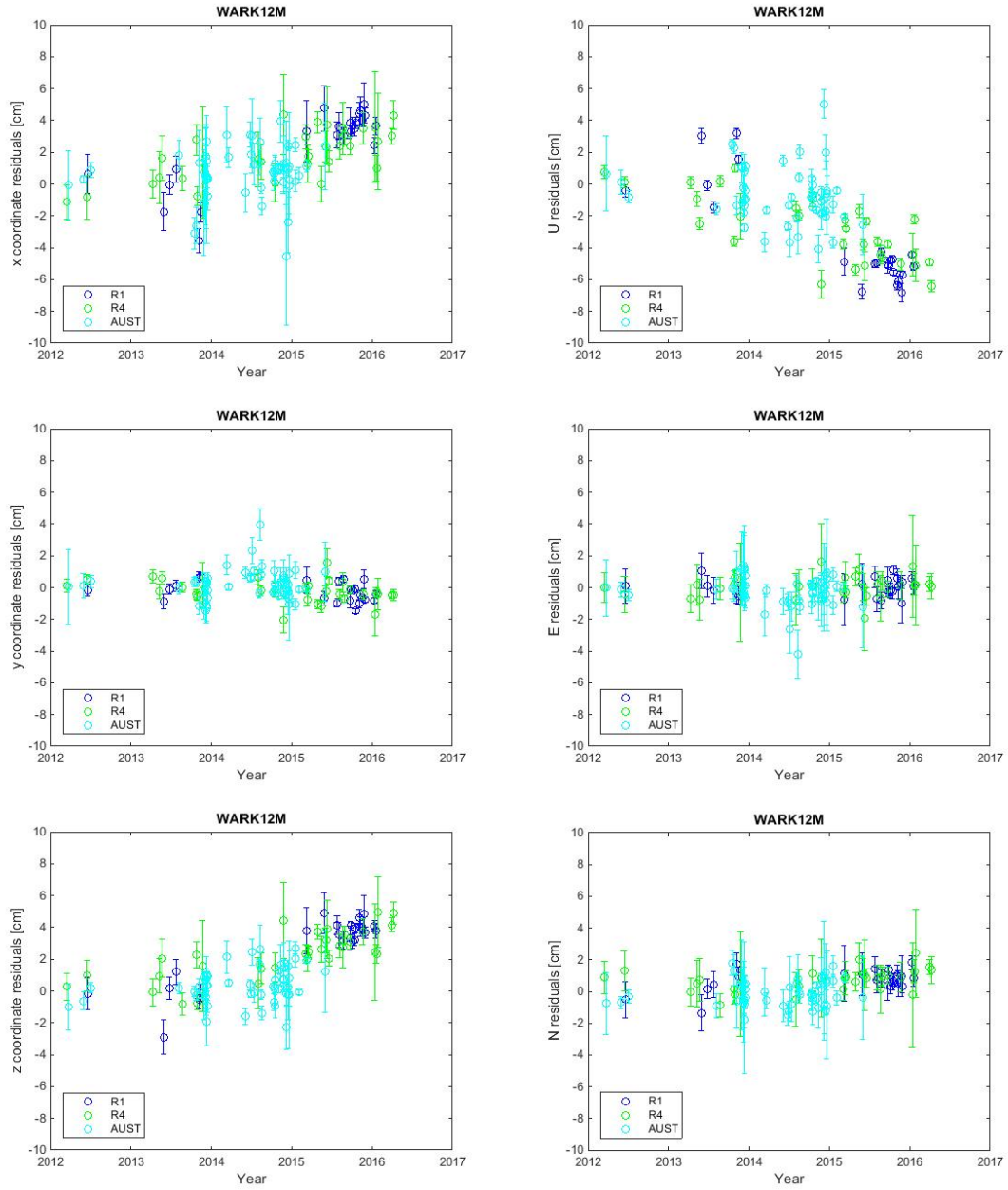
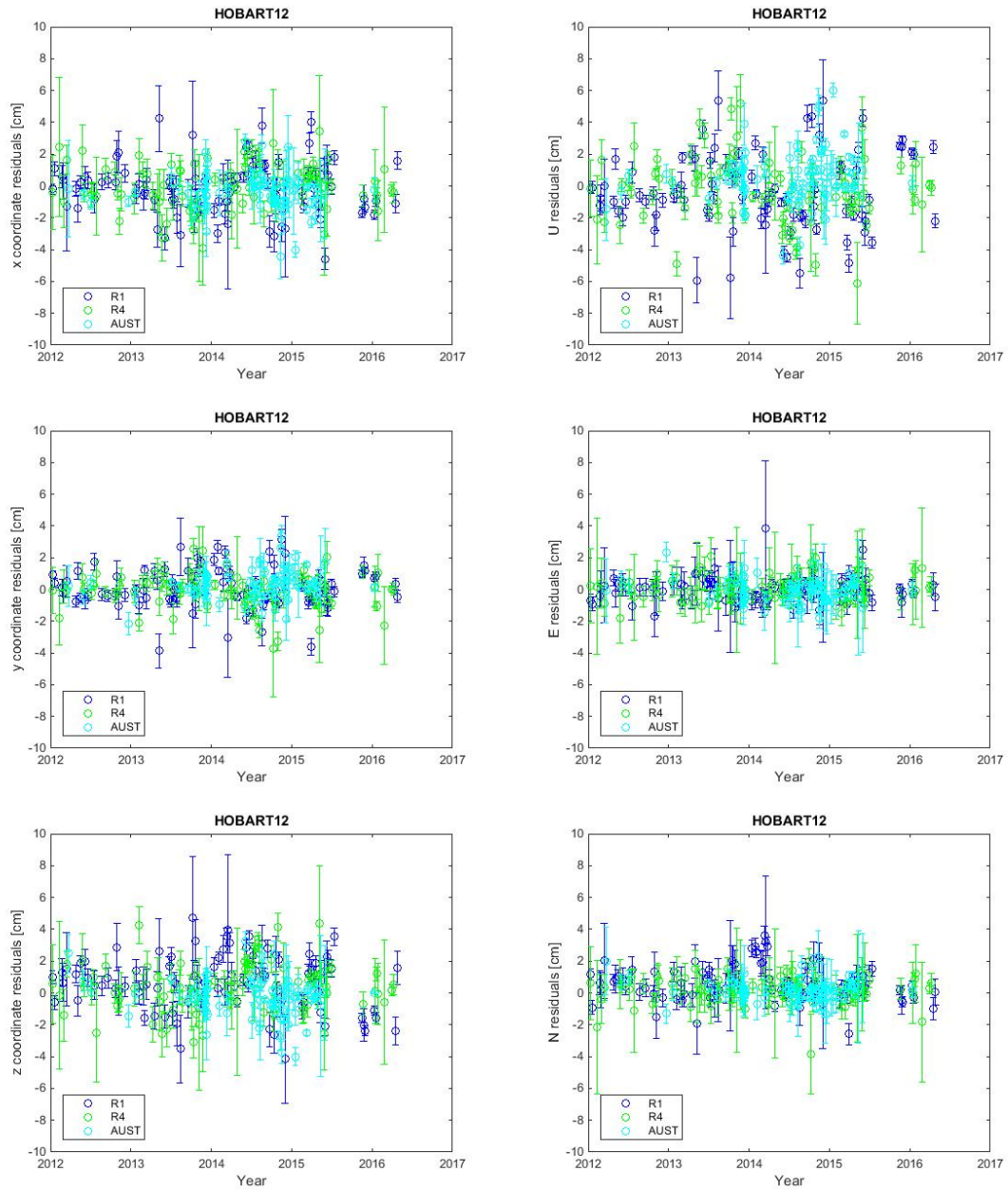Figure 2.3: Geocentric Coordinate Residuals (left column) and Local Horizontal Residuals (right column) for WARK12M

Figure 2.4: Geocentric Coordinate Residuals (left column) and Local Horizontal Residuals (right column) for HOBART12
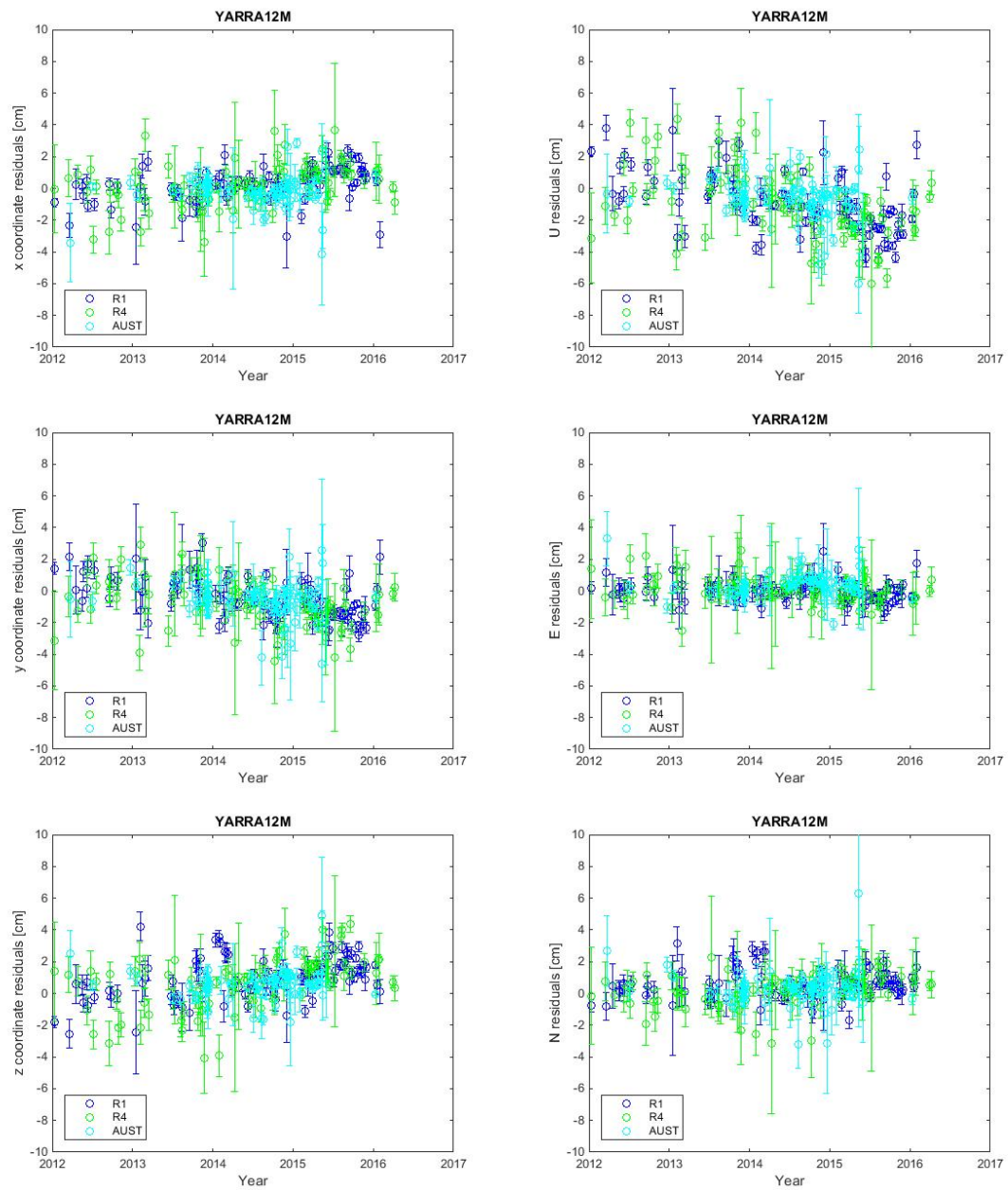
Figure 2.5: Geocentric Coordinate Residuals (left column) and Local Horizontal Residuals (right column) for YARRA12M
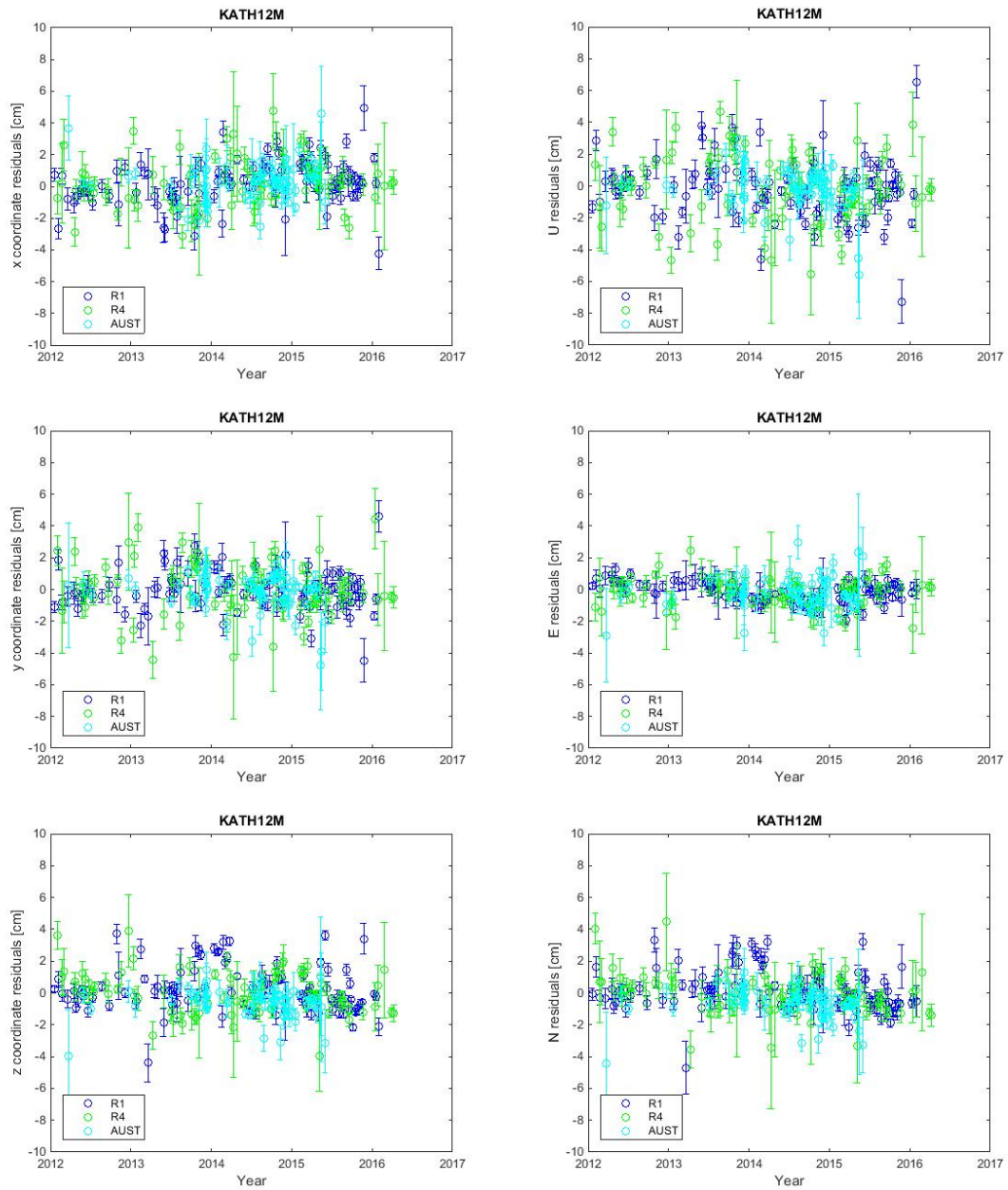
Figure 2.6: Geocentric Coordinate Residuals (left column) and Local Horizontal Residuals (right column) for KATH12M
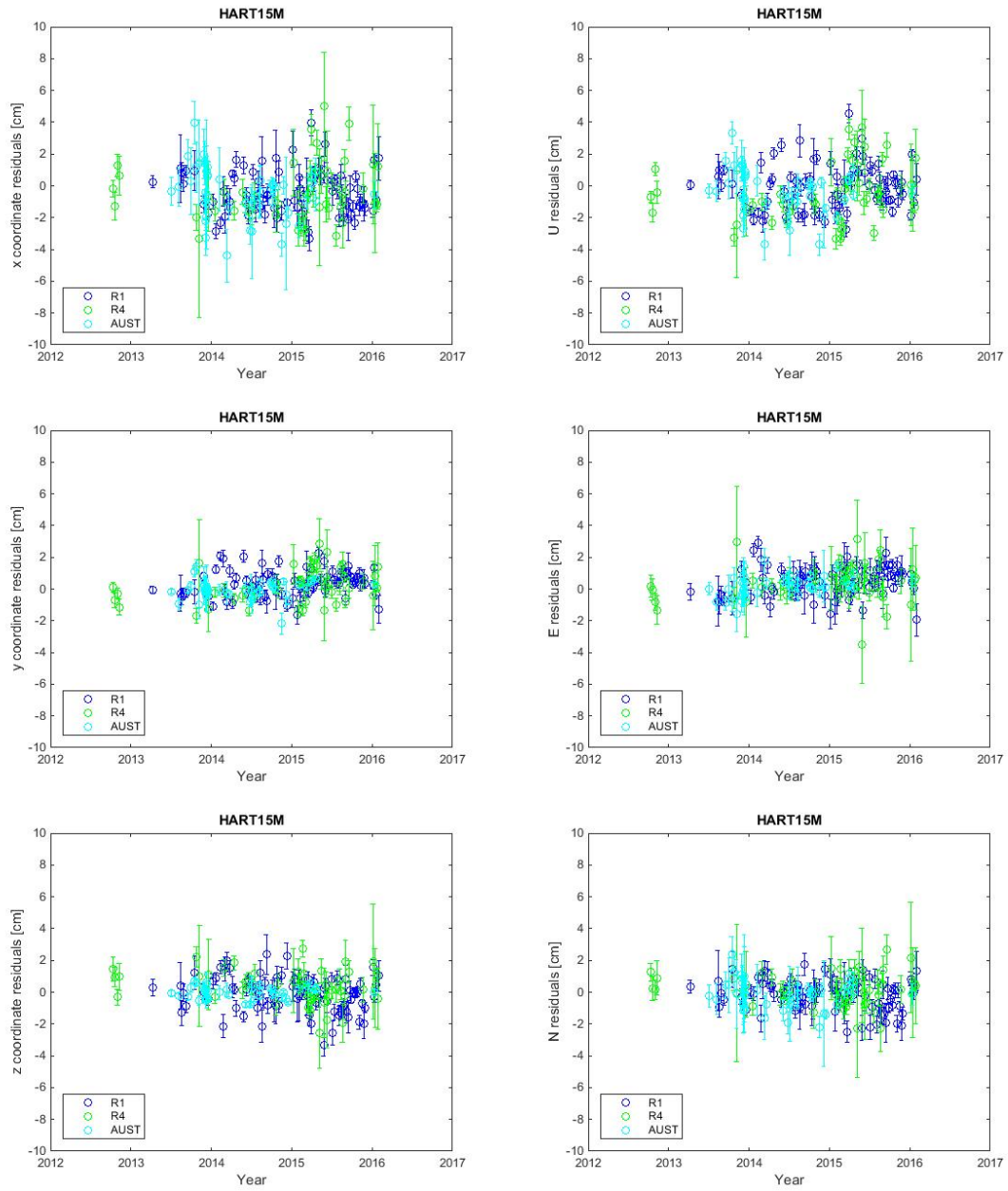
Figure 2.7: Geocentric Coordinate Residuals (left column) and Local Horizontal Residuals (right column) for HART15M
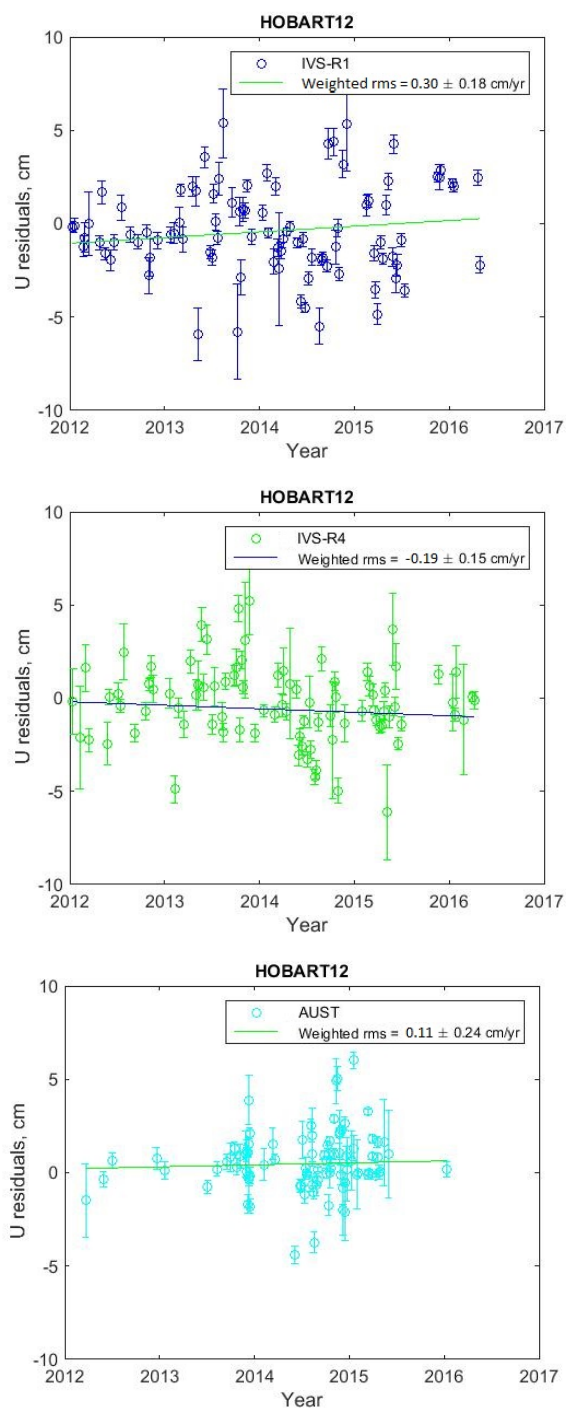
Figure 2.8: HOBART12 Local Horizontal Up Residuals WRMS for IVS-R1/R4 and AUSTRAL
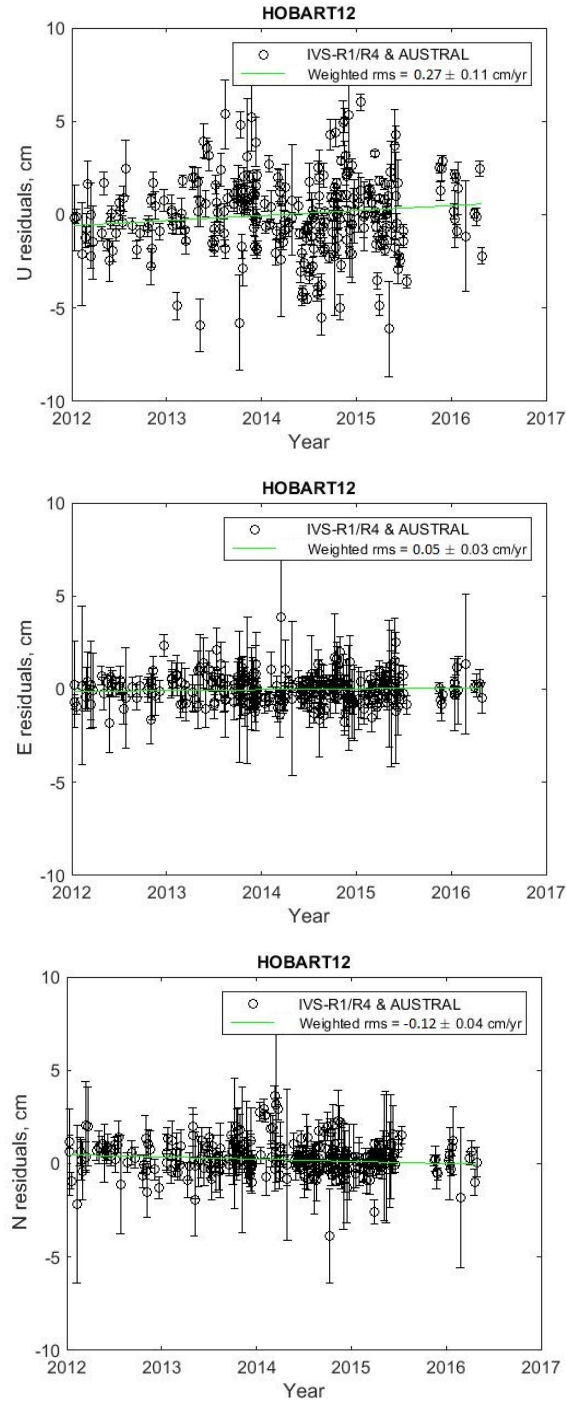
Figure 2.9: Local Horizontal Residuals WRMS for HOBART12 from 2012-2017. The observational VLBI data (IVS-R1/R4 and AUSTRAL) are extracted from VieTrf13 which are presented by black circle, the WRMS are displayed by green line
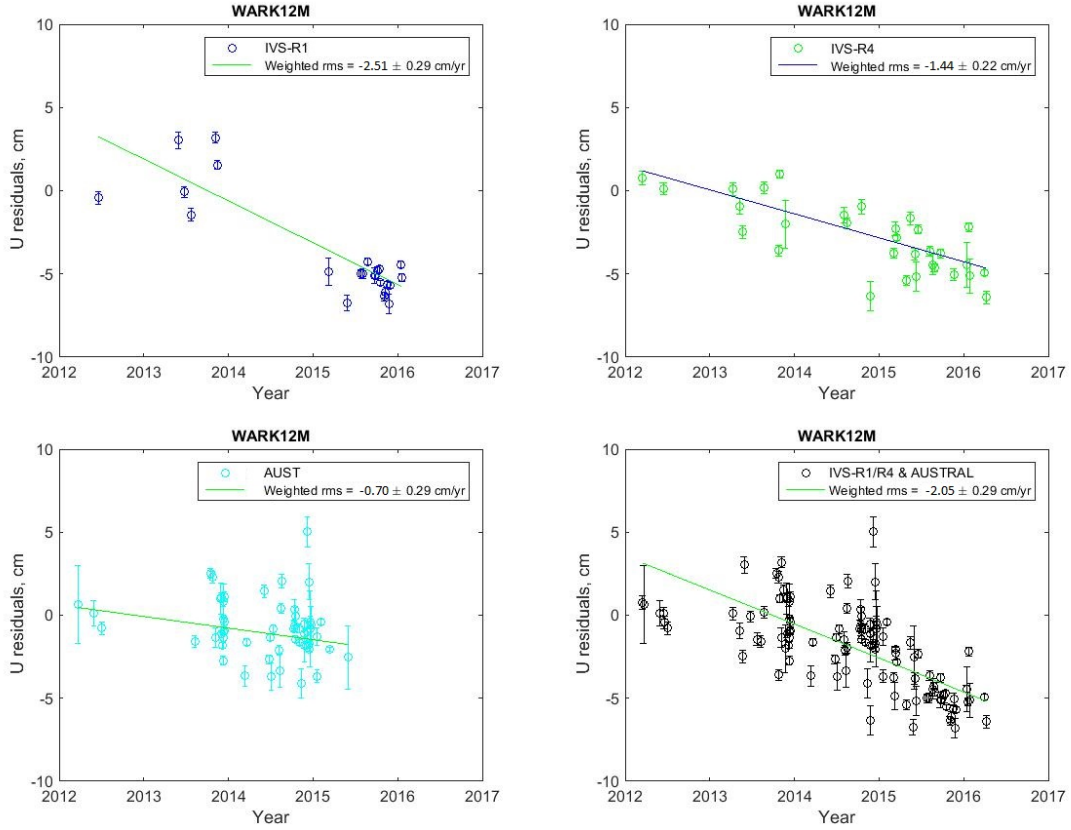
Figure 2.10: WARK12M Local Horizontal Up Residuals WRMS for IVS-R1/R4 and AUSTRAL

I studied specifically the behavior of Up residuals for Warkworth station. I plotted Up residuals and weighted least squares regression (WRMS with linear trend) for WARK12M for IVS-R1/R4 sessions, AUSTRAL sessions and all sessions in Figure 2.10. IVS-R1 sessions show significant decrease trend from mid 2012 to 2016 by -2.51 ± 0.29 cm/yr, however, there is a gap in 2014 and scatter in 2013 is large, so I cannot make a certain conclusion whether it is a jump or a slope. IVS-R4 shows Up residuals with linear trend of -1.44 ± 0.22 cm/yr. the slope for AUSTRAL sessions shows data is just -0.70 ± 0.29 cm/yr during the period from 2012 to mid

2016. However AUSTRAL data stopped at the mid 2016, so I do not have enough evidence to suggest that AUSTRAL sessions demonstrate the significant slope or not, compared to IVS-R1/R4 sessions, which continued further. I combined IVS-R1/R4 sessions and AUSTRAL sessions and computed WRMS, I can see that combined sessions data at WARK12M residual for the Up component changing at the rate of $\sim -2.05 \pm 0.29$ cm/yr. The dense time series also reveals a sudden subsidence of about -2 cm in the Up-component of WARK12M at the beginning of 2015 [Plank et al., 2016].

Does this rapid change of the Up residuals tell us about real vertical motion of WARK12M station? Or the theoretical (model) velocities for WARK12M are incorrect? Figure 2.11 shows Up displacement of the co-located GNSS WARK station with respect to its initial (2009) poition. The WARK vertical component shows annual oscillations with amplitude of ~ 10 mm. However, it does not show a noticeable systematic motion. The local tie surveys performed by LINZ in 2012 and 2016 do not show any noticeable motion of the WARK12M radio telescope with respect to the WARK GNSS station. From stability of GNSS station location and stability of radio telescope with respect to GNSS station (local tie surveys), I can conclude that a possible explanation of ~ -2 cm/yr residual is that the theoretical velocities for WARK12M might be incorrect.
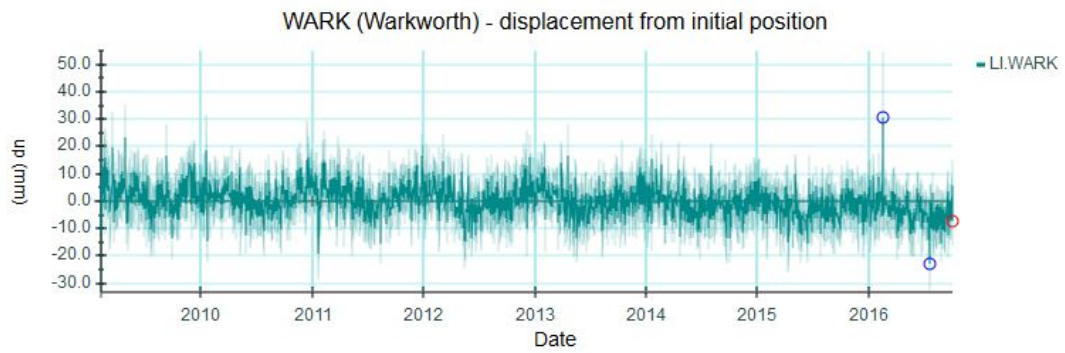
Figure 2.11: WARK Up coordinates time series based on GNSS data (by courtesy of [Gentle, 2016])

2.4 Velocities of VLBI and GNSS stations

To continue comparison between two geodetic techniques – VLBI and GNSS, I find rates of change for baseline lengths. I take *a priori* coordinates and velocities from the (preliminary) technique-specific (either VLBI or GNSS) solutions. I compare the *a priori*/model velocities (rates of change) of baselines for co-located stations, i.e., the rate of change of baseline between a pair of VLBI radio telescopes and the rate of change of the baseline between the pair of co-located GNSS stations. Data for five VLBI stations in New Zealand, Australia and South Africa are collected from VieTrf13 (Table 2.1 in Section 2.3) for the period from 2012 to 2016. Each VLBI radio telescope I considered has a co-located GNSS station. The data for these GNSS stations are taken from ITRF2014-IGS (`http://itrf.ign.fr/ITRF_solutions/2014/doc/ITRF2014_GNSS.SSC.txt`). In ITRF2014-IGS data, three Australian stations and Hartebeesthoek station have several coordinates (positions and velocities). These discontinuities were caused by earthquakes or antenna/receiver changes. The ITRF2014 GNSS data are presented in Table 2.2.

Also, I take VLBI data from ITRF2014 (`ftp://itrf.ign.fr/pub/itrf/itrf2014/ITRF2014-IVS-TRF.SNX.gz`). Five VLBI station positions and velocities of ITRF2014 are presented in Table 2.3. I use this official VLBI data to calculate the relative velocities/the rates of change for baselines.

Table 2.2: ITRF2014 GNSS station positions and velocities at epoch 2010.0.

Stations	Model geocentric coordinates, m			Model velocities, m/yr			Standard deviation, m/yr		
	X	Y	Z	V_X	V_Y	V_Z	σ_{V_X}	σ_{V_Y}	σ_{V_Z}
WARK	-5115333.2400	477886.8996	-3767147.4392	-0.0226	-0.0023	0.0328	0.00007	0.00004	0.00005
HOB2	-3950071.8688	2522415.2874	-4311637.8234	-0.0387	0.0079	0.0412	0.00004	0.00004	0.00005
YAR3	-2389043.3013	5043313.4981	-3078524.8980	-0.0470	0.0085	0.0508	0.00006	0.00005	0.00004
KAT2	-4147369.1557	4581537.1264	-1573260.1871	-0.0356	-0.0129	0.0575	0.00004	0.00004	0.00004
HRAO	5084657.6261	2670325.2090	-2768481.0690	-0.0014	0.0193	0.0170	0.00003	0.00003	0.00004

Table 2.3: ITRF2014 VLBI station positions and velocities at epoch 2010.0.

Stations	Model geocentric coordinates, m			Model velocities, m/yr			Standard deviation, m/yr		
	X	Y	Z	V_X	V_Y	V_Z	σ_{V_X}	σ_{V_Y}	σ_{V_Z}
WARK12M	-5115324.3531	477843.3011	-3767193.9316	-0.0237	-0.0020	0.0327	0.0008	0.0004	0.0007
HOBART12	-3949991.6685	2522421.1832	-4311708.1551	-0.0386	0.0078	0.0412	0.00006	0.00005	0.00006
YARRA12M	-2388896.9787	5043349.9506	-3078590.9970	-0.0500	0.0120	0.0475	0.0003	0.0005	0.0004
KATH12M	-4147354.5358	4581542.4104	-1573303.3939	-0.0363	-0.0076	0.0580	0.0003	0.0003	0.0002
HART15M	5085490.8006	2668161.4281	-2768692.6691	-0.0011	0.0193	0.0163	0.00007	0.00005	0.00006

The VieTrf13 uses less than 2 years of the observations of AuScope 12-m antennas. This was a period with large errors and sometimes just test VLBI observations in the initial periods of the arrays. Now we have longer time series and can make a better estimate of station coordinates and velocities. I use the linear regression to calculate the observed weighted velocities for the VLBI stations. Table 2.4 presents velocities of VieTrf13 (columns 2-4) and ITRF2014 (columns 5-7), as well as our estimates of station velocities based on more than 2 years of extension observations (columns 8-10).

Table 2.4: Comparison of the model velocities (VieTrf13 and ITRF2014) with our observed weighted velocities.

Stations	Velocities of VieTrf13, m/yr			Velocities of ITRF2014, m/yr			Observed weighted velocities, m/yr		
	V_X	V_Y	V_Z	V_X	V_Y	V_Z	V_X	V_Y	V_Z
WARK12M	-0.0351	0.0022	0.0199	-0.0237	-0.0020	0.0327	-0.0216	0.0029	0.0326
HOBART12	-0.0383	0.0083	0.0414	-0.0386	0.0078	0.0412	-0.0382	0.0075	0.0397
YARRA12M	-0.0535	0.0164	0.0427	-0.0500	0.0120	0.0475	-0.0555	0.0153	0.0468
KATH12M	-0.0422	-0.0074	0.0567	-0.0363	-0.0076	0.0580	-0.0419	-0.0081	0.0540
HART15M	-0.0003	0.0192	0.0167	-0.0011	0.0193	0.0163	-0.0082	0.0182	0.0148

Table 2.5: Velocity residuals (observed minus model velocities for VieTrf13). Standard deviations are given in the last 3 columns. Data are provided for 5 stations in mm/yr.

Stations	VieTrf13			Standard deviation		
	ΔV_X (mm/yr)	ΔV_Y (mm/yr)	ΔV_Z (mm/yr)	σ_{V_X} (mm/yr)	σ_{V_Y} (mm/yr)	σ_{V_Z} (mm/yr)
WARK12M	**13.5**	-0.7	**12.7**	2.2	0.8	1.9
HOBART12	0.1	**-0.8**	*-1.7*	0.7	0.1	0.8
YARRA12M	*-2.0*	-1.1	**4.1**	0.9	2.2	1.0
KATH12M	0.3	*-0.7*	**-2.7**	0.9	0.7	0.8
HART15M	**-7.9**	**-1.0**	*-1.9*	2.1	0.2	0.9

Table 2.6: Velocity residuals (observed minus model velocities for ITRF2014). Standard deviations are given in the last 3 columns. Data are provided for 5 stations in mm/yr.

Stations	ITRF2014			Standard deviation		
	ΔV_X (mm/yr)	ΔV_Y (mm/yr)	ΔV_Z (mm/yr)	σ_{V_X} (mm/yr)	σ_{V_Y} (mm/yr)	σ_{V_Z} (mm/yr)
WARK12M	*2.1*	**4.9**	-0.1	0.9	0.4	1.3
HOBART12	0.4	-0.3	*-1.5*	0.7	0.1	0.6
YARRA12M	**5.5**	*3.3*	-0.7	0.6	2.0	0.7
KATH12M	**-5.6**	*-0.5*	**-4.0**	0.6	0.3	0.6
HART15M	**-7.1**	**-1.1**	*-1.5*	2.1	0.2	0.9

Tables 2.5 and 2.6 present the velocity residuals (observed minus model velocities) for the VieTrf13 and the ITRF2014 (ΔV_X, ΔV_Y, ΔV_Z) as well as the standard deviations (σ_{V_X}, σ_{V_Y}, σ_{V_Z}), where the standard deviations are calculated in 1σ level for 5 stations. In both tables, the standard deviations were calculated by:

$$\sigma = \sqrt{\sigma_{obs}^2 + \sigma_{catalogue}^2} \qquad (2.13)$$

where, the σ_{obs} denotes the standard deviation of observed velocities, the $\sigma_{catalogue}$ presents the standard deviation of VieTrf13 and ITRF2014 velocities. The standard deviations of ITRF2014 velocities were taken from ITRF2014-IVS-TRF.SNX.gz.

In Tables 2.5 and 2.6, some velocity residuals are greater than 1σ level of observed standard deviation. These are in Italic font. Those even greater than 3σ level, are highlighted in bold (e.g., WARK12M velocity residuals of VieTrf13). Velocity residuals which are smaller than 1σ level are presented in normal font. To compare these two Tables, the velocity residuals of ITRF2014 for WARK12M are better than the ones of VieTrf13, except WARK12M ΔV_Y. HART15M shows similar velocity residuals as VieTrf13 and ITRF2014. As to three Australian stations, YARRA12M and KATH12M present that the VieTrf13 are better than the results of ITRF2014, while HOBART12 shows the ITRF2014 velocities are close to the observed velocities. Overall, three out of five stations show that the ITRF2014 velocities are close to the observed one.

2.5 VLBI and GNSS baseline rates of change

In this section, I consider baselines between AUSTRAL radio telescopes and those of the corresponding co-located GNSS receivers. I calculate and compare the rates of change for each baseline. I use two theoretical VLBI models: the model from VieVS (VieTrf13) and the official ITRF2014-IVS model [Bachmann et al., 2016].

I use the official ITRF2014-IGS [Bachmann et al., 2016] as the theoretical GNSS model. I compare these theoretical models with the results of observations.

The baseline rate of change, $\frac{dB_{jk}}{dt}$, can be calculated with the use of vectors for coordinates and velocities using the dot product:

$$\frac{dB_{jk}}{dt} = \frac{(\vec{V}_j - \vec{V}_k) \cdot \vec{B}_{jk}}{||B_{jk}||} \tag{2.14}$$

where

$$\vec{B}_{jk} = \vec{C}_j - \vec{C}_k \tag{2.15}$$

In Equations (2.14) and (2.15), j and k denote station j and station k; $C(0)$ indicates coordinates at the moment t_0; V stands for velocity; $||B_{jk}||$ is the length of baseline:

$$\vec{C}_j(0) = \begin{pmatrix} x_j \\ y_j \\ z_j \end{pmatrix}, \vec{V}_j = \begin{pmatrix} V_{xj} \\ V_{yj} \\ V_{zj} \end{pmatrix} \tag{2.16}$$

$$\vec{C}_k(0) = \begin{pmatrix} x_k \\ y_k \\ z_k \end{pmatrix}, \vec{V}_k = \begin{pmatrix} V_{xk} \\ V_{yk} \\ V_{zk} \end{pmatrix} \tag{2.17}$$

In the case of theoretical models, I use coordinates and velocities provided by a corresponding model. In the case of VLBI observations, I use station coordinates provided by the VieTrf13 and observed weighted velocities I calculated in the previous section.

Table 2.7 summarizes baseline rates of change for VLBI and GNSS stations. Column 1 indicates the pair of stations which form a baseline. Columns 2-3 provide theoretical (model) baseline rates of change for GNSS (ITRF2014-IGS) and VLBI (ITRF2014-IVS) stations. Column 4 shows the VieTrf13 baseline rates of change.

Column 5 shows the baseline rates of change which are calculated from the observed weighted velocities (AUSTRAL observations) using Equation (2.14). The last column presents the baseline rates of change I obtained from the IVS Combination Center (CCIVS) [IVS, 2016].

Table 2.7: Baseline rates of change (in mm/yr), calculated for the ITRF2014-IGS, the ITRF2014-IVS, the VieTrf13, the AUSTRAL observations, as well as the CCIVS (COMBI) for 10 baselines. The standard deviations at 1σ level are indicated in columns 2-6.

Stations	ITRF2014-IGS (mm/yr)	ITRF2014-IVS (mm/yr)	VieTrf13 (mm/yr)	AUSTRAL observations (mm/yr)	CCIVS (COMBI) (mm/yr)
Ww–Hb	-1.1 ± 0.1	-0.8 ± 0.8	-1.2 ± 2.1	-5.7 ± 2.3	5.1 ± 1.8
Hb–Ke	0.3 ± 0.1	4.0 ± 0.3	3.0 ± 0.7	2.3 ± 1.9	0.7 ± 1.1
Hb–Yg	0.1 ± 0.1	0.2 ± 0.4	-0.5 ± 0.9	0.4 ± 2.8	1.3 ± 0.6
Hb–Ht	32.9 ± 0.1	33.0 ± 0.1	33.5 ± 0.2	25.5 ± 3.3	35.1 ± 2.6
Ww–Ke	-0.4 ± 0.1	4.3 ± 1.0	7.3 ± 2.6	-3.8 ± 2.0	6.7 ± 2.4
Ww–Ht	23.6 ± 0.1	25.9 ± 0.8	37.1 ± 2.1	14.5 ± 3.3	35.4 ± 7.8
Ww–Yg	-0.9 ± 0.1	0.5 ± 1.1	5.7 ± 2.7	-4.9 ± 3.0	19.4 ± 3.6
Ke–Yg	-0.02 ± 0.1	0.3 ± 0.6	5.2 ± 1.3	1.0 ± 2.6	2.8 ± 0.6
Ht–Yg	38.8 ± 0.1	43.1 ± 0.4	48.8 ± 0.8	42.9 ± 3.7	44.9 ± 1.4
Ke–Ht	31.9 ± 0.1	34.0 ± 0.3	40.4 ± 0.7	32.4 ± 3.0	40.2 ± 2.1

To illustrate data provided in Table 2.7, I group the baselines according to their lengths and geographic locations, and put them on the maps (Figures 2.12–2.14). The first set of maps (Figure 2.12) shows baseline rates of change between Australasia (New Zealand and Australia) and Africa. The second set (Figure 2.13)

shows baseline rates of change between Australian stations and Warkworth station (New Zealand). Finally, the last set (Figure 2.14) is for the baseline rates of change inside the continent of Australia. Figure 2.15 is designed to present the results of Table 2.7 as graphs. The y-axis in Figure 2.15 shows the baseline rates of change in mm/yr. The x-axis presents the models and techniques used. They follow the order of columns in Table 2.7. Data for different baselines are shown with different colours; these are indicated in legends in the graphs.

Discussion. First of all, the results of two space geodetic techniques (VLBI and GNSS) presented in Figures 2.12–2.14 and Figure 2.15 show that the baseline rates of change between Australasia and South Africa are systematically greater than the baseline rates of change for the other two groups. It is understandable, because South African and Australasian stations are located on two different tectonic plates which move with respect to one another. The rates of change for Australasian baselines are much smaller than the one for the first set (South Africa–Australasian) – the New Zealand and Australian stations are located on the same tectonic plate.

I also note that all models and observations show greater rates of change for Ht–Yg than for other Africa–Australasia baselines. At the same time, Ht–Ww baseline shows smaller rate of change than the other three baselines. This can be explained by geometric factors: the greater the baseline, the smaller the projections of station horizontal velocity vectors on the baseline because of the curvature of the Earth's surface.

Furthermore, I note differences between two techniques, VLBI and GNSS, in terms of the baseline rates of change. At the level of individual baselines, some notes can also be made. For example, for the baseline Hb–Ke, the results present statistically significant difference between two geodetic techniques (0.3 ± 0.1 mm/yr of ITRF2014-IGS compared with 4.0 ± 0.3 mm/yr of ITRF2014-IVS, 3.0 ± 0.7

mm/yr of VieTrf13). AUSTRAL observations show 2.3 ± 1.9 mm/yr. Therefore, if I use 3σ level, I will get 2.3 ± 5.7 mm/yr. Here I cannot state that the difference between AUSTRAL observations and the other results is statistically significant. More observational data is required to improve accuracy of VLBI baseline rates of change.

The GNSS baseline rates of change are close to zero for the same tectonic plate (AuScope and Warkworth baselines–AuScope baselines). For these baselines, I find a good agreement between GNSS and AUSTRAL observations. However, the scattering for Warkworth–AuScope baseline rates of change is greater than for AuScope. This is because Warkworth had sparse time series. Two VLBI models show worse results (greater dispersion) than GNSS and AUSTRAL observations. These models are based on limited periods of observations (ITRF2014-IVS up to 2014 and VieTrf13 stopped at 2013). However, errors in AUSTRAL observations are still large compared with GNSS.
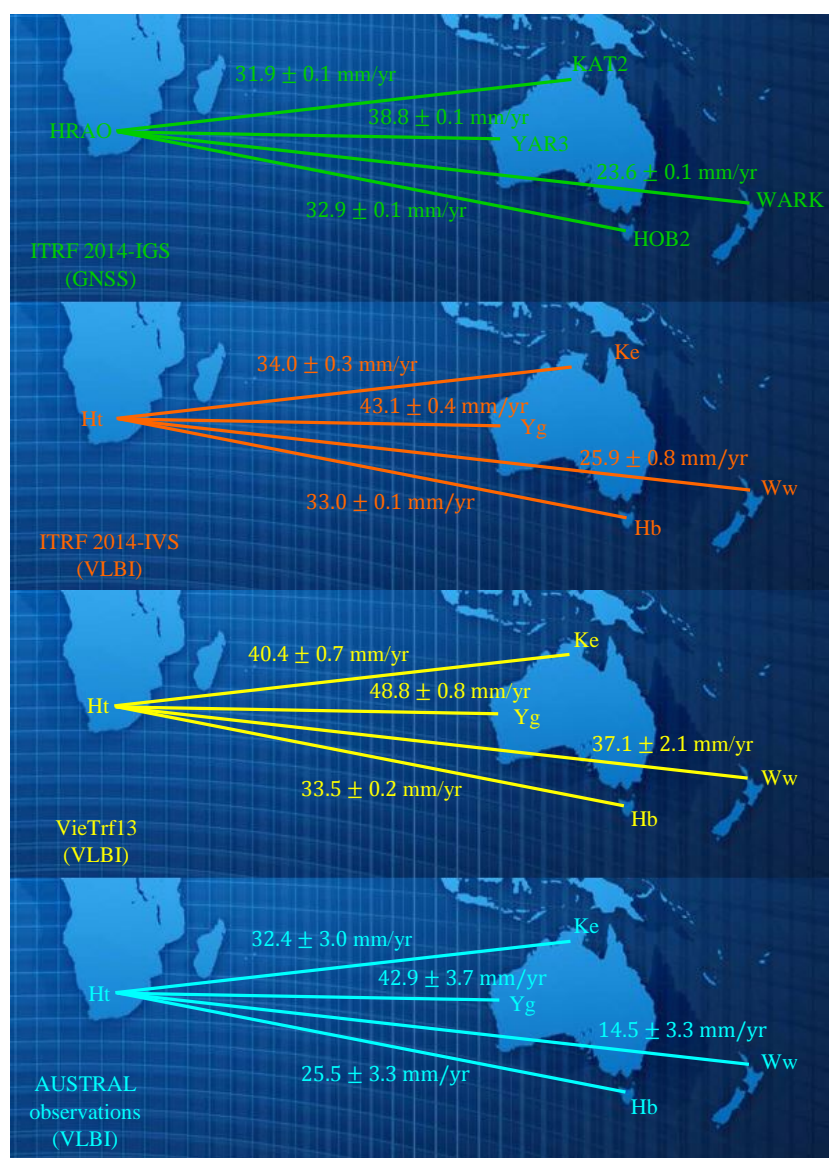
Figure 2.12: Theoretical baseline rates of change (mm/yr) between South Africa and Australasia. The GNSS rates of change are in green, the VLBI ITRF 2014 rates of change in orange, the VLBI VieTrf13 rates of change are in yellow, and the VLBI observed weighted (AUSTRAL observations) rates of change are in blue
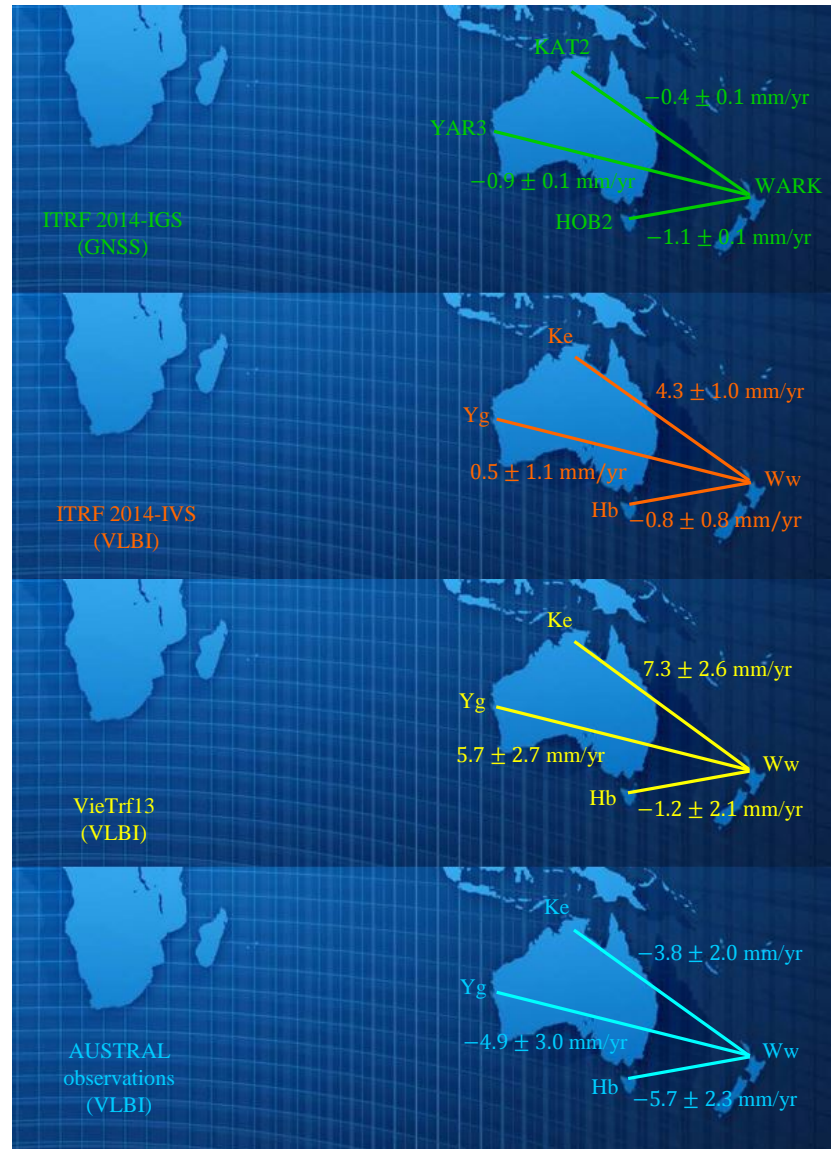
Figure 2.13: Theoretical baseline rates of change (mm/yr) between New Zealand and Australia. The GNSS rates of change are in green, the VLBI ITRF 2014 rates of change in orange, the VLBI VieTrf13 rates of change are in yellow, and the VLBI observed weighted (AUSTRAL observations) rates of change are in blue
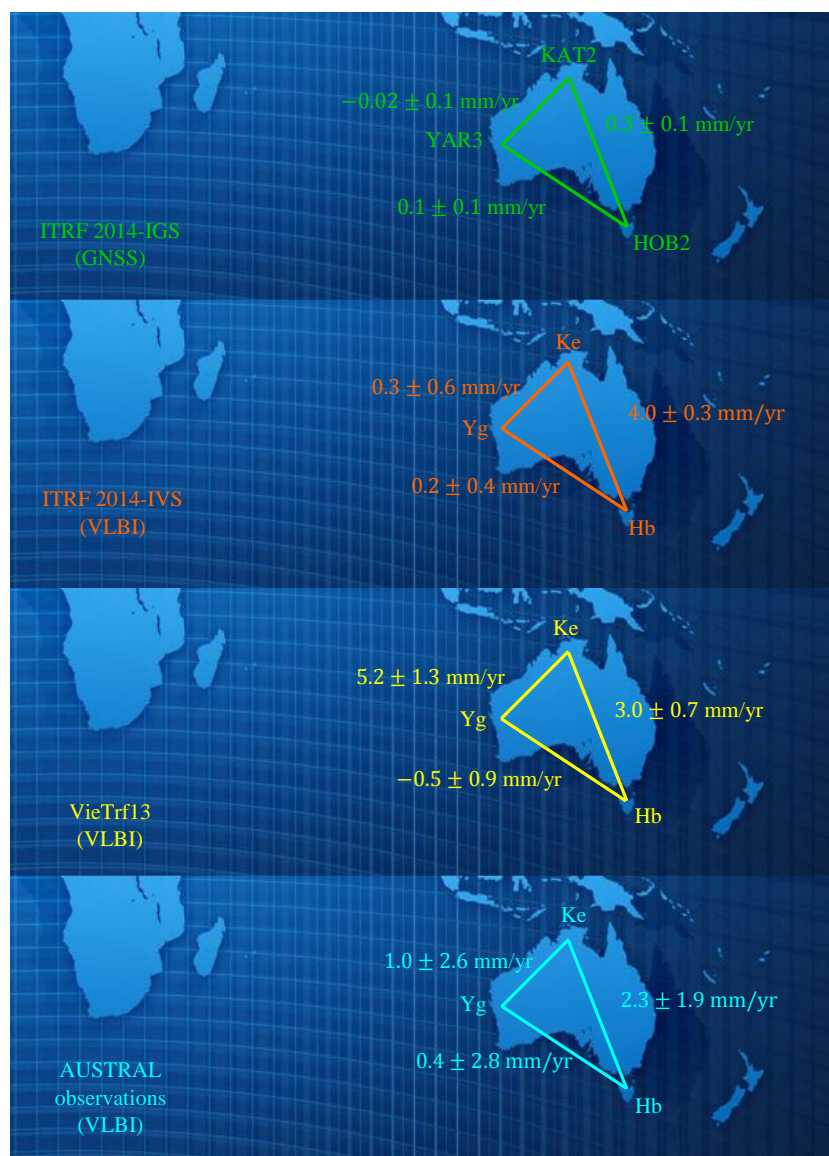
Figure 2.14: Theoretical baseline rates of change (mm/yr) in Australia. The GNSS rates of change are in green, the VLBI ITRF 2014 rates of change in orange, the VLBI VieTrf13 rates of change are in yellow, and the VLBI observed weighted (AUSTRAL observations) rates of change are in blue
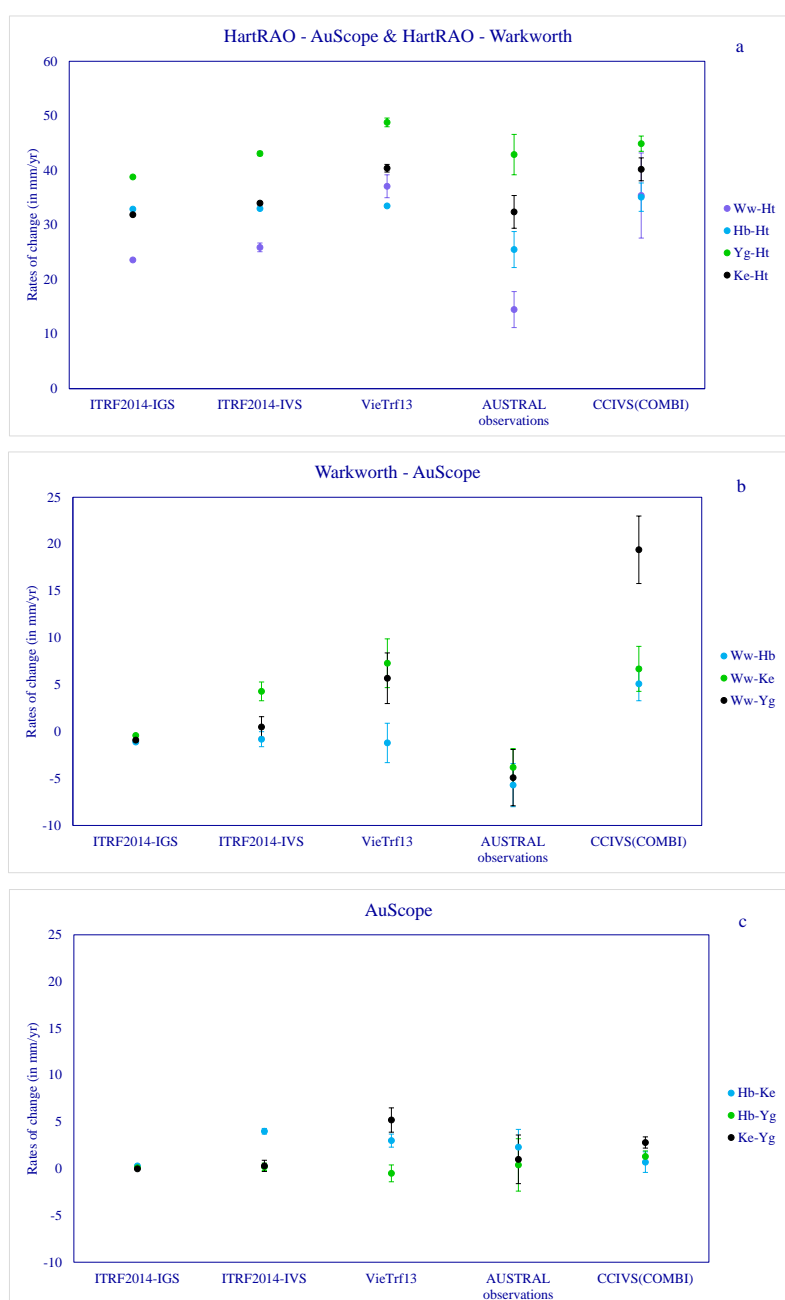
Figure 2.15: AUSTRAL VLBI telescopes and co-located GNSS receivers baseline rates of change

2.6   Baseline length repeatabilities for IVS-R1/R4 sessions and AUSTRAL sessions

Global tectonic plate motions and intraplate dynamics can be directly measured by VLBI and GNSS with the precision of a few millimetres. The baseline length repeatability (baseline root-mean-square error σ_L) has been used as a quality measure of geodetic VLBI data since the early 1990s [Titov, 2009]. The VLBI baselines are invariant with respect to the reference frame rotation, whereas the station coordinate estimates may be affected by the reference frame inconsistency. This means that if one selects a set of stations in each 24-hour session, the daily reference system may slightly vary from session to session followed by additional uncertainty in station coordinate estimates. Baseline lengths are free of the additional reference frame 'uncertainty' (private communication with Oleg Titov, 2016).

Using geocentric coordinates of AUSTRAL stations determined in section 2.3, I computed baselines among five AUSTRAL radio telescopes. In Figure 2.16, I provide an example of our results for a particular baseline, namely, WARK12M-HOBART12. Plots for the remaining nine baselines are placed in Appendices A-B. Matlab code for computing baseline residuals is presented in Appendix E.

I plotted the residuals (observed minus theoretical), and I found the weighted rms (WRMS in mm) for each baseline. Also, I limited the y-axis at ± 10 cm for each baseline (Figure 2.16). The same epoch (from 2012 to mid 2016) for each baseline was used. The WRMS of three different sessions, namely, IVS-R seesions (IVS-R1 and IVS-R4), AUSTRAL sessions and IVS-R + AUSTRAL sessions are presented in Table 2.8. Also, I listed the WRMS values from the CCIVS in the same table (CCIVS see: `http://www.ccivs.bkg.bund.de/EN/Quarterly/VLBI-Baseline/vlbi-baseline_node.html`) [IVS, 2016].

Table 2.8: Baseline length repeatabilities (wrms in mm) among five AUSTRAL stations of the IVS-R1/R4 sessions, the AUSTRAL sessions and the IVS-R + AUSTRAL sessions compared with the WRMS from CCIVS. In brackets, the number of sessions is given for each baseline.

Baselines	IVS-R1 (175)	IVS-R4 (154)	AUST (117)	IVS-R+AUST (446)	CCIVS
Ww–Hb	7.5 (19)	9.3 (30)	10.4 (62)	11.9 (112)	9.6 (132)
Hb–Ke	13.9 (87)	16.2 (80)	11.2 (98)	14.4 (259)	10.0 (303)
Hb–Yg	8.8 (83)	11.5 (83)	7.8 (100)	9.8 (266)	4.7 (297)
Hb–Ht	24.7 (49)	20.5 (40)	19.3 (52)	23.6 (141)	12.5 (151)
Ww–Ke	16.8 (32)	24.9 (33)	17.0 (60)	20.5 (125)	9.0 (122)
Ww–Ht	16.7 (20)	21.7 (21)	28.2 (32)	28.4 (73)	16.7 (70)
Ww–Yg	14.7 (29)	14.8 (34)	13.0 (60)	14.9 (123)	13.1 (119)
Ke–Yg	9.2 (94)	13.0 (99)	9.3 (94)	11.6 (287)	5.0 (291)
Ht–Yg	18.2 (65)	19.5 (47)	10.5 (50)	18.8 (162)	6.9 (148)
Ke–Ht	18.8 (60)	25.9 (42)	17.6 (49)	21.0 (151)	9.6 (144)

In CCIVS, the WRMS of the baselines among four Australasian stations has been analysed from 2010 to 2016, except for the baseline Ww–Yg, which has one year less than the others. The WRMS analysis of the baselines among AuScope stations and South African has been started from 2011 to 2016, except for Ww–Ht the WRMS has been analysed from 2012 to 2016.

Table 2.8 shows that the AUSTRAL sessions have better results, however, for the long baseline Ww–Ht, the IVS-R sessions present better performance (28.2 mm – AUSTRAL sessions, 16.7 mm – IVS-R1 sessions, 21.7 mm – IVS-R4 sessions).

I combined the IVS-R sessions and the AUSTRAL sessions to compare with the WRMS from CCIVS, and my results are worse than the one from CCIVS. This can be explained as our analysis has been started from the epoch at 2012 (2012-2016), so the time series is shorter than the one from CCIVS. Furthermore, when I processed VLBI data in VieVS, some sessions with big χ^2 were included (e.g., sessions in 2016).
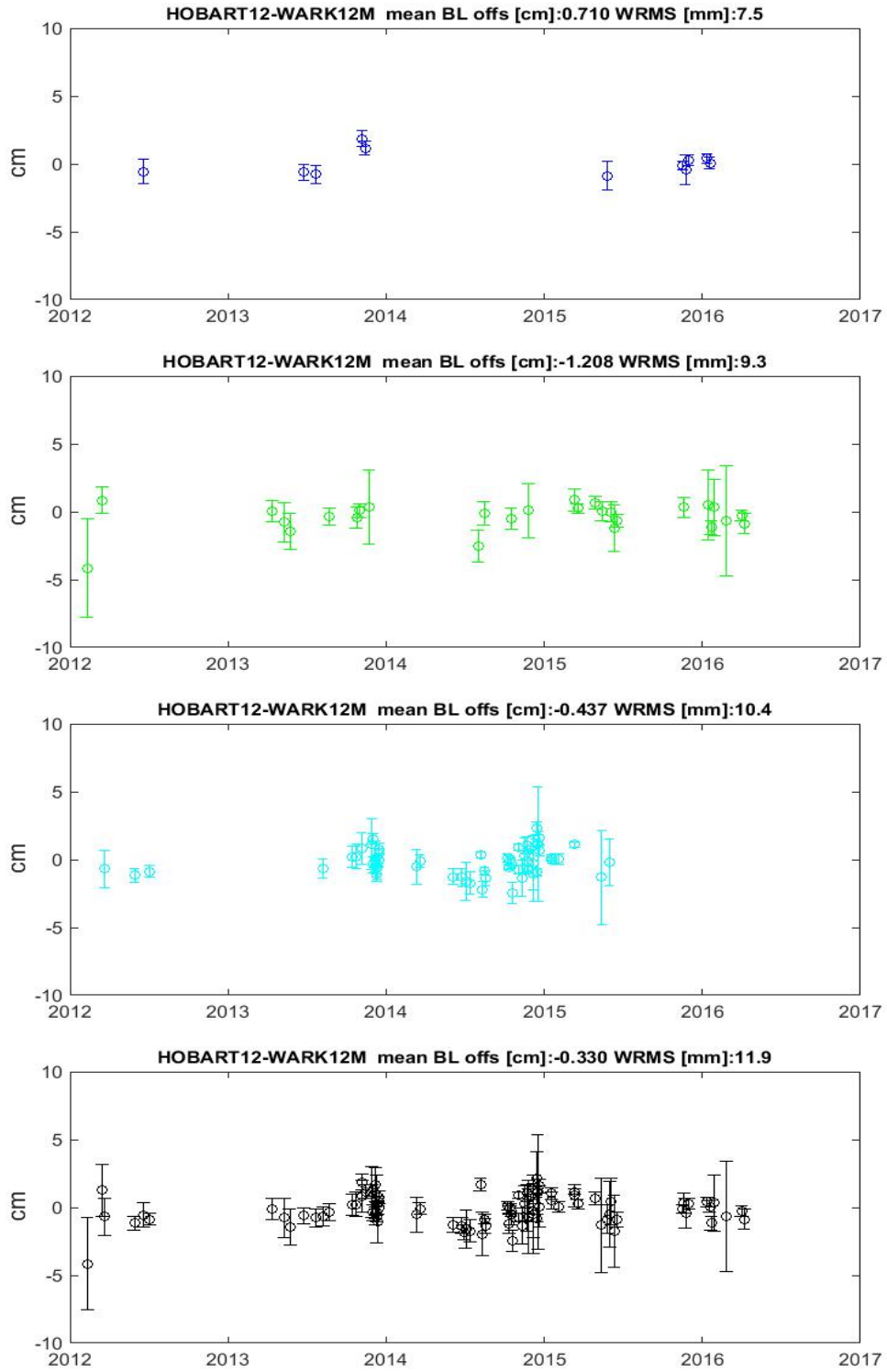
Figure 2.16: HOBART12-WARK12M residuals for IVS-R1 (blue), IVS-R4 (green), AUSTRAL (light blue), and IVS-R1/R4+AUSTRAL (black)

Chapter 3

Tropospheric propagation delays

Electromagnetic waves emitted by distant radio sources (e.g., quasars) pass through intergalactic, interstellar, interplanetary, and terrestrial atmospheric media before they are received by radio telescopes. Both the neutral and charged components of the media modify the propagation speed. This effect produces delay relative to propagation in vacuum. When using the VLBI method, the difference in properties of the Earth troposphere is responsible for a differential delay measured in different geographic locations [Sovers et al., 1998a].

Space geodetic techniques, such as VLBI, GNSS and DORIS are used to investigate the tropospheric delays. The challenging goals for the Global Geodetic Observing System (GGOS) of the International Association of Geodesy (IAG) are an accuracy of 1 mm for position and 0.1 mm/yr for velocities of globally distributed observing stations [Böhm, 2007]. Proper modelling of tropospheric delays is critical for the accuracy of space geodetic techniques, as many imperfection of these delays can affect the accuracy of geodetic parameters.

In this Chapter, I aim to compare VLBI and GNSS measurements of tropospheric delay. I also compare the accuracy of AUSTRAL and IVS measurements of the

tropospheric delay. As AUSTRAL sessions have many more observations per time unit it can be expected that they are more accurate than the IVS sessions [Plank et al., 2016]. In this Chapter I attempt to verify this assumption.

The troposphere is the lowest layer of the Earth's atmosphere which is placed between the Earth's surface and an altitude of few tens of kilometers. The tropospheric propagation delay ΔL as a function of the elevation angle ε can be modelled as the zenith delay ΔL^z multiplied by an elevation-dependent mapping function $m(\varepsilon)$.

$$\Delta L(\varepsilon) = \Delta L^z \cdot m(\varepsilon) \tag{3.1}$$

This concept is not only used to determine *a priori* slant delays for the observations, but also to estimate residual zenith delays. Both zenith delays and other parameters such as stations clocks and stations heights are estimated in the analysis of space geodetic observations. The components of partial derivatives for the estimation of stations clocks (=1) and stations heights $\sin(e)$ are exactly known, where station heights are dependent on the elevation angle only. The partial derivative for the estimation of the zenith delay is the mapping function which is known with a limited accuracy [Nilsson et al., 2013].

The propagation delay can be split into a Zenith Hydrostatic Delay (ZHD) (ΔL_h^z), which is caused by the dry gases present at the troposphere and a ZWD (ΔL_w^z), which is caused by the wet component, such as water vapour and condensed water in form of clouds. Assuming azimuthal symmetry of the neutral atmosphere around the station, it can be calculated through numerical integration of the hydrostatic refractivity, N_h, and the non-hydrostatic or wet refractivity, N_w, between the antenna, r_s, and the top of the neutral atmosphere, r_a, with equation:

$$\begin{aligned}
\Delta L^z &= \Delta L_h^z + \Delta L_w^z \\
&= 10^{-6} \int_{r_s}^{r_a} N_h dz + 10^{-6} \int_{r_s}^{r_a} N_w dz
\end{aligned} \tag{3.2}$$

where

$N = (n - 1) \times 10^6$ is the (total) group refractivity of moist air, n is the (total) refractive index of moist air [Nilsson et al., 2013].
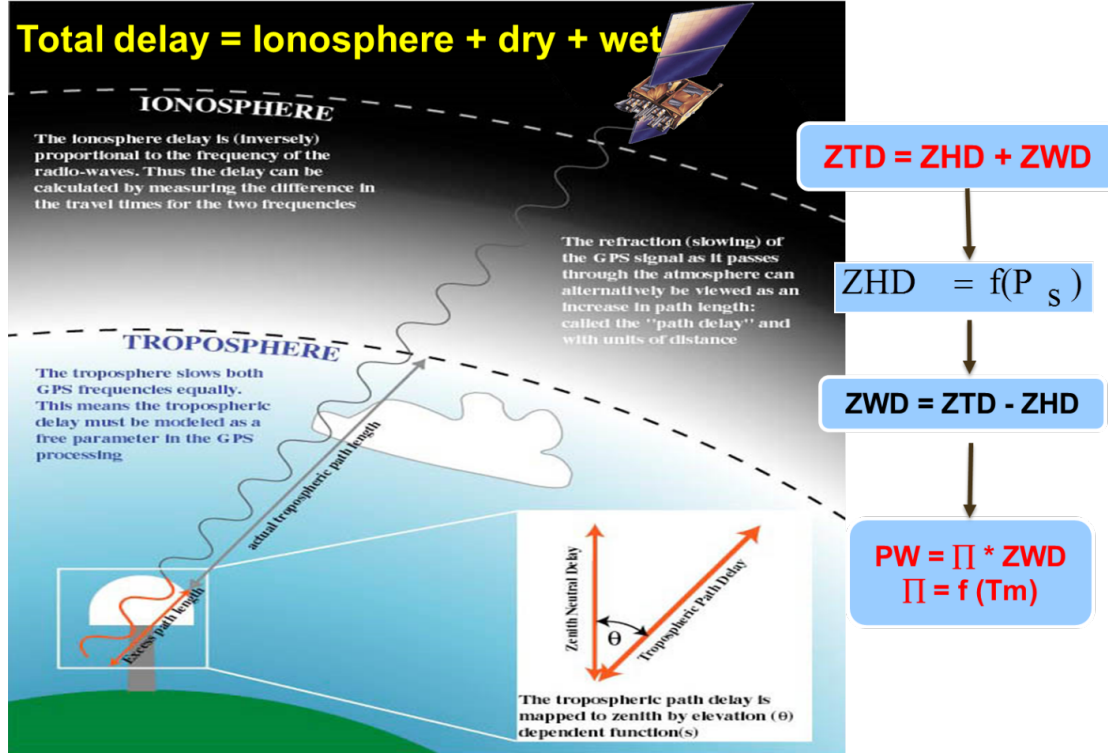
Figure 3.1: Illustration of a radio signal when travelling from a satellite to a receiver on the surface of the Earth. The troposphere delay is modeled to the vertical direction, or zenith total delay (ZTD). This combines the hydrostatic and wet delay (ZHD and ZWD). ZHD is removed by measuring the atmospheric surface pressure, leaving PW (by courtesy of: GPS Spotlight) [GPS, 2012]

3.1 Troposphere mapping function

The troposphere mapping function is used to describe the relation between the tropospheric delay at zenith (ZHD; ZWD) and an elevation angle ε above the

horizon. The troposphere mapping function can be simply represented by the cosecant function of the elevation angle [Schuh and Böhm, 2013c]:

$$m(\varepsilon) = \frac{1}{\sin(\varepsilon)} \tag{3.3}$$

In order to provide a more precise model, the continued fraction form is used [Böhm et al., 2006b]:

$$m(\varepsilon) = \cfrac{1 + \cfrac{a_{h,w}}{1 + \cfrac{b_{h,w}}{1 + c_{h,w}}}}{\sin(\varepsilon) + \cfrac{a_{h,w}}{\sin(\varepsilon) + \cfrac{b_{h,w}}{\sin(\varepsilon) + c_{h,w}}}} \tag{3.4}$$

where $a_{h,w}$, $b_{h,w}$ and $c_{h,w}$ are the hydrostatic and wet coefficients of the mapping function.

3.1.1 Vienna Mapping Function1: VMF1

According to [Böhm et al., 2006a], the most accurate mapping functions globally available are the VMF1 which is provided by the Department of Geodesy and Geoinformation of the Vienna University of Technology. The coefficients as well as hydrostatic and wet zenith delays of VMF1 are determined from data of the European Center for Medium-Range Weather Forecasts (ECMWF) which have improved the accuracy and precision of space geodetic results significantly [Böhm and Schuh, 2007]. The coefficients b and c are provided as analytical function which depends on station latitude and the day of the year as input parameters in Equation (3.5). The coefficients a are determined from rigorously raytraced mapping functions at 3° elevation [Böhm and Schuh, 2014].

The coefficients for the hydrostatic mapping function, b_h and c_h, are taken from the hydrostatic part of the Isobaric Mapping Function (IMF). The coefficients are determined by $b_h = 0.002905$ and $c_h = 0.0634 + 0.0014 \cdot \cos(2\varphi)$, where φ is the geodetic latitude. For the wet part, the coefficients b_w and c_w are taken from the Neil Mapping Function (NMF), when $\varphi = 45°$, $b_w = 0.00146$, and $c_w = 0.04391$ [Böhm and Schuh, 2014].
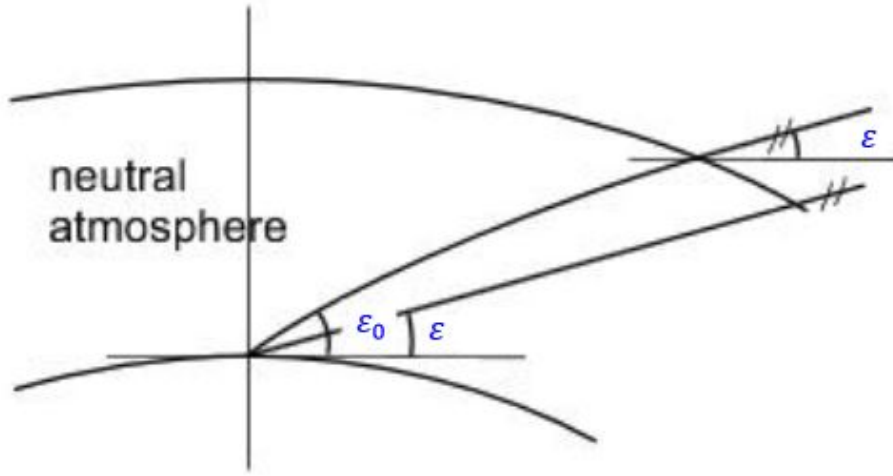
Figure 3.2: Ray path through the atmosphere. The bending of the ray in the neutral atmosphere, where the initial elevation angle is greater than the elevation angle (by courtesy of [Böhm and Schuh, 2014])

Input parameters for the raytracing program are an initial elevation angle ε_0, and values for height, temperature as well as water vapor pressure at distinct pressure levels in the neutral atmosphere (e.g., 21 levels from 1000 hPa to 1 hPa total pressure) by ERA-40 (ECMWF 40-year REANALYSIS) data. The outgoing (vacuum) elevation angle ε (Figure 3.2), and the hydrostatic and wet mapping function are determined at an initial elevation angle ε_0 of 3.3°. The hydrostatic mapping function includes the geometric bending effect, which is determined by

raytracing.

The Geo-department of the Vienna University of Technology has provided VMF1 global grids with resolution of $2.5° \times 2.0°$ (longitude-latitude) at $0h$, $6h$, $12h$ and $18h$ UT. The coefficients a_h and a_w are determined for all geodetic VLBI stations [Böhm and Schuh, 2014]. The hydrostatic delay depends on dry pressure, it can be modelled and determined more precisely with a few millimeter accuracy, whereas the wet delay need to be estimated within the Least-Square Adjustment (LSM) of the VLBI and GNSS observations [Petrovski and Tsujii, 2012].

3.2 Tropospheric horizontal gradients

In order to improve the accuracy of geodetic estimates, the horizontal gradients are usually estimated in the analysis of VLBI and GNSS observations in a linear form (Equation (3.5)) [Teke et al., 2011a]

$$\Delta L(\varepsilon) = \Delta L_h^z m f_h(\varepsilon) + \Delta L_w^z m f_w(\varepsilon) + m f_{AZ}(\varepsilon)[G_N \cos(\alpha) + G_E \sin(\alpha)]. \quad (3.5)$$

The four parameters in Equation (3.5) are the ZHD, ΔL_h^z, the ZWD, ΔL_w^z, and horizontal delay gradient with components denoted by G_N, G_E, which are used to determine the gradient at the azimuth α of the observation, then mapped with gradient mapping function $m f_{AZ}(\varepsilon)$ to the elevation of the observation. The $m f_h$, $m f_w$ and $m f_{AZ}$ present the mapping function for the hydrostatic, wet and gradient of the troposphere; ε is the elevation angle of the observation direction in vacuum; the azimuth angle (α) in which the signal is received, measured clockwise from north [Böhm and Schuh, 2007].

Based on Equation (3.5), the mapping function for the gradient of the troposphere $m f_{AZ}(\varepsilon)$ can be written as:

$$m f_{AZ}(\varepsilon) = m_w(\varepsilon) \cdot \cot(\varepsilon) \quad (3.6)$$

3.3 Estimation of tropospheric zenith wet delay (ZWD) with VieVS

In VieVS, the tropospheric ZWD is estimated in the least-squares adjustment as CPWLO functions on different time intervals, and the VMF1 is used. Below I use 1-hour time interval. The Equation (3.7) denotes the functional model of the wet delay at one station represented by piecewise linear offsets x_1 and x_2 of the zenith wet delays at the integer hours t_1 and t_2 [Schuh and Böhm, 2013c].

$$\Delta L_{trop}^{wet}(t) = mf_w(t) \cdot x_1 + mf_w(t) \cdot \frac{t - t_1}{t_2 - t_1} \cdot (x_2 - x_1) \tag{3.7}$$

where $mf_w(t)$ represents the wet mapping function of the observation at epoch t between integer hours.

The partial derivatives with respect to CPWLO of the ZWD are:

$$\frac{d\Delta L_{trop}(t)}{d(ZWD)_{x_1}} = mf_w(t) - mf_w(t) \cdot \frac{t - t_1}{t_2 - t_1} \tag{3.8}$$

$$\frac{d\Delta L_{trop}(t)}{d(ZWD)_{x_2}} = mf_w(t) \cdot \frac{t - t_1}{t_2 - t_1} \tag{3.9}$$

The estimation setting for the troposphere can be found in *Estimation-Least squares-Troposphere* in the GUI. The ZWD are estimated every 1-hour with 1.5 cm constraints to cover periods with little or non observations and troposphere gradients (constraints at 0.05 cm after 360 minutes) are introduced (Figure 3.3).

Figure 3.3: Troposphere estimation in VieVS

3.3.1 Zenith wet delay time series for AUSTRAL stations for 2012-2016

Figure 3.5 presents the estimates of tropospheric ZWD in centimeters (cm) at five AUSTRAL stations (WARK12M, HOBART12, YARRA12M, KATH12M and HART15M). The ZWD is computed for IVS-R1/R4 sessions and AUSTRAL sessions from 2012 to mid 2016. Each point of the graph represents a 24-hour session; I used weighted average over 60-minute time interval data. This means for each 24-hour session, one value was calculated. I limited y-axis range by 50 cm (maximum) for KATH12M, all other four stations have y-axis range from 0 to 40 cm.

There is a good agreement between data from IVS-R1/R4 sessions and AUSTRAL sessions. Significant (large amplitude) seasonal variations are observed in mid-latitudes (e.g., KATH12M), whereas smaller amplitudes are located at higher latitude (e.g., HOBART12) and the equator areas. To support this statement, I provide a map for distribution of the tropospheric zenith total delay from [Jin et al., 2007] (Figure 3.4). This is in agreement with our results presented in Figure 3.5, where KATH12M shows significant seasonal variations ranging from 5 cm in winter days to 30-40 cm in summer days, whereas HOBART12 and YARRA12M show smaller seasonal variations approximately from 5 to 15 cm. In fact, seasonal variations I found for KATH12M are much greater than one can expect from Figure 3.4. The latter predicts seasonal variation with amplitude of 8 to 9 cm, whereas our analysis (Figure 3.5) shows the amplitude of 25 to 35 cm for KATH12M. HART15M (Figure 3.5) shows amplitude seasonal variations which are ranging from approximately 5 to 20 cm in both IVS global R sessions and AUSTRAL sessions. WARK12M (Figure 3.5) did not show statistically significant seasonal variatons, meanwhile, the IVS-R1 sessions have a gap during 2014 (no observations), whereas the AUSTRAL sessions were gathered at the same epoch.
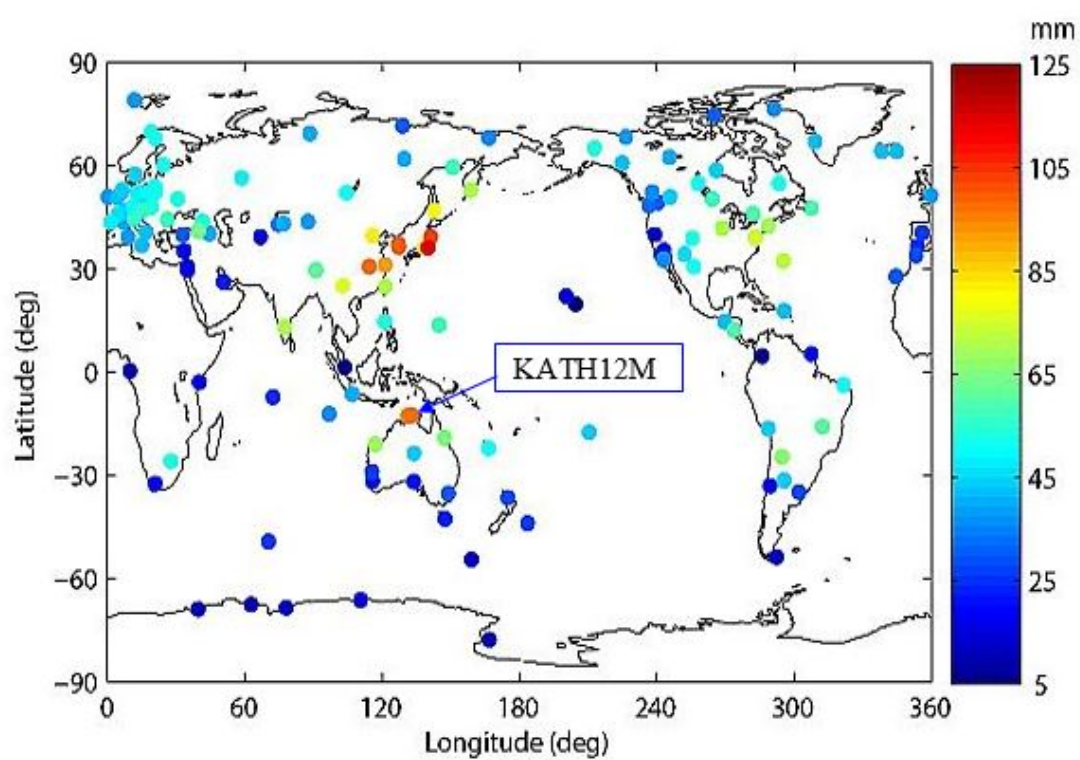
Figure 3.4: Annual variation amplitude of ZTD from global IGS observations (by courtesy of [Jin et al., 2007])
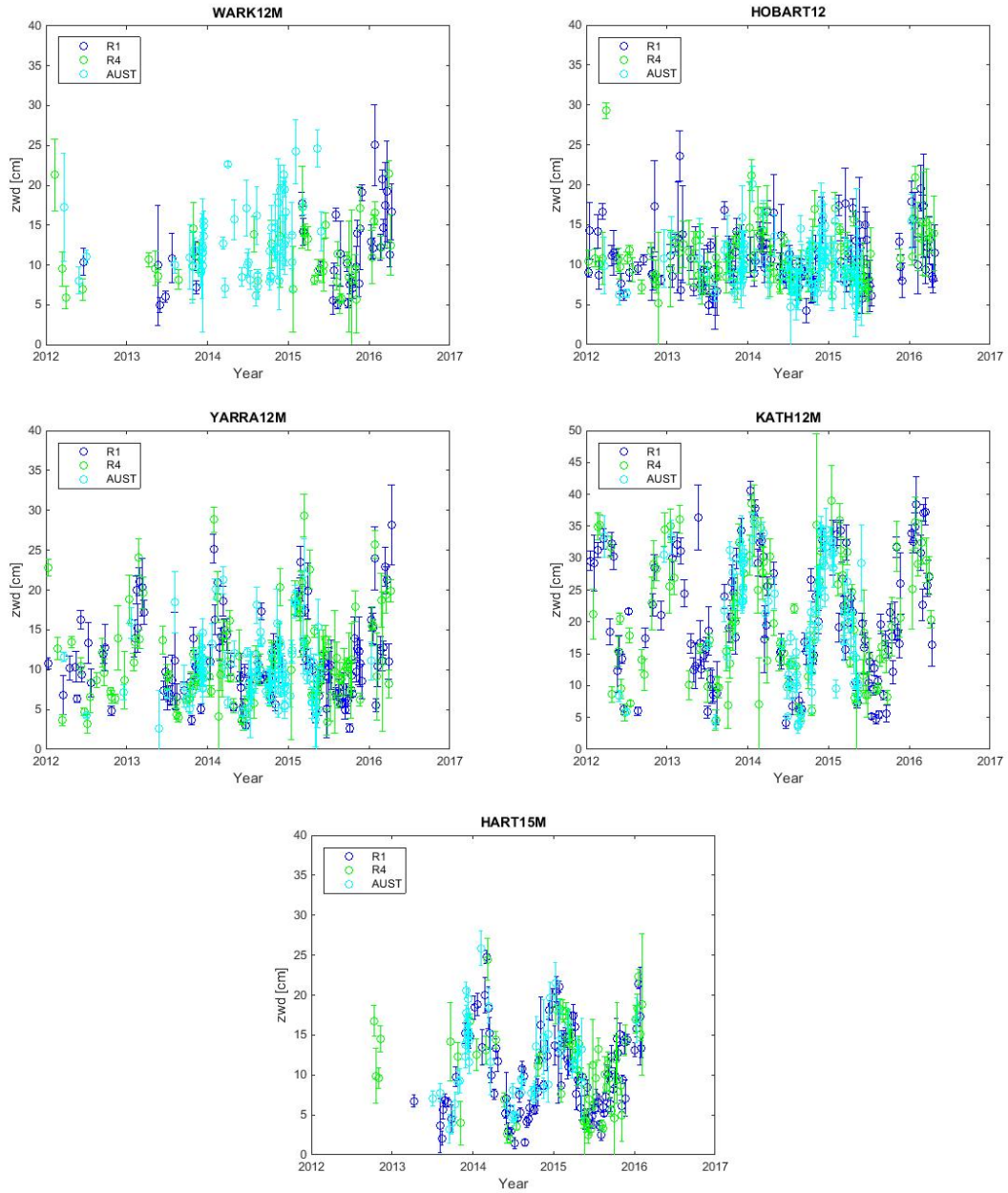
Figure 3.5: Tropospheric Zenith Wet Delay (ZWD) time series for the period from 2012 to the mid of 2016. IVS-R1 sessions are shown in green, IVS-R4 sessions presented in blue, and AUSTRAL sessions are shown in cyan for five stations

3.3.2 Comparison between VLBI and GNSS measurements of the zenith wet delay for WARK12M with time interval at 10 mins, 30 mins and 60 mins

Several studies on inter-technique comparison of troposphere parameters have been performed in order to assess the level of agreement between various space geodetic techniques [Teke et al., 2013].

[Behrend et al., 2002] compared ZWD from the non-hydrostatic numerical weather prediction model (MM5) and a hydrostatic NWP model with the observational results of various geodetic techniques – VLBI, GNSS and a Water Vapor Radiometer (WVR). They found that the correlation coefficients between VLBI and GNSS data for the ZWD are high. They range between 86 and 92 percent based on observations at three different stations – see Figure 3.6.

Stationwise statistical parameters for the independently derived ZWD values

Meth. 1	Meth. 2	# Points	Bias (cm)	RMS diff. (cm)	Corr. (%)
Madrid					
VLBI	GPS	75	−0.99	±1.37	91.9
	WVR	24	−1.18	±0.79	90.8
	MM5	75	−1.14	±1.61	91.2
GPS	WVR	28	−0.66	±0.82	74.8
	MM5	102	−0.20	±1.32	88.2
WVR	MM5	28	0.76	±1.35	90.4
Onsala					
VLBI	GPS	90	−0.39	±0.57	90.8
	WVR	62	−0.08	±0.69	95.4
	MM5	90	−1.03	±1.34	94.3
GPS	WVR	62	0.35	±0.81	86.8
	MM5	102	−0.60	±1.47	85.2
	RS	39	0.46	±1.25	90.8
WVR	MM5	62	−1.11	±1.27	90.3
Wettzell					
VLBI	GPS	90	−0.90	±0.74	85.9
	WVR	60	0.12	±3.38	52.4
	MM5	90	−0.94	±1.35	85.2
GPS	WVR	121	1.15	±3.84	74.8
	MM5	98	0.01	±1.43	88.8
WVR	MM5	68	−0.52	±3.95	39.3

The bias value is taken in the sense Meth. 1 minus Meth. 2.

Figure 3.6: Statistical parameters for the independently derived ZWD values (by courtesy of [Behrend et al., 2002])

Also, [Teke et al., 2011b] and [Teke et al., 2013] found that the VLBI estimates of tropospheric ZTD was similar to those derived from observations with the GNSS during CONT campaigns. They found that the best ZTD agreement, interpreted as the smallest standard deviation, was between VLBI and GNSS – about a few millimeters at most of the co-located sites. For example, it was just 3 mm for Ny-Ålesund (NYA1) during CONT05 campaign.

Comparison of the tropospheric ZWD between VLBI and GNSS for the AUSTRAL sessions and the IVS-R sessions is the main purpose of this subsection. Zenith wet delay data from GNSS can be compared with VLBI tropopheric ZWD at WARK12M. I randomly chose four 24-hour VLBI sessions from IVS-R1 (3rd Nov, 2015), IVS-R4 (13th Aug, 2015) and AUSTRAL sessions (18th Jan, 2015 and 3rd Feb, 2015) in which WARK12M participated. I plot their VLBI tropospheric ZWD at three different time intervals (10 mins, 30 mins and 60 mins, respectively). GNSS data for the ZWD at 60 mins time interval is plotted for the same dates (see Figures 3.7–3.10). The GNSS ZWD data were provided by Dionne Hansen from LINZ.

In general, I find a very good agreement between tropospheric data measured with VLBI and GNSS techniques. My results confirm the conclusion of [Teke et al., 2011b] and [Teke et al., 2013]. Also, on the basis of these computations and comparisons, I can conclude that the AUSTRAL sessions are suitable to measure ZWD.
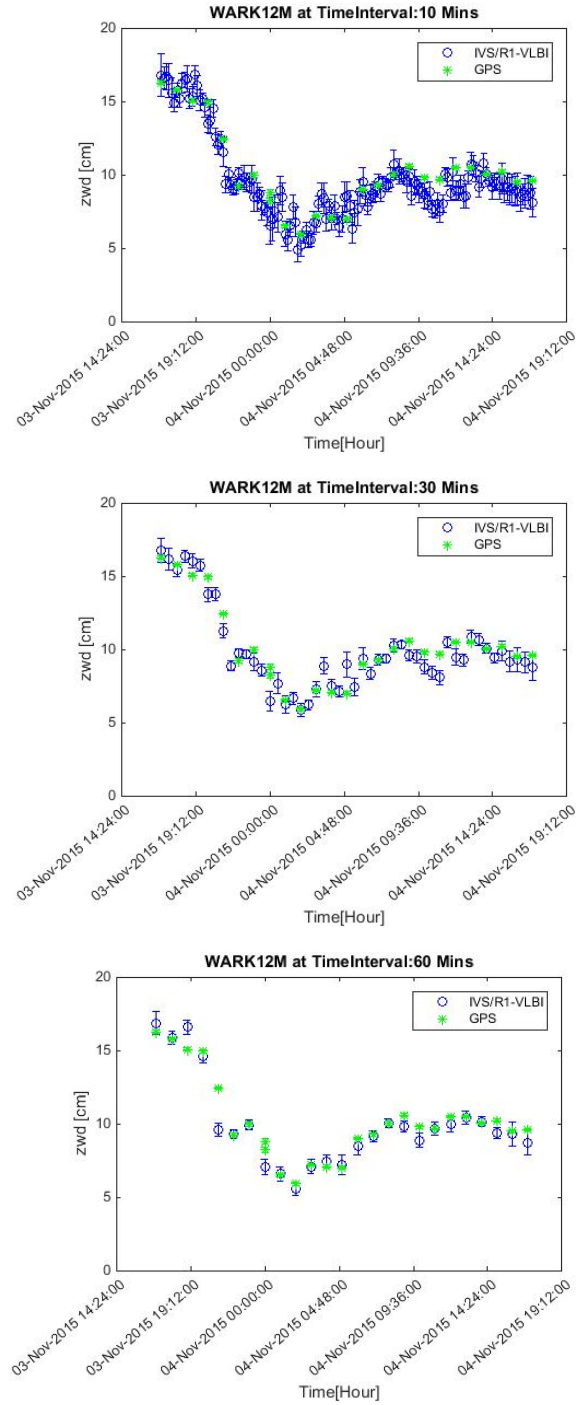
Figure 3.7: Tropospheric ZWD results at WARK12M for the 3rd Nov, 2015. VLBI IVS-R4 session data are presented for three different time intervals (10 mins, 30 mins and 60 mins) in blue. GNSS 60 mins time interval data is presented in green
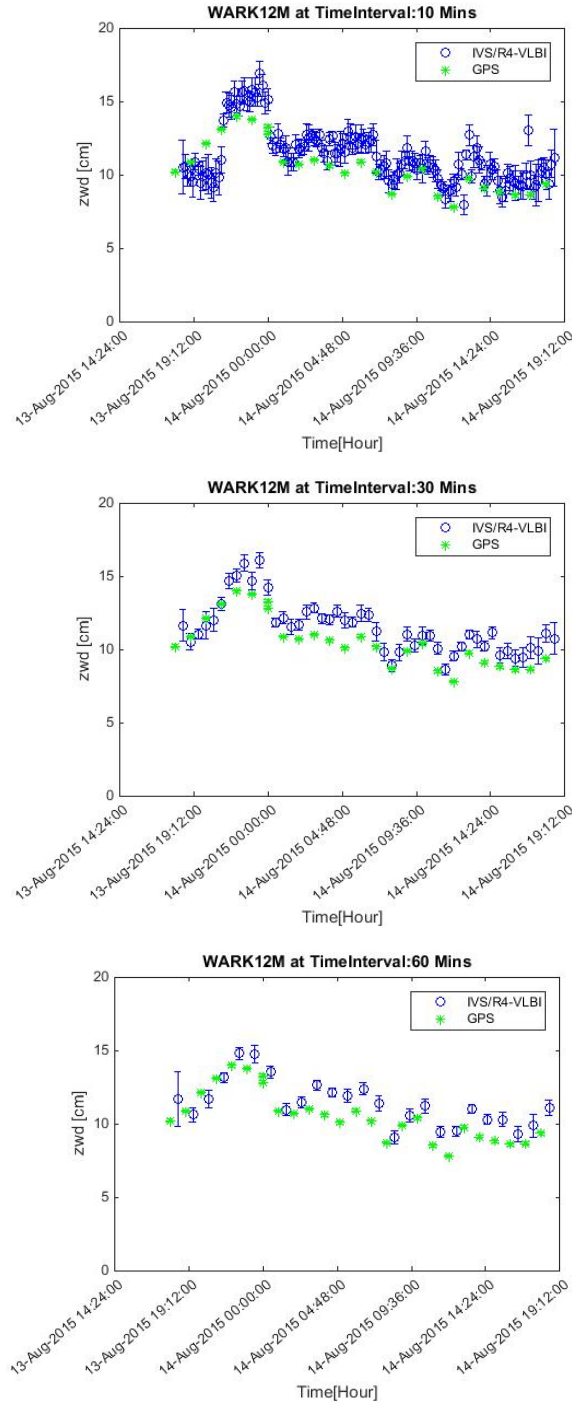
Figure 3.8: Tropospheric ZWD results at WARK12M for the 13th Aug, 2015. VLBI IVS-R4 session data are presented for three different time intervals (10 mins, 30 mins and 60 mins) in blue. GNSS 60 mins time interval data is presented in green
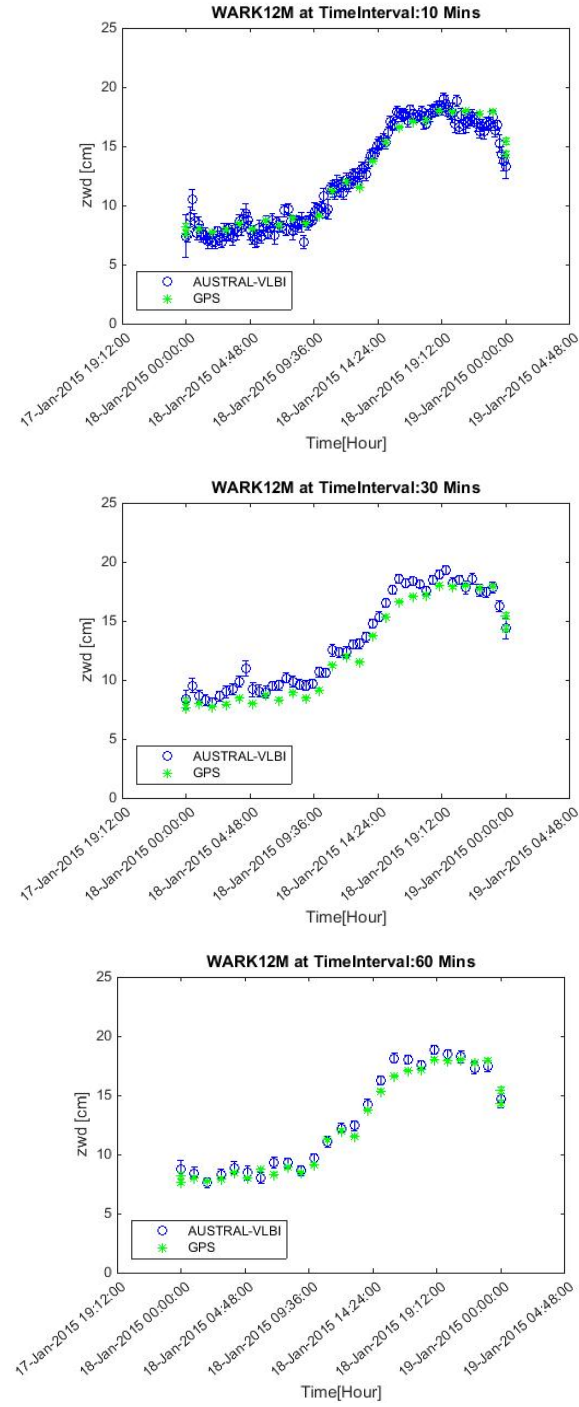
Figure 3.9: Tropospheric ZWD results at WARK12M for the 18th Jan, 2015. VLBI AUSTRAL session data are presented for three different time intervals (10 mins, 30 mins and 60 mins) in blue. GNSS 60 mins time interval data is presented in green
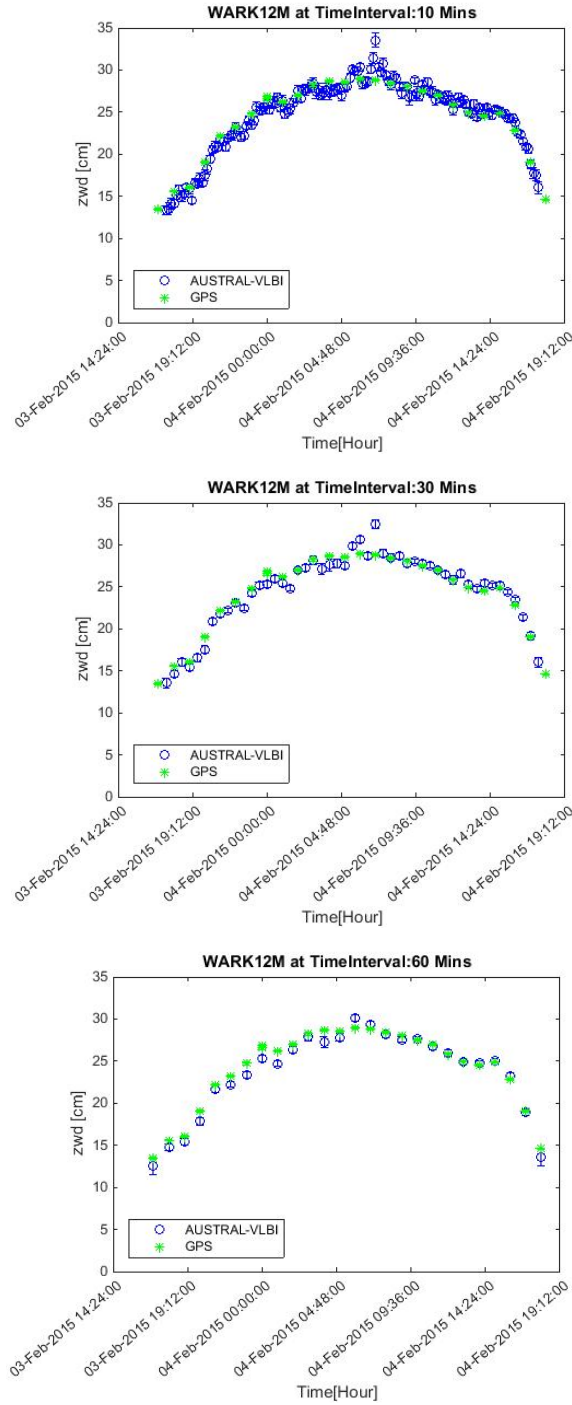
Figure 3.10: Tropospheric ZWD results at WARK12M for the 03rd Feb, 2015. VLBI AUSTRAL session data are presented for three different time intervals (10 mins, 30 mins and 60 mins) in blue. GNSS 60 mins time interval data is presented in green

For 4 typical sessions I estimated the mean error of ZWD measurements. The results are presented in Table 3.1. I conclude here that not only AUSTRAL are suitable for estimating ZWDs, but they even give better (higher accuracy) result, as I have more observations per unit of time. The difference in accuracy between AUSTRAL and IVS sessions is greater for 10 min interval: mean rms = 0.53 and 0.58 cm for AUSTRAL and 0.73 and 0.78 for IVS – see column 3 in Table 3.1.

Table 3.1: Mean errors of troposhperic zenith wet delay (in cm) for IVS-R1/R4 and AUSTRAL sessions with different time intervals.

	Date	10 Mins	30 Mins	60 Mins
IVS-R1	3 Nov 2015	0.73	0.50	0.48
IVS-R4	13 Aug 2015	0.78	0.52	0.50
AUSTRAL	18 Jan 2015	0.58	0.45	0.47
AUSTRAL	3 Feb 2015	0.53	0.41	0.44

As I discussed it, the ZWD obtained from VLBI sessions and GNSS agree well. There are, however, sessions which show a systematic difference between VLBI and GNSS ZWD. For example, for the 31th May, 2015 session the GNSS ZWD is greater than AUSTRAL ZWD by 3-4 cm approximately. I should note a sharp drop existing in ZWD for VLBI AUSTRAL session at 13:00 UTC on 31st May, 2015. This drop is as big as 8-10 cm and it lasts for about 1 hour; then the ZWD returned to the values corresponding to GNSS ZWD (minus 3-4 cm). This drop in AUSTRAL ZWD is clearly seen in the 10-min graph in Figure 3.11. I note another drop at 19:00 UTC on the same day. It may be interpreted as an instability of VLBI data for WARK12M on this date. I conclude that in this case, it was important to consider 10-min graph, because if I only use 60-min graph, I could think that I dealt with just one point outlier. In fact, it was more than one

point, and it was visible on a 10-min graph.

I conclude that some sessions demonstrate instability ("jumps"). These "jumps" in time series of the zenith wet delay may be caused by technical reason, such as, clock breaks which are able to undermine a whole session; or may be caused by the troposphere itself. These fluctuations need to be investigated in the future work.
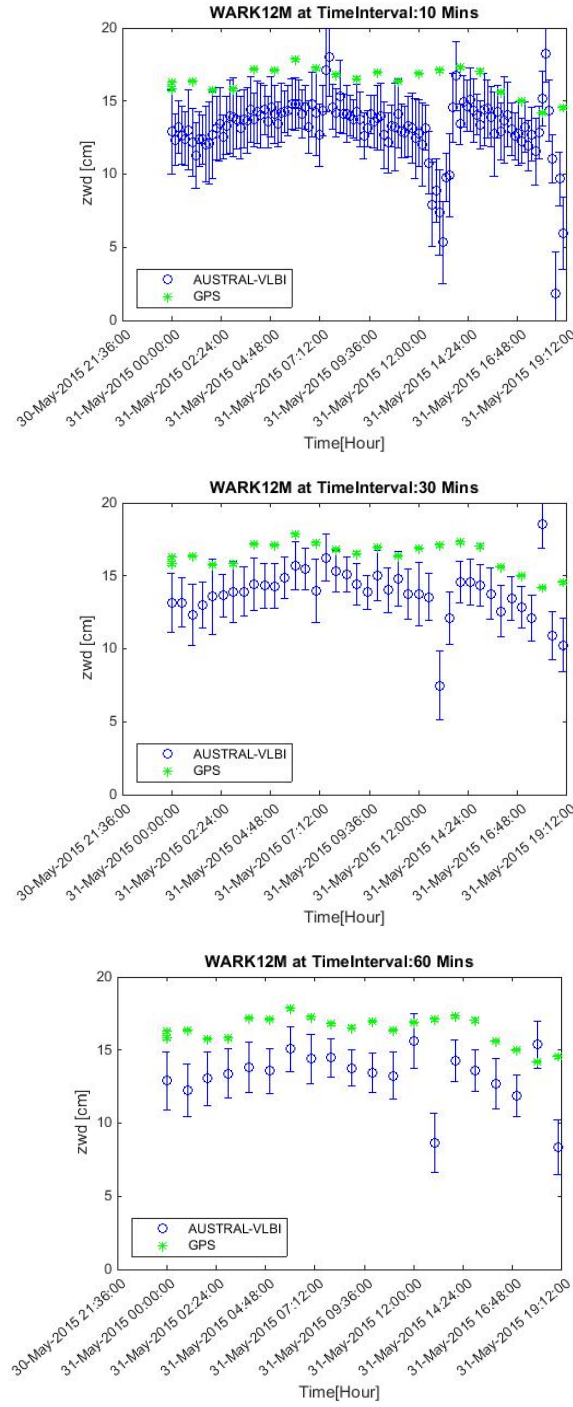
Figure 3.11: Tropospheric ZWD results from VLBI AUSTRAL at three different time intervals (10 mins, 30 mins and 60 mins) in blue and GNSS data at 60 mins time interval in green at WARK12M on 31st May, 2015
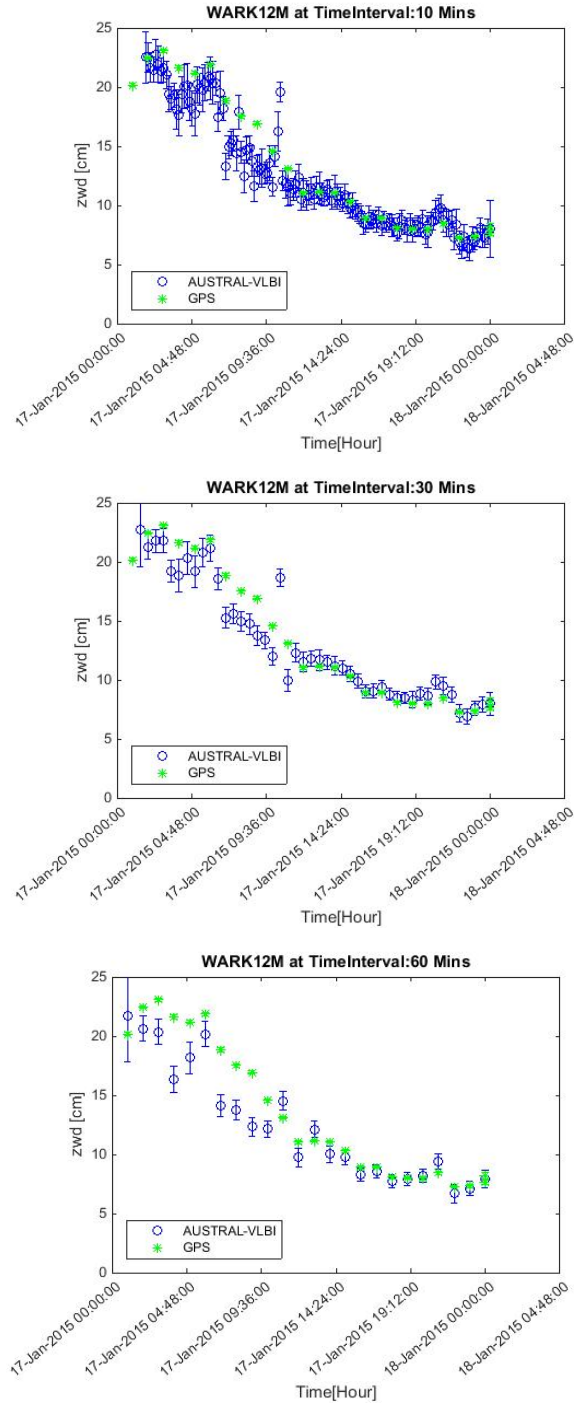
Figure 3.12: Tropospheric ZWD results from VLBI AUSTRAL at three different time intervals (10 mins, 30 mins and 60 mins) in blue and GNSS data at 60 mins time interval in green at WARK12M on 17th Jan, 2015

Chapter 4

Earth Orientation Parameters

The full orientation of the Earth in space is described with a complicated time-dependent function. This function is required for the direct and precise transformation of the VLBI station coordinates from the rotating terrestrial frame to the celestial frame [Schindelegger et al., 2013]. Three time-dependent Euler angles are required to conduct this transformation. In tradition, however, an intermediate reference frame is used with the result that five angles are required for the complete transformation of terrestrial and celestial station positions (this will be discussed in section 4.2). The Earth rotation is parameterized by five EOPs, which can be divided into three categories:

1. Length of Day (LOD) or, equivalently, an universal time parameter $dUT1$, the difference between $UT1$ and uniform atomic time UTC (Universal Time Coordinated);

2. Precession/nutation ($NutdX$, $NutdY$) comprises long-periodic motions of the Earth's rotation axis in a celestial reference system;

3. Polar motion (X_{pol}, Y_{pol}) denotes direction changes of the Earth rotation axis with respect to a body-fixed reference system.

The EOP is a collection of parameters which describe the irregularities of the Earth's rotation. They are the parameters which provide the rotation of the ITRS to the Geocentric Celestial Reference System (GCRS) at the epoch of the observation t [Seitz and Schuh, 2010]. This transformation matrix can be written as [Schuh and Böhm, 2013a]:

$$[GCRS] = Q(t) \cdot R(t) \cdot W(t) \cdot [ITRS] \qquad (4.1)$$

where

$Q(t)$ is the transformation matrix arising from the motion of the celestial pole in the celestial reference system. $Q(t)$ is a function of $NutdX$ and $NutdY$;

$R(t)$ is the transformation matrix arising from the rotation of the Earth around the axis associated with pole, and it is connected with $dUT1$;

$W(t)$ is the transformation matrix arising from the polar motion. It includes as parameters the coordinates X_{pol} and Y_{pol} (polar motion) of the CIP in the Earth-fixed frame and the correction angle s' which locates the position of the Terrestrial Intermediate Origin (TIO) on the equator of the CIP.

Nowadays, precise and actual EOPs are necessarily needed for space navigation of satellites, maintaining time with Earth's rotation. Precision and accuracy of measuring EOPs are provided by modern space geodetic techniques. Geodetic VLBI is the only space-geodetic technique that provides the full set of EOPs, which are important for positioning and navigation on Earth and in space. The VLBI technique uniquely estimates the nutation parameters and the Earth rotation angle ($UT1 - UTC$) directly [Schuh and Böhm, 2013a].

The purpose of the IVS-R1 and R4 sessions is to provide bi-weekly EOPs with medium latency. The 1 and 4 indicate that the sessions are on Mondays and

Thursdays, respectively. The R indicates rapid turnaround because the stations, correlators and analysts have taken the commitment, to make the time from the end of recording to results as short as possible. The turnaround time should be no more than 15 days [IVS, 2008].

4.1 Earth rotation angle $dUT1$

Universal Time is conventionally related to the Greenwich Mean Sidereal Time (GMST). It is used to express the difference $UT1 - TAI$ or $UT1 - UTC$ [Petit and Luzum, 2013c].

International Atomic Time (TAI) is realized by the combination of multiple highly-precise atomic clocks around the world. It is a time scale of the International Bureau of Weights and Measures (BIPM). The origin of TAI is such that $UT1 - TAI$ was about zero on 1st January, 1958. The instability of TAI is 6 orders of magnitude smaller than that of $UT1$ [Petit and Luzum, 2013c]. TAI is not adjusted for leap seconds, it is replaced by the intermediate time scale Coordinated Universal Time (UTC).

In Equation (4.1), matrix $R(t)$ is the Earth rotation matrix with the geocentric angle θ between TIO and CIO. The conventional relationship defining Universal Time 1 (UT1) from the Earth rotation angle θ is [Sovers et al., 1998b]:

$$\theta(T_u) = 2\pi \cdot (0.7790572732640 + 1.00273781191135448 \cdot T_u) \quad (4.2)$$

where

$$T_u = JulianUT1date - 2451545.0 \quad (4.3)$$

$$UT1 = UTC + (UT1 - UTC) \quad (4.4)$$

The difference between $UT1$ and UTC can be observed by VLBI. The *a priori* offset $UT1 - UTC$ is changed as needed to keep UTC within 0.9 seconds of Earth rotation time, $UT1$, leap seconds can be added once or twice a year. The deviation of the actual Earth rotation is:

$$dUT1 = UT1 - UTC \qquad (4.5)$$

$dUT1$ is calculated and distributed by the IERS.

4.2 Precession and nutation

Diverse seasonal variations are caused by the Earth's obliquity to the ecliptic and orbital rotation of the Earth around the Sun. Slow rotation of the Earth's rotational axis around the direction perpendicular to the ecliptic plane with the period of about 26 thousands years is called precession. It has been known since early day astronomy. Another motion in space is called nutation with the main period of 18.6 years, which is periodic perturbation of the direction of the Earth's spin axis. It is much smaller in amplitude than precession and often regarded as associated motion of precession. Both motions (Figure 4.1) are due to the gravitational interaction between the Earth and the Sun (precession) as well as the Earth and the Moon (nutation). The motion of the precession/nutation is determined by VLBI. It gives the offsets in longitude and in obliquity of the celestial pole with respect to its position defined by the conventional IAU precession/nutation models [Na, 2013].
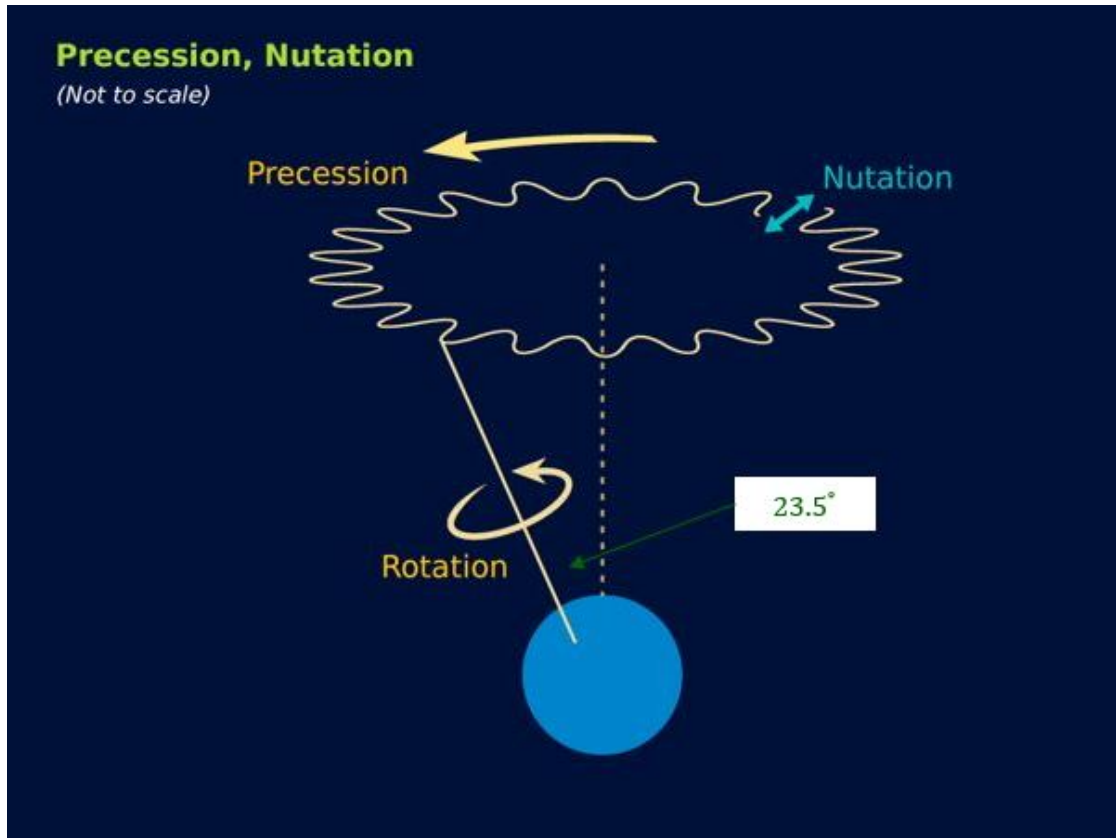
Figure 4.1: Earth precession and nutation (by courtesy of: TES Teach)

By Equation (4.1), the precession/nutation matrix, denoted $Q(t)$, includes the rotations around the angles X and Y which are the coordinates of the CIP in the celestial frame as well as the correction angle s' which positions the CIO on the equator of the CIP. The CIP is the reference pole for space geodetic measurements, it used to define the observed axis [Arora et al., 2011].

The CIP divides the motion of the pole of the ITRS with respect to the GCRS into a celestial part (precession and nutation, $[NutdX, NutdY]$) and a terrestrial part (polar motion $[X_{pol}, Y_{pol}]$). The celestial part includes all motions with periods greater than 2 days observed in the celestial frame, and this corresponds to all frequencies between 0.5 (retrograde) and +0.5 (prograde) cycles per sidereal day

in the GCRS. A conventional precession/nutation model can be calculated by the largest part of the celestial motion of the CIP. The model IAU 2006/2000A is recommended by the IERS Conventions 2010.

4.3 Polar motion

The remaining unmodeled parts of the celestial motion of the CIP can be observed with VLBI as the so-called polar motion (X_{pol}, Y_{pol}). The polar motion is defined as a periodic rotation of the Earth's rotation axis relative to its crust, and it is measured relative to the mean epoch of the ITRF using coordinates X and Y [Petit and Luzum, 2013b]. The polar motion is made up of three major components: two periodic oscillations and an irregular drift in the direction of the 80th meridian west, which has lately been shifted toward the east. Two periodic oscillations are presented by a free oscillation (Chandler wobble) with a period of about 435 days and the other is an annual oscillation [Adhikari and Ivins, 2016]. The polar motion is monitored by the IVS and provided by the IERS.

4.4 EOPs for IVS-R1/R4 sessions and AUSTRAL sessions

In this section, I determine the Earth orientation parameters on the basis of IVS-R1/R4 sessions and AUSTRAL sessions. I present the results of our computations in terms of residuals between the observed parameters and predicted (*a priori*) model parameters. These models are listed in the IERS Conventions.

Using VieVS, EOPs can be estimated for arbitrary estimation intervals with specified constraints in *Estimation-Least squares-EOP* (Figure 4.2).
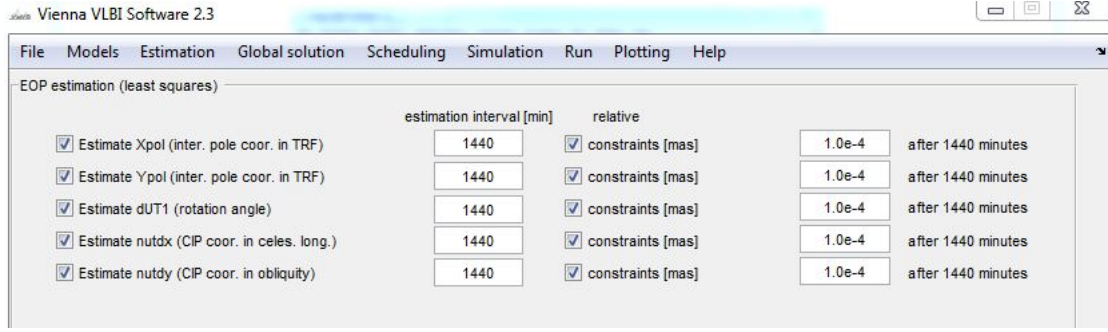
Figure 4.2: EOP estimation in VieVS

Measurement points with large errors (>5 mas for X_{pol}, Y_{pol}, $NutdX$, and $NutdY$; as well as >5 ms for $dUT1$) were regarded as outliers and were excluded from the figures. Figure 4.3 shows my results for five EOPs for IVS-R1/R4 and AUSTRAL sessions for the period of four years from 2012 to the beginning of 2016. According to [Malkin, 2009], both the accuracy and precision of measured EOPs is strongly correlated with the size of the observing network. Therefore, I can expect that the errors of AUSTRAL EOPs data should be greater than the errors of global IVS R-sessions. This is exactly what I see in Figure 4.3.

According to [Plank et al., 2016], the errors of X_{pol} and Y_{pol} are about five times larger for AUSTRAL than for IVS-R1/R4 sessions, and the errors for precession/nutation are two times larger. Taken longer East-West baselines into consideration, one might expect better results for estimates of $dUT1$ because the longer baselines are capable to measure the $dUT1$ with a better accuracy. Table 4.1 presents the RMS of EOPs for the AUSTRAL sessions and the global IVS sessions. I can see that the regional (AUSTRAL) sessions do not suit well for polar motion (X_{pol}, Y_{pol}) study, as the standard deviations show that the AUSTRAL sessions are about 4 times greater than for the IVS R-sessions. The difference between these two different types of seesions for $dUT1$ and pression/nutation ($NutdX$, $NutdY$) show that the accuracy of the AUSTRAL sessions is only twice as bad as the IVS

R1/R4 sessions, which confirms the conclusion made in [Plank et al., 2016].

Table 4.1: The RMS of the EOP for the AUSTRAL sessions and the IVS-R sessions from the period of 2012 to 2016.

EOP	R1R4	AUSTRAL	Ratio (AUSTRAL/R1R4)
	RMS	RMS	RMS
X_{pol}	0.33	1.47	4.45
Y_{pol}	0.55	1.50	2.73
dUT1	0.05	0.09	1.80
NutdX	0.41	0.60	1.50
NutdY	0.35	0.66	1.89

Also, I fixed X_{pol} and Y_{pol} in VieVS and calculated the RMS of $dUT1$ and $NutdX$, $NutdY$ for the AUSTRAL sessions and the IVS-R1/R4 sessions. Figure 4.4 presents the lower $dUT1$ RMS scatter of AUSTRAL sessions. The RMS values are presented in Table 4.2. The RMS (ratio of AUSTRAL devided by R1R4) of $dUT1$ in the AUSTRAL sessions show only 1.3 times larger than for the IVS R-sessions when polar motion are fixed. Meanwhile, the ratio of $NutdX$ and $NutdY$ are reduced to 1.25 and 1.52, respectively.

Table 4.2: The RMS of $dUT1$ and $NutdX$, $NutdY$ for the AUSTRAL sessions and the IVS-R sessions from the period of 2012 to 2016.

EOP	R1R4	AUSTRAL	Ratio (AUSTRAL/R1R4)
	RMS	RMS	RMS
dUT1	0.03	0.04	1.33
NutdX	0.36	0.45	1.25
NutdY	0.31	0.47	1.52

I can conclude that the RMS of EOPs in AUSTRAL sessions show worse result than the IVS-R sessions. This can be explained by the fact that AUSTRAL sessions include small number of stations, all in the southern hemisphere, therefore, not balanced in terms of distribution around the globe. The more stations are involved and the more regular is the distribution of IVS stations on the globe, the higher the accuracy of EOPs determined in these sessions [Malkin, 2009].
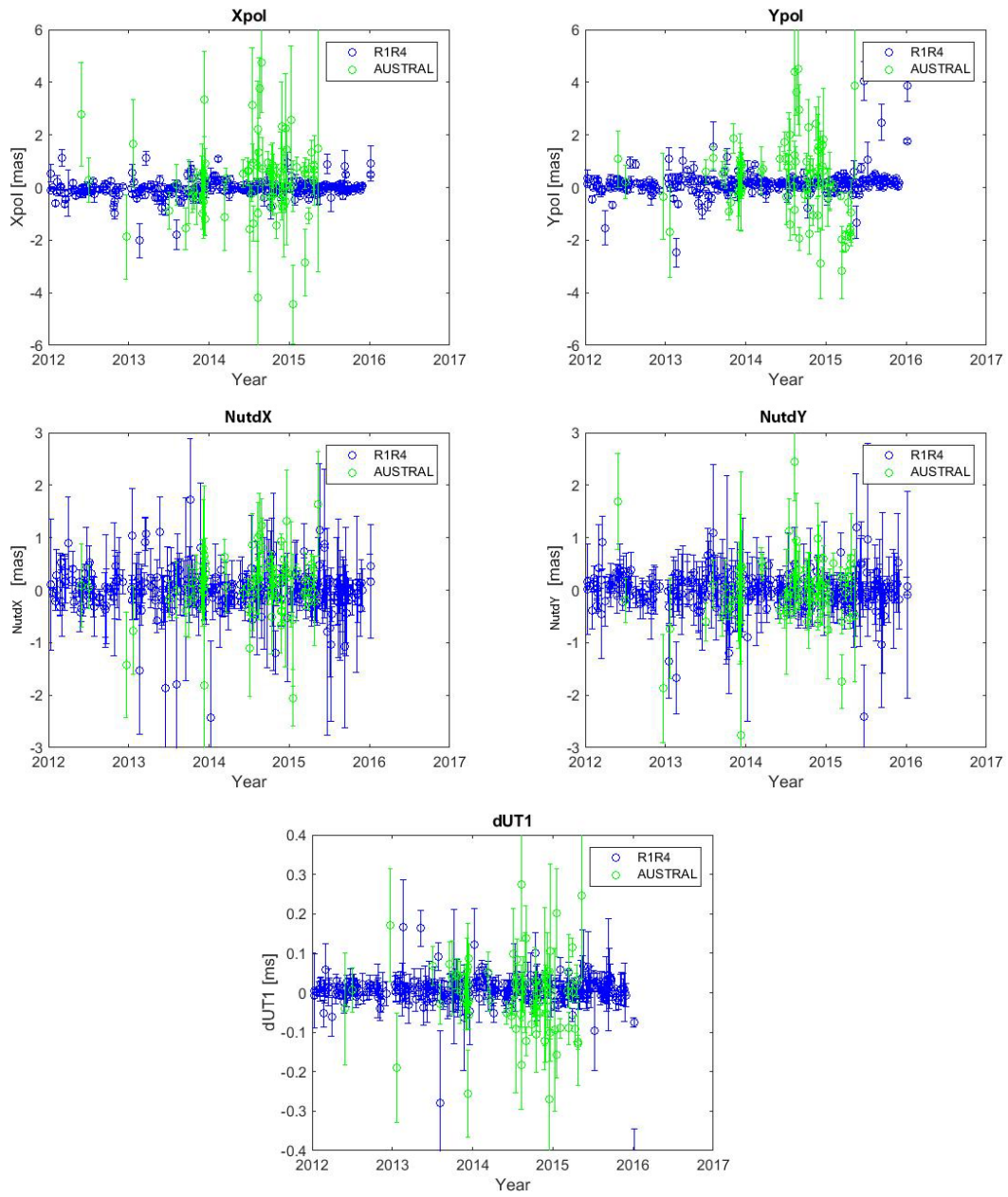
Figure 4.3: Earth Orientation Parameters (EOP) for the regional AUSTRAL (green) and the global IVS-R sessions (blue)
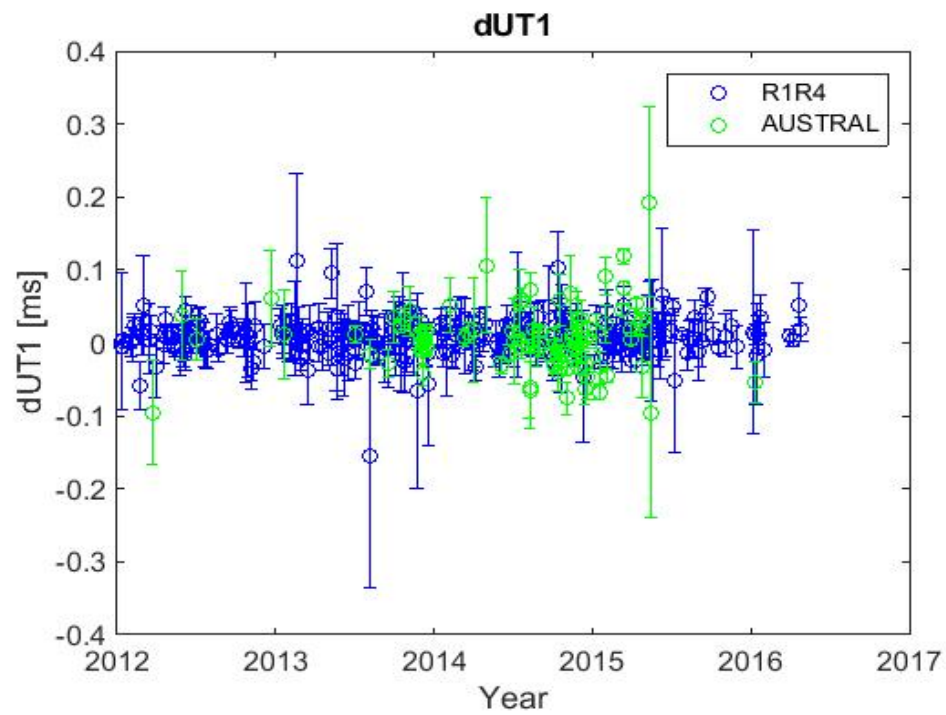
Figure 4.4: The polar motion fixed dUT1 for the regional AUSTRAL (green) and the global R-sessions (blue)

Chapter 5

Conclusion

Contribution of the southern hemisphere geodetic VLBI stations in the IVS expanded significantly since the AUSTRAL VLBI program started in year 2011. In this thesis, I tried to estimate the importance and contribution of the AUSTRAL geodetic VLBI network in global and regional space geodesy.

Though theoretical (*a priori*) models for AUSTRAL stations exist, they are based on short time series. For example, the ITRF2014 model is based on a 2-year VLBI observations in the beginning of AUSTRAL stations when observations were not regular and the time series were sparse, so errors in determination of station velocities were large – see e.g., time series for WARK12M (Figure 2.3) and for HART15M (Figure 2.7). Therefore, it was important to include two more years of observations (up to mid-2016) and to test how accurate were the theoretical models (station coordinates and velocities) of AUSTRAL stations.

In this thesis, I used VLBI observations of AUSTRAL sessions, as well as observations of global IVS-R1/R4 sessions where the AUSTRAL VLBI network stations participated. I investigated the period from 2012 to mid 2016. To process these VLBI data, I used the VieVS developed by the Geo-department, Vienna University of Technology.

In Chapter 2, I computed the observed (VLBI) station geographic locations and velocities, and compared them with existing model (*a priori*) locations and velocities. I found some discrepancies between observations and models when analysing residuals (observed minus theoretical). The discrepancies became more obvious when I converted from geocentric (XYZ) coordinates to local horizontal coordinates (NEU). For example, I studied specifically the behaviour of NEU residuals for Warkworth VLBI station (WARK12M). I found that during year 2015 the Up-residual dropped by $\sim$2 cm. I considered the Up-coordinate of the co-located WARK GNSS station, and found that the GNSS location did not show systematic motion during 2015. I involved the Local Tie Survey 2014 and 2015 data, which also did not show any noticeable motion of the radio telescope with respect to the co-located GNSS station during this period. From stability of GNSS station location and stability of radio telescope with respect to GNSS station (local tie survey), I concluded that a possible explanation of -2.0 cm/yr Up-residual drop is that the theoretical velocities for WARK12M might require correction. By saying this, the errors of VLBI observations are still large, so I suggested that more data should be collected before I make a reliable conclusion with respect to the theoretical model suitability.

I computed the ITRF2014 velocities of VLBI stations and co-located GNSS stations. I calculated the observed weighted velocities, then I calculated and compared velocity residuals (observed minus theoretical) for ITRF2014 and VieTrf13. I found that the theoretical (model) velocities of VLBI ITRF2014 (ITRF2014-IVS) are close to my observed VLBI velocities.

Furthermore, I computed the VLBI and GNSS baseline rates of change for each AUSTRAL baseline. I found that more observations are needed to judge about suitability of theoretical models for these AUSTRAL stations. For example, results for the baseline Hb-Ke presented quite different for VLBI and GNSS: 0.3 ± 0.1

mm/yr for the ITRF2014-IGS compared to 4.0 ± 0.3 mm/yr predicted by the ITRF2014-IVS and 3.0 ± 0.7 mm/yr of the VieTrf13. The difference between GNSS and VLBI models are statistically significant. The AUSTRAL observations which I calculated showed 2.3 ± 1.9 mm/yr baseline rate of change. The VLBI observation error is large. Given ± 1.9 mm/yr is a 1σ error, which means the 3σ error is huge ± 5.7 mm/yr, I could not say whether the difference between VLBI observations and GNSS result for this baseline is statistically significant or not.

I can conclude, therefore, that the AUSTRAL array is still a relatively new array, time series for AUSTRAL stations are not long enough to be used for accurate prediction of station motions and coordinates, so the models for the AUSTRAL stations might not be perfect. The models for the AUSTRAL stations, will probably need to be adjusted, but I recommend that more VLBI observations to be conducted in the future, before the final conclusion is made.

The troposphere is a layer of the Earth atmosphere, which is responsible for delay of radio signals propagating through this layer. Because the state of troposphere is different in different geographic locations and it is time-dependent, the tropospheric delay is considered to be one of the most important error sources for space geodetic techniques relying on radio signals from space.

In Chapter 3, I investigated the tropospheric ZWD for AUSTRAL stations. In particular, I focused on the Warkworth GGOS station, which has both VLBI telecopes and co-located GNSS receiver. I compared the ZWD results obtained with VLBI technique vs. the ZWD results based on GNSS measurements. Using VieVS, I processed data for AUSTRAL stations from the AUSTRAL sessions and the IVS-R1/R4 sessions from 2012-2016. ZWD data for the co-located GNSS station was provided to us by LINZ.

I conclude that in general the AUSTRAL sessions are suitable to measure ZWD.

This conclusion is based on my finding that in most cases ZWD results from two geodetic techniques (VLBI and GNSS) agree well. However, in some cases VLBI data showed large ZWD fluctuations during one session, these fluctuations were not present in GNSS results. These fluctuations need to be investigated in the future work.

I also discussed seasonal variations (signals) of the ZWD. My AUSTRAL VLBI results showed that some stations present significant seasonal ZWD variations. For example, KATH12M, shows seasonal ZWD variations ranging from 5 cm in winter to 30-40 cm in summer. So the amplitude of the ZWD signal (seasonal variation) reaches $\sim$30 cm. I noted that annual variation amplitude of the ZTD provided by [Jin et al., 2007] is $\sim$ 10 cm for GNSS station co-located with KATH12M. This discrepancy need to be investigated in the future work.

In Chapter 4, I estimated the accuracy of the EOPs that can be derived from the AUSTRAL VLBI observations. It was clear that EOPs which require global distribution of VLBI stations polar motion, precession and nutation should show smaller errors (higher accuracy) for global sessions rather than for regional AUS-TRAL sessions. So I computed EOPs for the AUSTRAL sessions, as well as for the IVS-R1/R4 sessions where the AUSTRAL stations participated. As it was expected, the errors of polar motion (X_{pol}, Y_{pol}) were about 4 times greater for the AUSTRAL sessions than for the IVS-R1/R4 sessions. The accuracy for precession/nutation parameters was different by the factor of 2. However, my main interest was focused on the $dUT1$ parameter.

$dUT1$ is extremely important time correction which is obtained from VLBI only. GNSS uses this VLBI product to correct GNSS satellite orbits. I fixed the polar motion and calculated the standard deviation of $dUT1$ for both the AUSTRAL sessions and the IVS-R1/R4 sessions. I found that, the errors of the AUSTRAL

sessions are similar to (just 1.3 times greater than) the errors of the global IVS-R1/R4 sessions.

There is discussion currently whether AUSTRAL array can be used efficiently to determine $dUT1$ given a considerably long East-West baseline of the AUSTRAL network. Possibly more efficient scheduling can be applied to increase $dUT1$ accuracy and decrease time needed to produce $dUT1$. This will be done in the future work.

Overall, I demonstrate that AUSTRAL geodetic VLBI network plays an important role in space geodesy and in particular in the IVS. AUSTRAL geodetic VLBI network demonstrates a great example of GGOS geodetic network when data from co-located techniques can be compared and important geodetic information can be obtained for future studies.

Abbreviations

AUT   Auckland University of Technology

BIPM   International Bureau of Weights and Measures

CCIVS IVS Combination Center

CIO   Celestial Intermediate Origin

CIP   Celestial Intermediate Pole

CPWLO Continuous Piece-Wise Linear Offsets

CRF   Celestial Reference Frame

DBBC   Digital Base Band Converter

DORIS Doppler Orbitography and Radio-Positioning by Integrated Satellite

ECEF   Earth Center Earth Fixed

ECMWF European Center for Medium-Range Weather Forecasts

EOPs   Earth Orientation Parameters

GCRS   Geocentric Celestial Reference System

GGOS   Global Geodetic Observing System

GLONASS Russian Globalnaja Nawigazionnaja Sputnikowwaja Sistema

GMST Greenwich Mean Sidereal Time

GNS Science Geological and Nuclear Science Research Institute

GNSS Global Navigation Satellite Systems

GPS Global Positioning System

GUI Graphical User Interface

IAG International Association of Geodesy

IAU International Astronomical Union

ICRF International Celestial Reference Frame

ICRS International Celestial Reference System

IERS International Earth Rotation and Reference System Service

IMF Isobaric Mapping Function

IRASR Institute for Radio Astronomy and Space Research

ITRF International Terrestrial Reference Frame

ITRS International Terrestrial Reference System

IUGG International Union of Geodesy and Geophysics

IVS International VLBI Service for Geodesy and Astrometry

LINZ Land Information New Zealand

LOD Length of Day

LSM   Least-Square Adjustment

NGS   Next Generation Sequencing

NICT   National Institute of Information and Communications Technology

NMF   Neil Mapping Function

NZGD2000 New Zealand Geodetic Datum 2000

PWLO Piece-Wise Linear Offsets

SEFD   System Equivalent Flux Density

SLR   Satellite Laser Ranging

TAI   International Atomic Time

TIO   Terrestrial Intermediate Origin

TRF   Terrestrial Reference Frame

UT1   Universal Time 1

UTC   Coordinated Universal Time

VGOS VLBI Global Observing System

VieTrf13 Vienna Terrestrial Reference Frame

VieVS Vienna VLBI Software

VLBI   Very Long Baseline Interferometry

VMF1 Vienna Mapping Function 1

WRMS Weighted Root Mean Square

WVR   Water Vapor Radiometer

ZHD   Zenith Hydrostatic Delay

ZTD   Zenith Total Delay

ZWD   Zenith Wet Delay

List of Figures

List of Tables

Bibliography

Adhikari, S. and Ivins, E. R. (2016). Climate-driven polar motion: 2003-2015. *Science Advances*, 2(4):e1501693. `http://dx.doi.org/10.1126/sciadv.1501693`.

Altamimi, Z., Rebischung, P., Métivier, L., and Collilieux, X. (2016). ITRF2014: A new release of the International Terrestrial Reference Frame modeling nonlinear station motions. *Journal of Geophysical Research: Solid Earth*, 121(8):6109–6131.

Arora, K., Cazenave, A., Engdahl, E. R., Kind, R., Manglik, A., Roy, S., Sain, K., Uyeda, S., and Gupta, H. (2011). *Encyclopedia of Solid Earth Geophysics*. Springer Science. `http://dx.doi.org/10.1007/978-90-481-8702-7`.

AuScope (2015). *The Infrastucture System.* url http://www.auscope.org.au/system/.

Bachmann, S., Thaller, D., Roggenbuck, O., Lösler, M., and Messerschmitt, L. (2016). IVS contribution to ITRF2014. *Journal of Geodesy.* `http://dx.doi.org/10.1007/s00190-016-0899-4`.

Behrend, D., Haas, R., D, P., Gradinarsky, L. P., Keihm, S. J., Schwarz, W., Cucurull, L., and Rius, A. (2002). MM5 derived ZWDs compared to observational results from VLBI, GPS and WVR. *Physics and Chemistry of the Earth, Parts A/B/C*, 27(4):301–308.

Blick, G. and Sarib, R. (2010). The Geodetic Infrastructure in Australia and New Zealand: Differences and Similarities. `https://www.fig.net/resources/proceedings/fig_proceedings/fig2010/papers/ts07c/ts07c_blick_sarib_4065.pdf`.

Böhm, J. (2007). *Tropospheric delay modelling at radio wavelengths for space geodetic techniques.* Inst. of the Course on "Geodesy and Geoinformation" of the Vienna University of Technology.

Böhm, J. (2014a). Least squares adjustment in VLBI. In *VieVS-Wiki*.

Böhm, J. (2014b). *Overview of VIE LSM.* `http://vievs.geo.tuwien.ac.at/doku.php?id=public:vievs_manual:estimation&s[]=least&s[]=square`.

Böhm, J., Böhm, S., Nilsson, T., Pany, A., Plank, L., Spicakova, H., Teke, K., and Schuh, H. (2012). The new Vienna VLBI Software VieVS. In *Geodesy for Planet Earth*, volume 136 of *International Association of Geodesy Symposia*, pages 1007–1011. Springer-Verlag Berlin Heidelberg. `http://link.springer.com/chapter/10.1007/978-3-642-20338-1_126/fulltext.html`.

Böhm, J., Krásná, H., Böhm, S., Choliy, V., Hellerschmied, A., Hofmeister, A., Karbon, M., Mayer, D., McCallum, J., Madzak, M., Nilsson, T., Plank, L., Shabala, S., Soja, B., Sun, J., and Teke, K. (2014a). Vienna VLBI Software: Current release and plans for the future.

Böhm, J., Krásná, H., Böhm, S., Choliy, V., Hellerschmied, A., Hofmeister, A., Karbon, M., Mayer, D., McCallum, J., Madzak, M., Nilsson, T., Plank, L., Shabala, S., Soja, B., Sun, J., and Teke, K. (2014b). Vienna VLBI Software: Current release and plans for the future. pages 258–261. `ftp://ivscc.gsfc.nasa.gov/pub/general-meeting/2014/pdf/055_Bohm_etal.pdf`.

Böhm, J., Niell, A., Tregoning, P., and Schuh, H. (2006a). Global Mapping Function (GMF): A new empirical mapping function based on numerical weather model data. *Geophysical Research Letters*, 33(7).

Böhm, J. and Schuh, H. (2007). Troposphere Gradients from the ECMWF in VLBI analysis. *Journal of Geodesy*, 81(6-8):403–408. `http://dx.doi.org/10.1007/s00190-006-0126-9`.

Böhm, J. and Schuh, H. (2012). *Science of Geodesy II: Geodetic Principle*. Springer Science.

Böhm, J. and Schuh, H. (2014). Vienna Mapping Functions in VLBI analyses. *Geophysical Research Letters*, 31(1).

Böhm, J. and Schuh, H. (2015). *Least-squares adjustment in VLBI*. `http://vievs.geo.tuwien.ac.at/doku.php?id=public:vlbi_fundamantals:least_squares_adjustment`.

Böhm, J., Werl, B., and Schuh, H. (2006b). Troposphere Mapping Functions for GPS and Very Long Baseline Interferometry from European Centre for Medium-Range Weather Forecasts Operational Analysis Data. *Journal of Geophysical Research: Solid Earth*, 111(B2). `http://dx.doi.org/10.1029/2005JB003629`.

Cai, G. W., Chen, B. M., and Lee, T. H. (2011). Coordinate systems and transformations. In *Unmanned Rotorcraft Systems*, pages 23–34. Springer.

Gentle, P. (2016). *WARK GNSS Vertical Component Time Series*. `http://fits.geonet.org.nz/plot?networkID=LI&siteID=WARK&typeID=u`.

GGOS (2011). Geodetic Reference Frames. `http://www.ggos-portal.org/lang_en/GGOS-Portal/EN/Topics/GeodeticApplications/`

`GeodeticReferenceSystemsAndFrames/GeodeticReferenceFrames/`
`GeodeticReferenceFrames.html`.

GNS (2016). *NZ's Plate Boundary Zone.* `https://www.gns.cri.nz/Home/`
`Our-Science/Earth-Science/Plate-Tectonics/NZ-plate-boundary`.

GPS (2012). *Schematic Plot Showing How GPS Measures Atmospheric Precipitable Water (PW).* `http://xenon.colorado.edu/spotlight/index.php?product=`
`spotlight&station=sg05`.

Gulyaev, S. and Natusch, T. (2009). New Zealand 12-m VLBI station. *International VLBI service for geodesy and astrometry*, pages 138–141.

Gulyaev, S., Natusch, T., and Weston, S. (2011). Radio Astronomical Observatory at Warkworth, New Zealand. `http://dx.doi.org/978-1-4244-6051-9/11`.

Gulyaev, S., Natusch, T., and Wilson, D. (2010). Characterisation and calibration of the 12-m antenna in Warkworth, New Zealand. In *The 5th IVS General Meeting Proc.*

Hellerschmied, A. (2015). VieVS MOD. In *VieVS User Workshop.* `http://vievs.geo.tuwien.ac.at/lib/exe/fetch.php?media=public:`
`user_workshop:2015:WS2015_VieMod_Hellerschmied.pdf`.

IVS (2008). IVS-R1 and IVS-R4. In *IVS Observing Program.* `http://ivs.nict.`
`go.jp/mirror/program/descrip2008.html`.

IVS, C. C. (2016). VLBI Baseline. `http://www.ccivs.bkg.bund.de/EN/`
`Quarterly/VLBI-Baseline/vlbi-baseline_node.html`.

Jacobs, C. S., Arias, F., Boboltz, D., Böhm, J., Bolotin, S., Bourda, G., Charlot, P., De Witt, A., Fey, A., and Gaume, R. (2013). The ICRF-3: Proposed roadmap

to the next generation international celestial reference frame. page 1. `http://syrte.obspm.fr/journees2013/powerpoint/jacobs_jsr13.pdf`.

Jin, S. G., Park, J. U., Cho, J. H., and Park, P. H. (2007). Seasonal variability of GPS-derived zenith troposhperic delay (1994-2006) and climate implications. *Journal of Geophysical Research: Atmospheres*, 112(d9). `http://onlinelibrary.wiley.com/doi/10.1029/2006JD007772/full`.

Kásná, H., Böhm, J., Plank, L., Nilsson, T., and Schuh, H. (2014). Atmospheric effects on VLBI-derived terrestrial and celestial reference frames. In *Earth on the Edge: Science for a Sustainable Planet*, pages 203–208. Springer.

Krásná, H. and Mayer, D. (2015). VieVS GLOB. In *VieVS User Workshop*. `http://vievs.geo.tuwien.ac.at/lib/exe/fetch.php?media=public:user_workshop:2015:WS2015_VieGlob_Mayer.pdf`.

Kwak, Y. (2015). VieVS INIT. In *VieVS User Workshop*. `http://vievs.geo.tuwien.ac.at/lib/exe/fetch.php?media=public:user_workshop:2015:WS2015_vie_init_Kwak.pdf`.

Lovell, J., Dickey, J., Reid, B., McCallum, J., Shabala, S., Watson, C., Ellingsen, S., and Memin, A. (2013). AuScope VLBI Project and Hobart 26-m Antenna.

Malkin, Z. (2009). On comparison of the Earth Orientation Parameter obtained from different VLBI network and observing programs. *Journal of Geodesy*, 83(6):547–556. `http://dx.doi.org/10.1007/s00190-008-0265-2`.

Mayer, D. (2015). VieVS SCHED. In *VieVS User Workshop*. `http://vievs.geo.tuwien.ac.at/lib/exe/fetch.php?media=public:user_workshop:2015:WS2015_VieSched_Mayer.pdf`.

Na, S. H. (2013). Earth Rotation - Basic Theory and Features.

Nickola, M., Gaylard, M., Quick, J., and Combrinck, L. (2013). Hartebeesthoek Radio Astronomy Observatory (HartRAO).

Nilsson, T., Böhm, J., Wijaya, D. D., Tresch, A., Nafisi, V., and Schuh, H. (2013). Path delay in the neutral atmosphere. In *Atmospheric Effects in Space Geodesy*, pages 73–136. Springer. `http://dx.doi.org/10.1007/978-3-642-36932-2`.

Palmer, J. (2010). PositioNZ-PP-A GPS Post-Processing Service for New Zealand.

Petit, G. and Luzum, B. (2010a). IERS conventions (2010): Conventional Celestial Reference System and Frame. Technical report, DTIC Document. `http://www.iers.org/SharedDocs/Publikationen/EN/IERS/Publications/tn/TechnNote36/tn36_021.pdf?__blob=publicationFile&v=1`.

Petit, G. and Luzum, B. (2010b). IERS conventions (2010): Terrestrial Reference Systems and Frames. Technical report, DTIC Document. `http://www.iers.org/SharedDocs/Publikationen/EN/IERS/Publications/tn/TechnNote36/tn36_031.pdf?__blob=publicationFile&v=1`.

Petit, G. and Luzum, B. (2013a). The International Terrestrial Reference System (ITRS). `http://www.iers.org/IERS/EN/DataProducts/ITRS/itrs.html`.

Petit, G. and Luzum, B. (2013b). Polar motion. `https://www.iers.org/IERS/EN/Science/EarthRotation/PolarMotion.html;jsessionid=AF6399FF1FA93696F9DF9C84E469AA6D.live2?nn=12932`.

Petit, G. and Luzum, B. (2013c). Universal Time (UT1) and Length of Day (LOD). `https://www.iers.org/IERS/EN/Science/EarthRotation/UT1LOD.html`.

Petrachenko, W., Behrend, D., Hase, H., Ma, C., Niell, A., Schuh, H., and Whitney, A. (2013). The VLBI2010 Global Observing System (VGOS). In *EGU General Assembly Conference Abstracts*, volume 15, page 12867.

Petrovski, I. G. and Tsujii, T. (2012). *Digital Satellite Navigation and Geophysics: A Practical Guide with GNSS Signal Simulator and Receiver Laboratory.* Cambridge University Press. `http://dx.doi.org/978-0-521-76054-6`.

Plank, L. (2013). Vlbi satellite tracking for the realization of frame ties. *Veröffentlichungen des Departments für Geodäsie und Geoinformation, Vienna University of Technology, Geowissenschaftliche Mitteilungen*, 95.

Plank, L. (2014). The impact of the AuScope VLBI observations and the regional AUSTRAL sessions on the TRF.

Plank, L., Lovell, J., McCallum, J., Mayer, D., Reynolds, C., Quick, J., Weston, S., Titov, O., Shabala, S., Böhm, J., Natusch, T., Nickola, M., and Gulyaev, S. (2016). The AUSTRAL VLBI observing program. *Journal of Geodesy*, pages 1–15. `http://link.springer.com.ezproxy.aut.ac.nz/article/10.1007/s00190-016-0949-y`.

Plank, L., Lovell, J. E., McCallum, J., Rastorgueva-Foi, E., Shabala, S. S., Böhm, J., Mayer, D., Sun, J., Titov, O., and Weston, S. (2015a). Results from the Regional AUSTRAL VLBI Sessions for Southern Hemisphere Reference Frames.

Plank, L., Shabala, S., and Böhm, J. (2015b). VieVS SIM. In *VieVS User Workshop.* `http://vievs.geo.tuwien.ac.at/lib/exe/fetch.php?media=public:user_workshop:2015:WS2015_Vie_SIM_JBoehm.pdf`.

Rothacher, M., Drewes, H., Nothnagel, A., and Richter, B. (2010). Integration of Space Geodetic Techniques as the Basis for a Global Geodetic-Geophysical Observing System (GGOS-D). In *System Earth via Geodetic-Geophysical Space Techniques*, pages 529–537. Springer.

Schindelegger, M., Böhm, S., Böhm, J., and Schuh, H. (2013). Atmospheric Effects on Earth Rotation. In Böhm, J. and Schuh, H., editors, *Atmospheric*

Effects in Space Geodesy, pages 181–231. Springer. `http://dx.doi.org/10.1007/978-3-642-36932-2_6`.

Schuh, H. and Behrend, D. (2012). VLBI: a fascinating technique for geodesy and astrometry. *Journal of Geodynamics*, 61:68–80.

Schuh, H. and Böhm, J. (2013a). Earth Orientation. In Xu, G. C., editor, *Science of Geodesy - II: Innovations and Future Developments*. Springer. `http://dx.doi.org/10.1007/978-3-642-28000-9_7`.

Schuh, H. and Böhm, J. (2013b). Very Long Baseline Interferometry for Geodesy and Astrometry. In Xu, G. C., editor, *Science of Geodesy - II: Innovations and Future Developments*. Springer. `http://dx.doi.org/10.1007/978-3-642-28000-9_7`.

Schuh, H. and Böhm, J. (2013c). Very Long Baseline Interferometry for Geodesy: Troposphere Delay Modelling. In Xu, G. C., editor, *Science of Geodesy - II: Innovations and Future Developments*. Springer.

Seitz, F. and Schuh, H. (2010). Earth Rotation. In Xu, G. C., editor, *Science of Geodesy - I: Advances and Future Advances*. Springer. `http://dx.doi.org/10.1007/978-3-642-11741-1`.

Sovers, O. J., Fanselow, J. L., and Jacobs, C. S. (1998a). Astrometry and Geodesy with Radio Interferometry: Experiments, Models, Results. Atmospheric Delay Models. *Reviews of Modern Physics*, 70(4):1393.

Sovers, O. J., Fanselow, J. L., and Jacobs, C. S. (1998b). Astrometry and Geodesy with Radio Interferometry: Experiments, Models, Results. Geometric Delay Models: Time Information. *Reviews of Modern Physics*, 70(4).

Subirana, J. S., Zornoza, J. M., and Hernandez-Pajares, M. (2011a). Reference Systems and Frames. `http://www.navipedia.net/index.php/Reference_Systems_and_Frames`.

Subirana, J. S., Zornoza, J. M., and Hernandez-Pajares, M. (2011b). Transformations between ECEF and ENU coordinates. `http://www.navipedia.net/index.php/Transformations_between_ECEF_and_ENU_coordinates`.

Szabova, M. and Duchon, F. (2016). Survey of GNSS coordinates systems. *European Scientific Journal*, 12(24).

Takiguchi, H., Weston, S., Natusch, T., and Gulyaev, S. (2013). Warkworth Radio Astronomical Observatory, New Zealand.

Teke, K. and Böhm, J. (2015). VieVS LSM. In *VieVS User Workshop*. `http://vievs.geo.tuwien.ac.at/lib/exe/fetch.php?media=public:user_workshop:2015:WS2015_Vie_LSM_part1_Teke.pdf`.

Teke, K., Böhm, J., Nilsson, T., Schuh, H., Steigenberger, P., Dach, R., Heinkelmann, R., Willis, P., Haas, R., Garcia-Espada, S., Hobiger, T., Ichikawa, R., and Shimizu, S. (2011a). Multi-technique comparison of troposphere zenith delays and gradients during CONT08. *Journal of Geodesy*, 85(7):395–413. `http://dx.doi.org/10.1007/s00190-010-0434-y`.

Teke, K., Böhm, J., Nilsson, T., Schuh, H., Steigenberger, P., Dach, R., Heinkelmann, R., Willis, P., Haas, R., García-Espada, S., Hobiger, T., Ichikawa, R., and Shimizu, S. (2011b). Multi-technique comparison of troposphere zenith delays and gradients during CONT08. *Journal of Geodesy*, 85(7):395–413.

Teke, K., Nilsson, T., Böhm, J., Hobiger, T., Steigenberger, P., García-Espada, S., Haas, R., and Willis, P. (2013). Troposphere delays from space geodetic

techniques, water vapor radiometers, and numerical weather models over a series of continuous VLBI campaigns. *Journal of Geodesy*, 87(10-12):981–1001.

Titov, O. (2009). A new estimator for VLBI baseline length repeatability. *Journal of Geodesy*, 83(11):1041–1049. `http://dx.doi.org/10.1007/s00190-009-0322-5`.

Titov, O., Lovell, J., Takeguchi, H., Quick, J., Shabala, S., McCallum, J., Sun, J., Dawson, J., de Witt, A., and Reynolds, C. (2014). First geodetic results from the Australasian VLBI Network.

Titov, O., Tesmer, V., and Böhm, J. (2004). OCCAM v. 6.0 software for VLBI data analysis. *International VLBI Service for Geodesy and Astrometry*, pages 267–271.

Weston, S., Natusch, T., Woodburn, L., Hart, B., and Gulyaev, S. (2014). New Zealand VLBI station, Warkworth.

Appendix A

AUSTRAL Baseline Lengths Residuals

Figures A.1-A.9 present five AUSTRAL stations residuals for IVS-R1 sessions (top), IVS-R4 sessions (second), AUSTRAL sessions (third), and all sessions (bottom) for the period from 2012 to the mid of 2016.
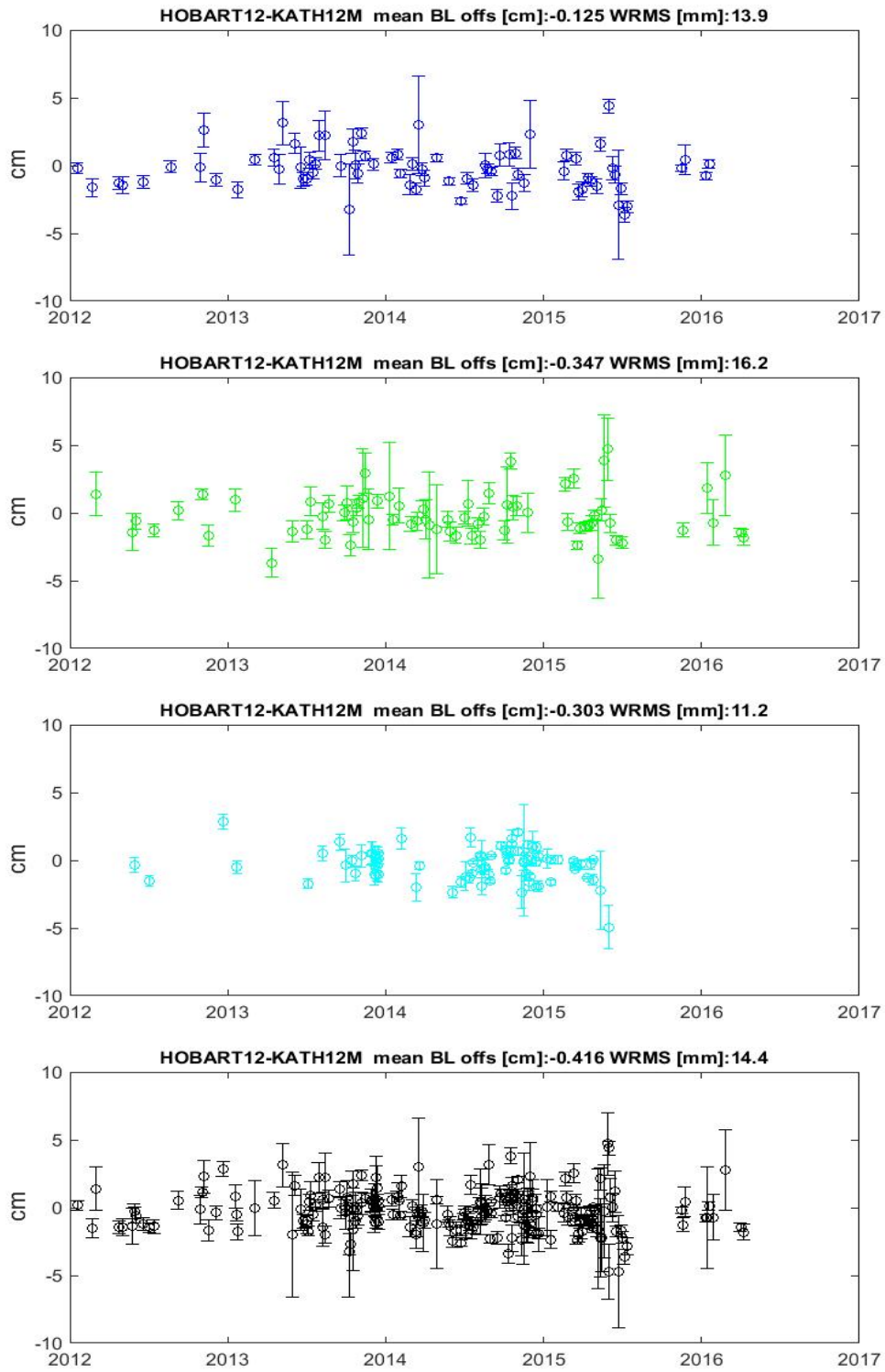
Figure A.1: HOBART12-KATH12M residuals for IVS-R1 (blue), IVS-R4 (green), AUSTRAL (light blue), and IVS-R1/R4+AUSTRAL (black)

Figure A.2: HOBART12-YARRA12M residuals for IVS-R1 (blue), IVS-R4 (green), AUSTRAL (light blue), and IVS-R1/R4+AUSTRAL (black)

Figure A.3: HOBART12-HART15M residuals for IVS-R1 (blue), IVS-R4 (green), AUSTRAL (light blue), and IVS-R1/R4+AUSTRAL (black)

Figure A.4: WARK12M-KATH12M residuals for IVS-R1 (blue), IVS-R4 (green), AUSTRAL (light blue), and IVS-R1/R4+AUSTRAL (black)
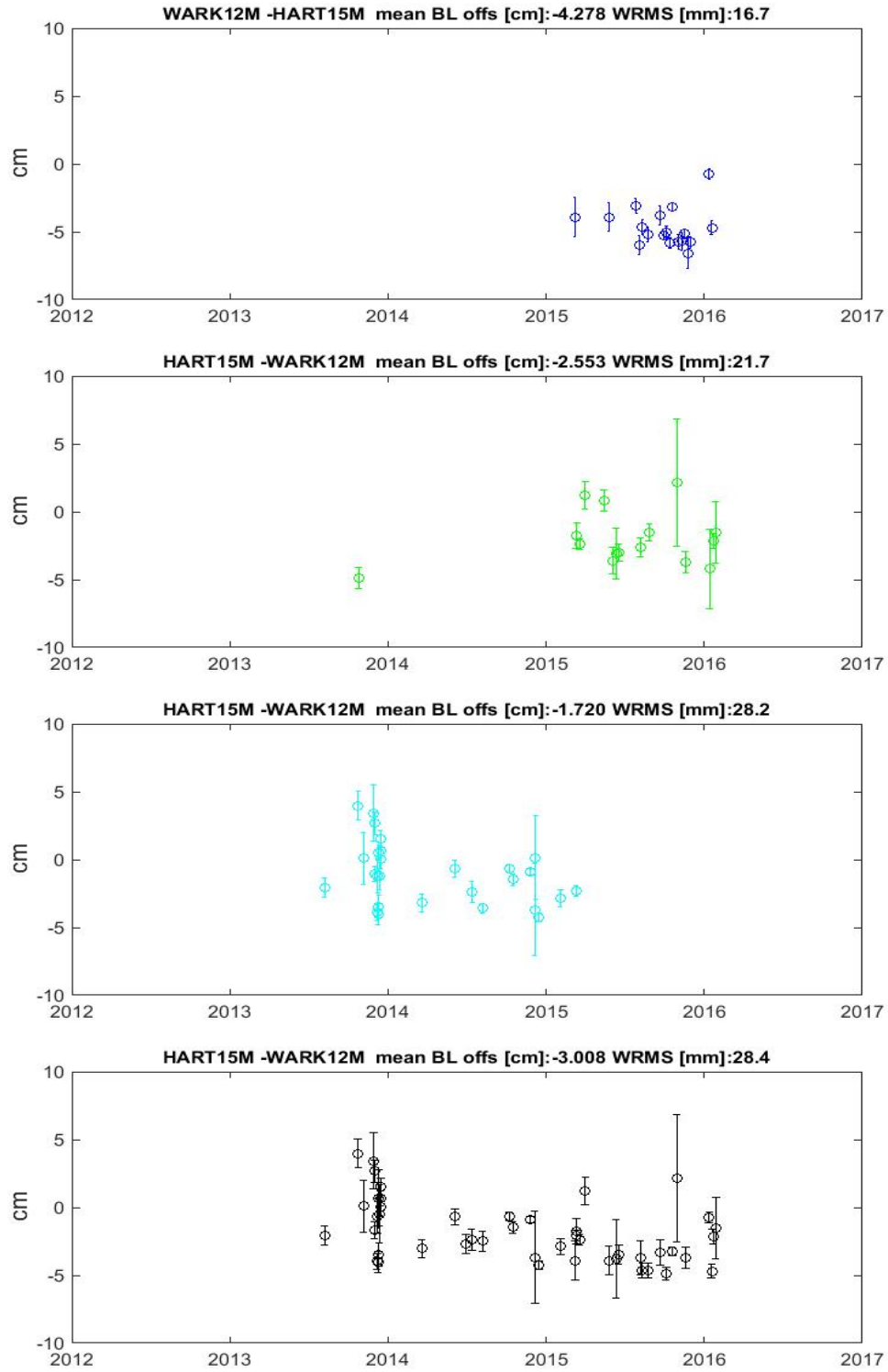
Figure A.5: WARK12M-HART15M residuals for IVS-R1 (blue), IVS-R4 (green), AUSTRAL (light blue), and IVS-R1/R4+AUSTRAL (black)
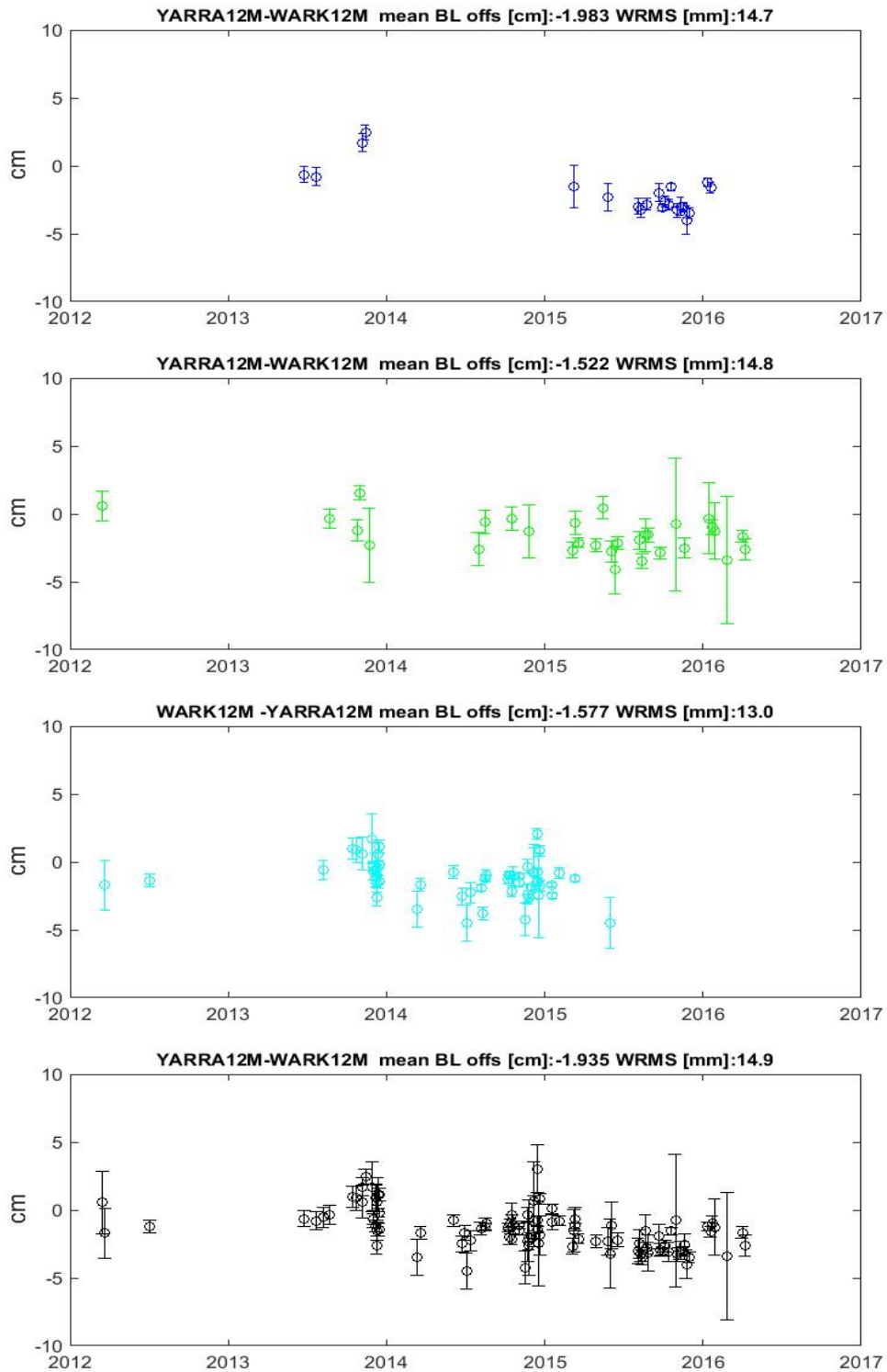
Figure A.6: WARK12M-YARRA12M residuals for IVS-R1 (blue), IVS-R4 (green), AUSTRAL (light blue), and IVS-R1/R4+AUSTRAL (black)
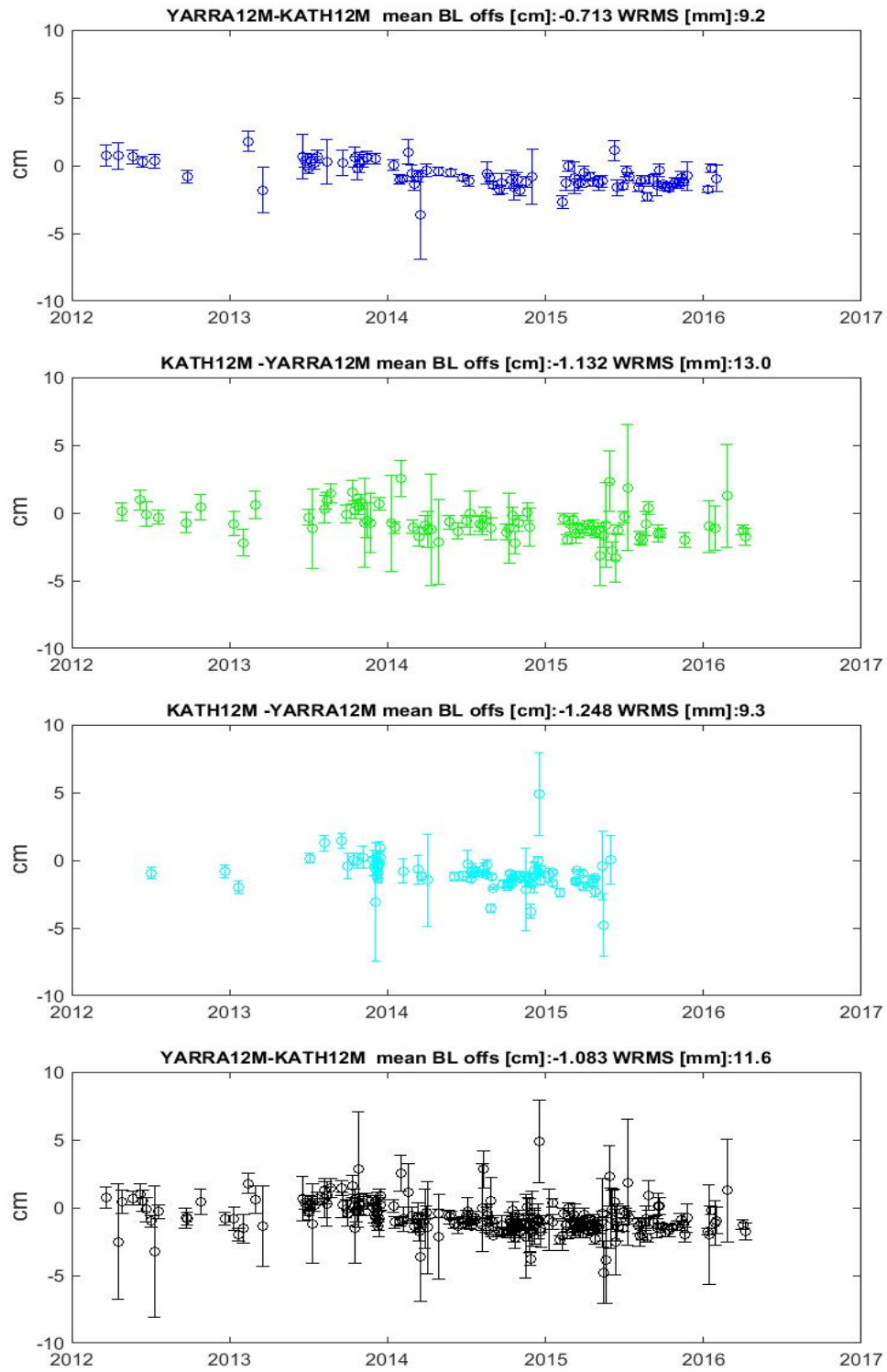
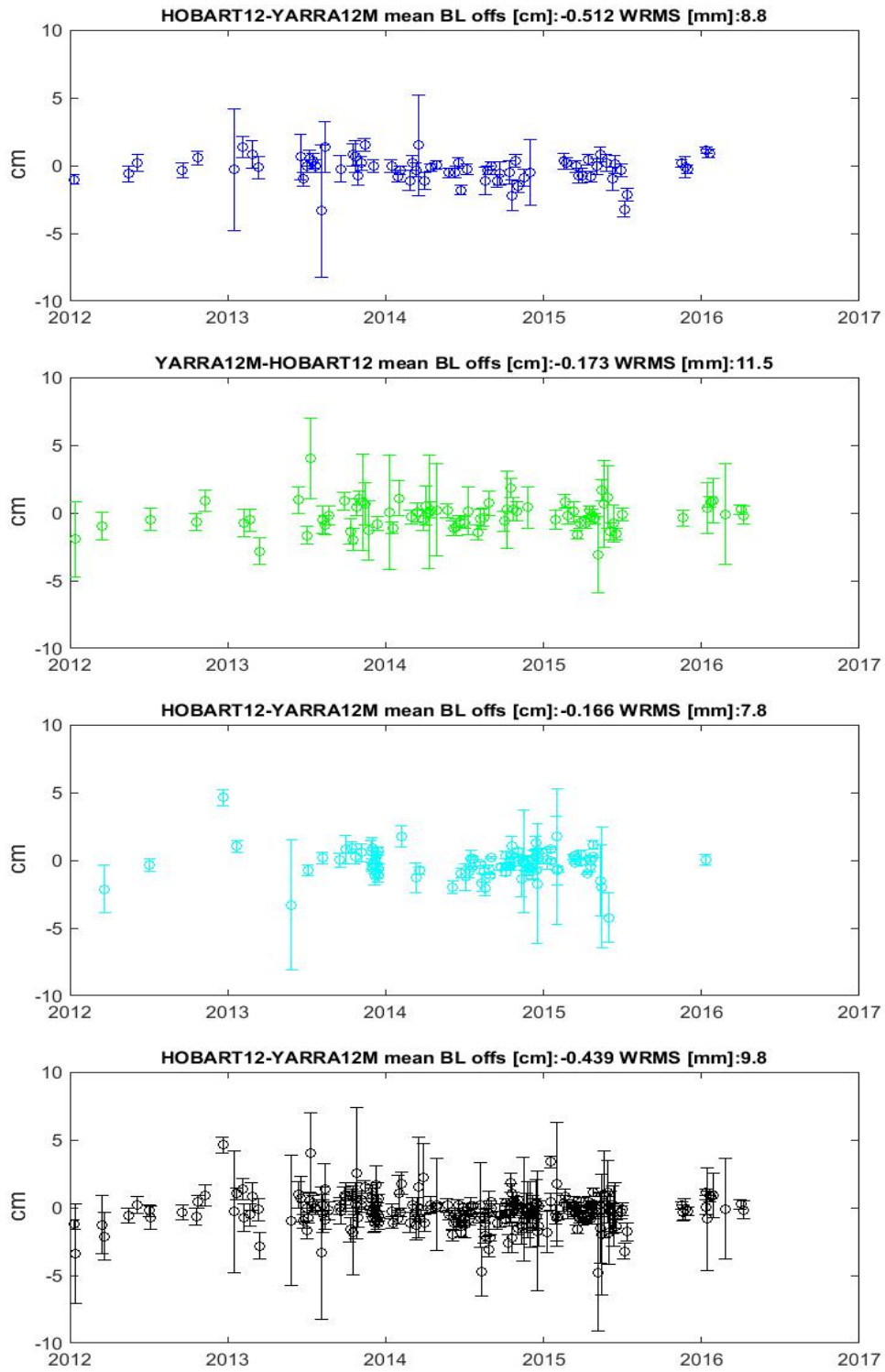Figure A.7: KATH12M-YARRA12M residuals for IVS-R1 (blue), IVS-R4 (green), AUSTRAL (light blue), and IVS-R1/R4+AUSTRAL (black)
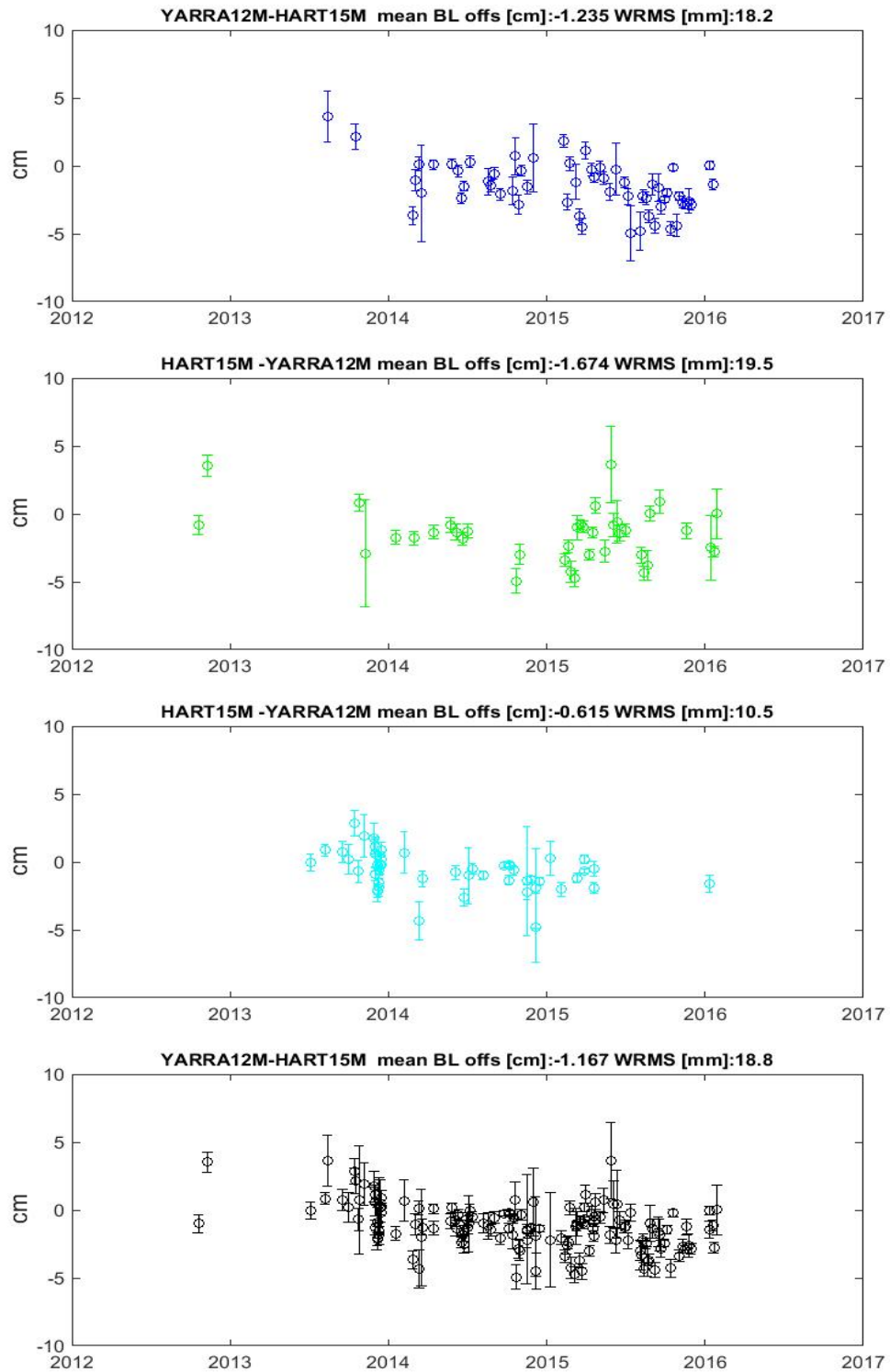
Figure A.8: HART15M-YARRA12M residuals for IVS-R1 (blue), IVS-R4 (green), AUSTRAL (light blue), and IVS-R1/R4+AUSTRAL (black)
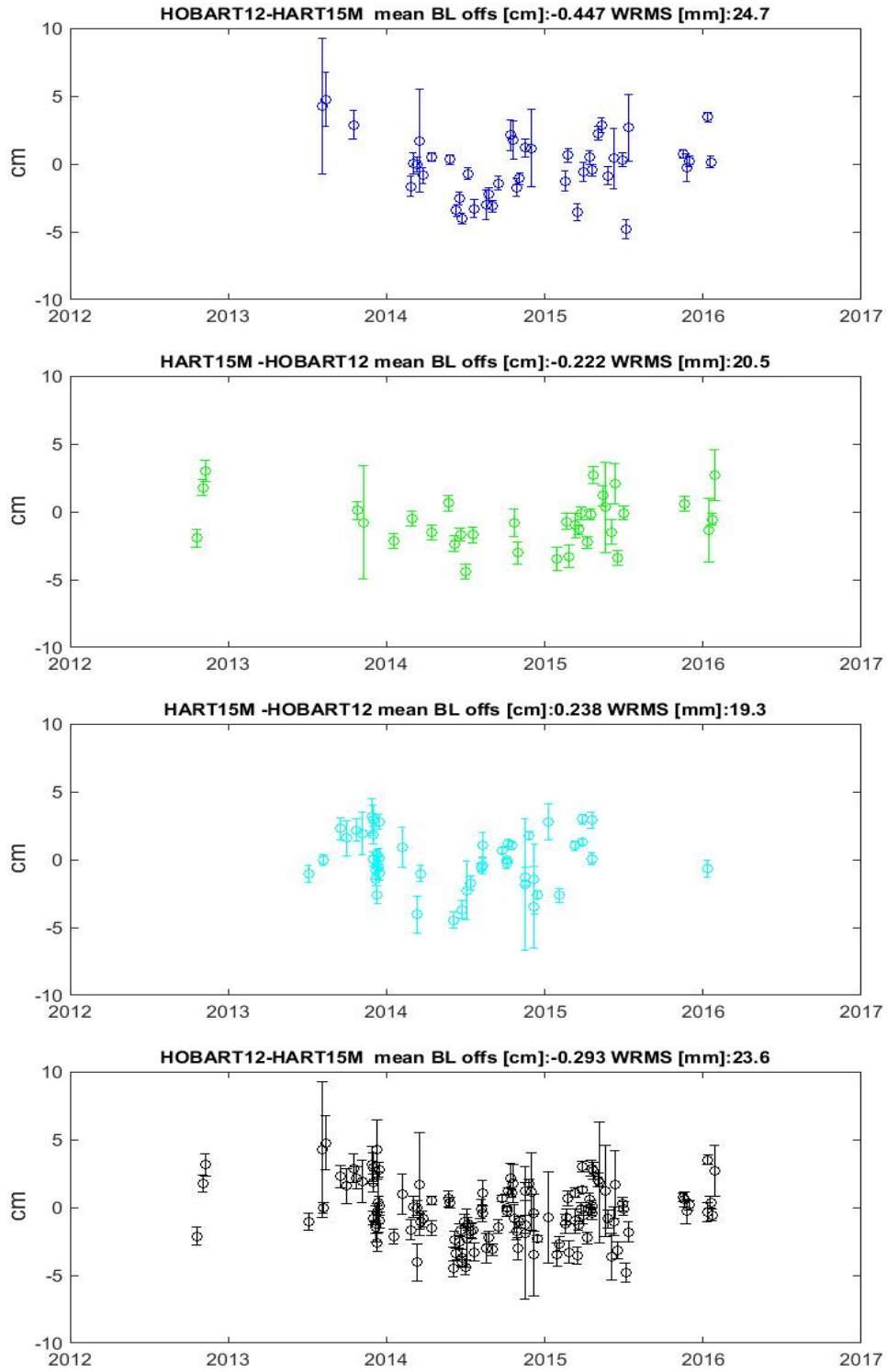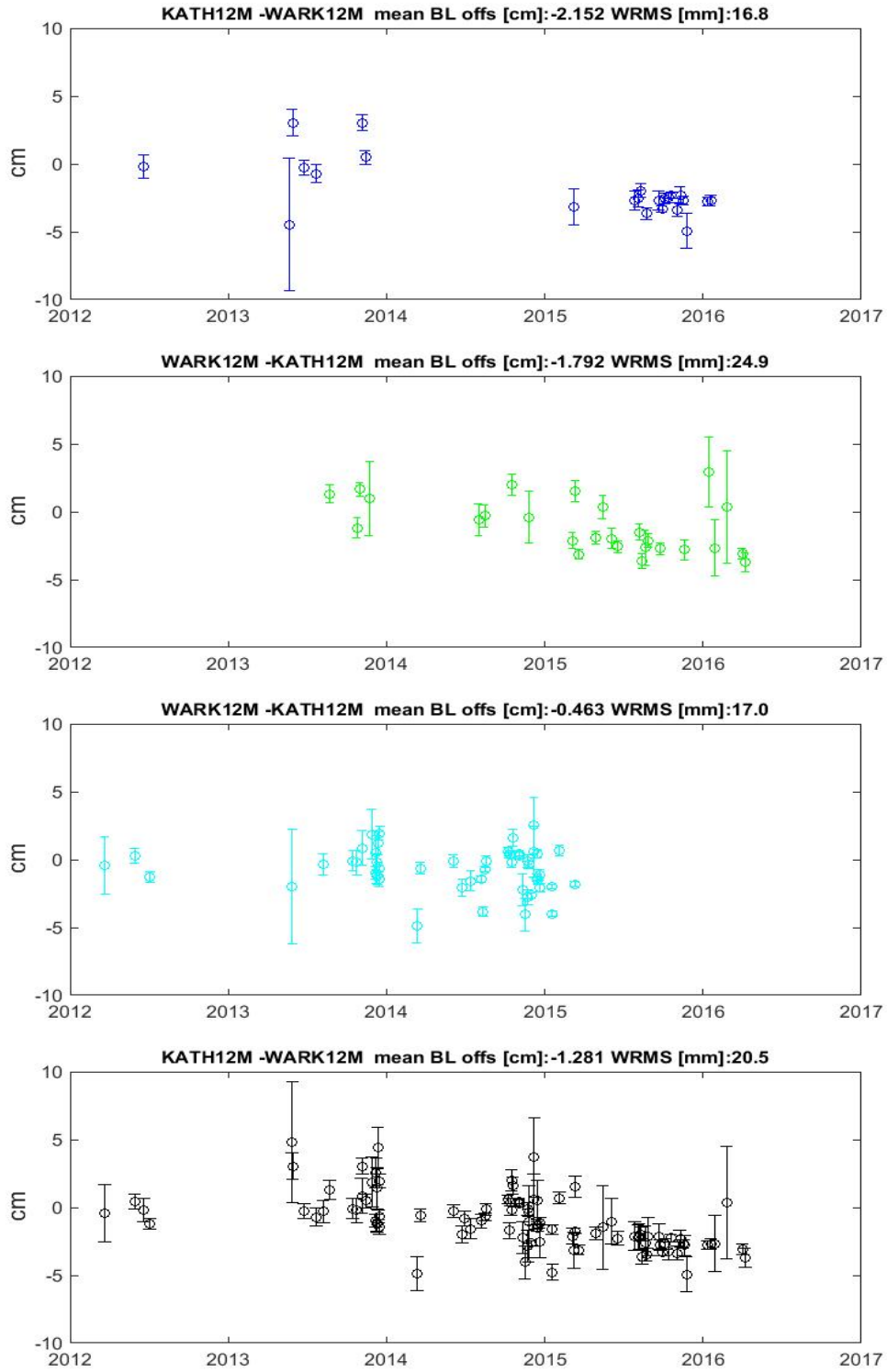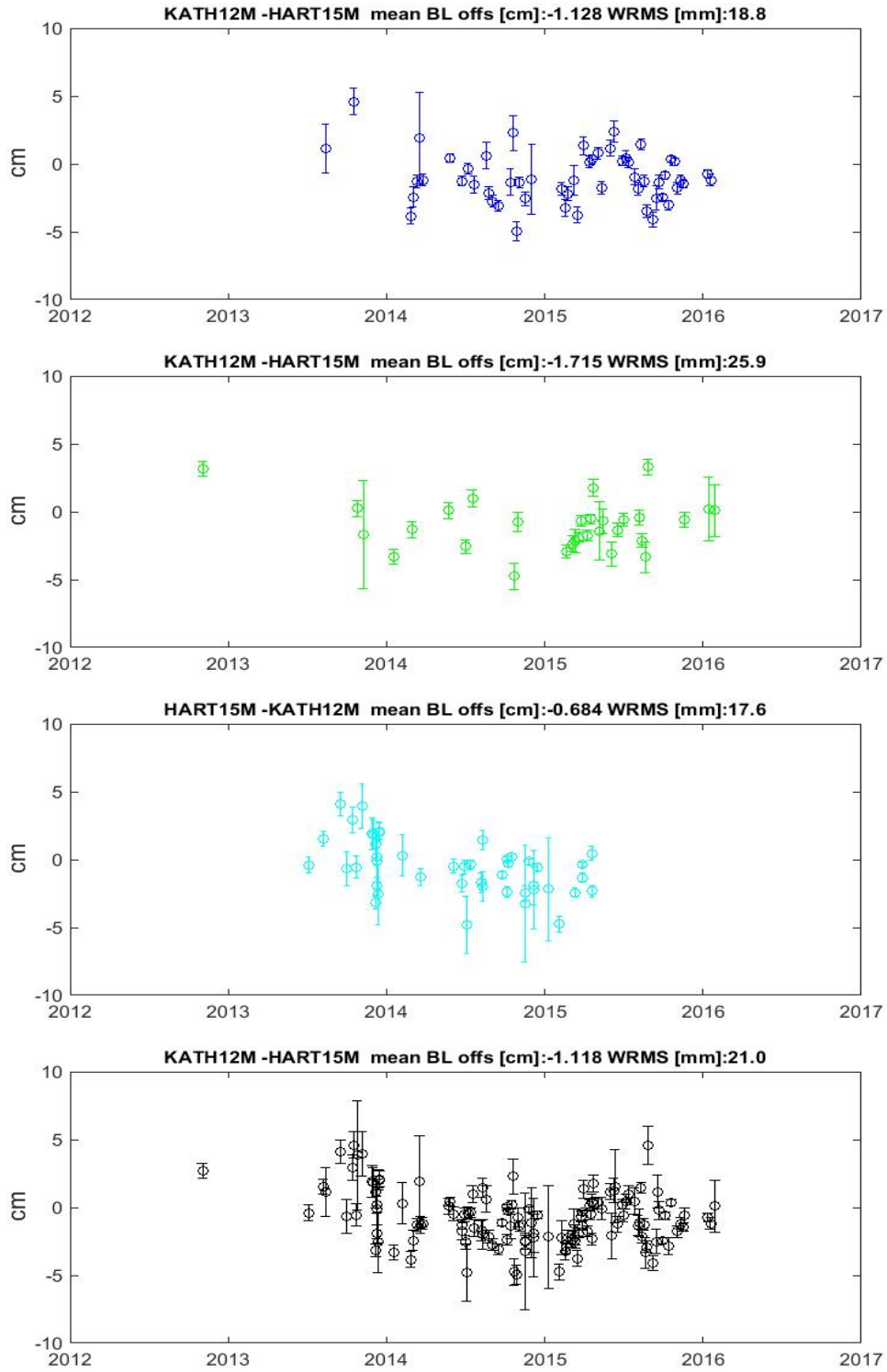
Figure A.9: HART15M-KATH12M residuals for IVS-R1 (blue), IVS-R4 (green), AUSTRAL (light blue), and IVS-R1/R4+AUSTRAL (black)

Appendix B

Matlab: Geocentric coordinate residuals of AUSTRAL stations

```
clear all

% path of files
path= '../';
loadf=1;

% load process_list
kaf=6;

% SUBDIRECTORY
subdir='ALL_IVS_AUSTRAL_2012_2016';
% PROCESSLIST
load PROCESSLIST/ALL_IVS_AUSTRAL_2012_2016.mat

kf=6; % FOR REAL DATA
```

```matlab
clear bas stat

[ns,l] = size(process_list);

mjd(1:ns,1:5) = 0;
coorx(1:ns,1:5) = 0;
coory(1:ns,1:5) = 0;
coorz(1:ns,1:5) = 0;
dcoorx(1:ns,1:5) = 0;
dcoory(1:ns,1:5) = 0;
dcoorz(1:ns,1:5) = 0;


if loadf==1
for ip = 1: ns

fil = process_list(ip,kf:end)
sessnam(ip,:) = fil;
load(['../DATA/LEVEL3/',subdir,'/x_',fil,'.mat']);
load(['../DATA/LEVEL1/',subdir,'/',fil,'_antenna.mat']);
clear stat
nstat = length(x_.antenna);

for k = 1:nstat
    stnam = x_.antenna(k).name;
  if strcmp(stnam,'YARRA12M')||strcmp(stnam,'HOBART12')||strcmp(stnam,'KA
```

```
    if strcmp(stnam,'YARRA12M')
        id = 1;
    end
    if strcmp(stnam,'HOBART12')
        id = 2;
    end
    if strcmp(stnam,'KATH12M ')
        id = 3;
    end
    if strcmp(stnam,'HART15M ')
        id = 4;
    end
    if strcmp(stnam,'WARK12M ')
        id = 5;
    end
mjd(ip,id) = x_.coorx(k).mjd;
coorx(ip,id) = x_.coorx(k).val;
coory(ip,id) = x_.coory(k).val;
coorz(ip,id) = x_.coorz(k).val;
dcoorx(ip,id) = x_.coorx(k).mx;
dcoory(ip,id) = x_.coory(k).mx;
dcoorz(ip,id) = x_.coorz(k).mx;
 end
end
end
end
```

```matlab
% remove zeros
for j = 1:5

    t = mjd(:,j);
    dx = coorx(:,j);
    ddx = dcoorx(:,j);
    t = t(t~=0);
    dx = dx(dx~=0);
    ddx = ddx(ddx~=0);


    t = mjd(:,j);
    dy = coory(:,j);
    ddy = dcoory(:,j);
    t = t(t~=0);
    dy = dy(dy~=0);
    ddy = ddy(ddy~=0);


    t = mjd(:,j);
    dz = coorz(:,j);
    ddz = dcoorz(:,j);
    t = t(t~=0);
    dz = dz(dz~=0);
    ddz = ddz(ddz~=0);


    if j==1
        name = 'YARRA12M';
    end
```

```
if j==2
    name = 'HOBART12';
end
if j==3
    name = 'KATH12M ';
end
if j==4
    name = 'HART15M ';
end
if j==5
    name = 'WARK12M ';
end


dxyz1 = [dx,dy,dz];
ddxyz1 = [ddx,ddy,ddz];
XYZ = [dxyz1,ddxyz1,t];


% coord
XYZ(abs(XYZ(:,1))>5,:)=[];
XYZ(abs(XYZ(:,2))>5,:)=[];
XYZ(abs(XYZ(:,3))>5,:)=[];


% errors
XYZ(abs(XYZ(:,4))>5,:)=[];
XYZ(abs(XYZ(:,5))>5,:)=[];
XYZ(abs(XYZ(:,6))>5,:)=[];
```

```matlab
dx = XYZ(:,1);
dy = XYZ(:,2);
dz = XYZ(:,3);
ddx = XYZ(:,4);
ddy = XYZ(:,5);
ddz = XYZ(:,6);
t = XYZ(:,7);


figure;
subplot(2,2,1);
errorbar(t,dx,ddx,'bo')
set(gca,'xTick',[55927 56293 56658 57023 57388 57754]);
set(gca,'xTicklabel',{'2012','2013','2014','2015','2016','2017'})
set(gca,'xlim',[55927 57754]);
set(gca,'ylim',[-10 10]);
xlabel('Year'), ylabel('x coordinate [cm]')
title(name)

subplot(2,2,2);
errorbar(t,dy,ddy,'go')
set(gca,'xTick',[55927 56293 56658 57023 57388 57754]);
set(gca,'xTicklabel',{'2012','2013','2014','2015','2016','2017'})
set(gca,'xlim',[55927 57754]);
set(gca,'ylim',[-10 10]);
xlabel('Year'), ylabel('y coordinate [cm]')
title(name)
```

```
subplot(2,2,3);
errorbar(t,dz,ddz,'co')
set(gca,'xTick',[55927 56293 56658 57023 57388 57754]);
set(gca,'xTicklabel',{'2012','2013','2014','2015','2016','2017'})
set(gca,'xlim',[55927 57754]);
set(gca,'ylim',[-10 10]);
xlabel('Year'), ylabel('z coordinate [cm]')
title(name)
end
```

Appendix C

Matlab: Local horizontal residuals of AUSTRAL stations

```matlab
clear all

% path of files
path= '../';
loadf=1;

% load process_list
kaf=6;

% SUBDIRECTORY
subdir='ALL_AUSTRAL_2012_2016';

% PROCESSLIST
load PROCESSLIST/ALL_AUSTRAL_2012_2016.mat
```

```
kf=6; % FOR REAL DATA


clear bas stat


[ns,l] = size(process_list);


mjd(1:ns,1:5) = 0;
coorx(1:ns,1:5) = 0;
coory(1:ns,1:5) = 0;
coorz(1:ns,1:5) = 0;
dcoorx(1:ns,1:5) = 0;
dcoory(1:ns,1:5) = 0;
dcoorz(1:ns,1:5) = 0;


Phi = [-0.25092,-0.45186,-0.74706,-0.50697,-0.63591];
Lam = [2.306528,0.483201,2.573322,2.013161,3.048449];


if loadf==1
for ip = 1: ns
fil = process_list(ip,kf:end);
sessnam(ip,:) = fil;
load(['../DATA/LEVEL3/',subdir,'/x_',fil,'.mat']);
load(['../DATA/LEVEL1/',subdir,'/',fil,'_antenna.mat']);
clear stat
nstat = length(x_.antenna);
for k = 1:nstat
    stnam = x_.antenna(k).name;
```

```
if strcmp(stnam, 'KATH12M ')||strcmp(stnam, 'HART15M ')||strcmp(stnam, 'H
    if strcmp(stnam, 'KATH12M ')
        id = 1;
    end
    if strcmp(stnam, 'HART15M ')
        id = 2;
    end
    if strcmp(stnam, 'HOBART12')
        id = 3;
    end
    if strcmp(stnam, 'YARRA12M')
        id = 4;
    end
    if strcmp(stnam, 'WARK12M ')
        id = 5;
    end
mjd(ip, id) = x_.coorx(k).mjd;
coorx(ip, id) = x_.coorx(k).val;
coory(ip, id) = x_.coory(k).val;
coorz(ip, id) = x_.coorz(k).val;
dcoorx(ip, id) = x_.coorx(k).mx;
dcoory(ip, id) = x_.coory(k).mx;
dcoorz(ip, id) = x_.coorz(k).mx;
    end
end
end
end
```

```matlab
% remove zeros
for j = 1:5

t = mjd(:,j);
dx = coorx(:,j);
ddx = dcoorx(:,j);
t = t(t~=0);
dx = dx(dx~=0);
ddx = ddx(ddx~=0);

t = mjd(:,j);
dy = coory(:,j);
ddy = dcoory(:,j);
t = t(t~=0);
dy = dy(dy~=0);
ddy = ddy(ddy~=0);

t = mjd(:,j);
dz = coorz(:,j);
ddz = dcoorz(:,j);
t = t(t~=0);
dz = dz(dz~=0);
ddz = ddz(ddz~=0);

if j==1
    name = 'KATH12M ';
```

```
    phi = Phi(1);
    lam = Lam(1);
end
if j==2
    name = 'HART15M ';
    phi = Phi(2);
    lam = Lam(2);
end
if j==3
    name = 'HOBART12';
    phi = Phi(3);
    lam = Lam(3);
end
if j==4
    name = 'YARRA12M';
    phi = Phi(4);
    lam = Lam(4);
end
if j==5
    name = 'WARK12M ';
    phi = Phi(5);
    lam = Lam(5);
end

dxyz1 = [dx,dy,dz];
ddxyz1 = [ddx,ddy,ddz];
XYZ = [dxyz1,ddxyz1,t];
```

```matlab
% coord
XYZ(abs(XYZ(:,1))>5,:) = [];
XYZ(abs(XYZ(:,2))>5,:) = [];
XYZ(abs(XYZ(:,3))>5,:) = [];

% errors
XYZ(abs(XYZ(:,4))>5,:) = [];
XYZ(abs(XYZ(:,5))>5,:) = [];
XYZ(abs(XYZ(:,6))>5,:) = [];

dx = XYZ(:,1);
dy = XYZ(:,2);
dz = XYZ(:,3);
ddx = XYZ(:,4);
ddy = XYZ(:,5);
ddz = XYZ(:,6);
t = XYZ(:,7);

dxyz = [dx,dy,dz];
ddxyz = [ddx,ddy,ddz];

SS = size(dxyz);
DREN = dxyz;
DDREN = ddxyz;

l1 = size(ddxyz);
```

```matlab
l2 = size(phi);
l3 = size(lam);


l1 = l1(1);
l2 = l2(1);
l3 = l3(1);


eq = isequal(l1,l2,l3);
if eq==0
    fprintf('Number of rows in dxyz, phi and lam must be the same! \n')
end


for i = 1:l1
dE = sqrt(((-sin(lam))*ddx).^2+(cos(lam)*ddy).^2);
dN = sqrt((-cos(lam)*sin(phi)*ddx).^2+(-sin(lam)*sin(phi)*ddy).^2+(cos(p
dU = sqrt((cos(lam)*cos(phi)*ddx).^2+(sin(lam)*cos(phi)*ddy).^2+(sin(phi
ddren(i,:) = [dE(i,:), dN(i,:), dU(i,:)];
end


% xyz2ren
for i = 1:SS(1)
[dren]=xyz2ren(dxyz(i,:),phi,lam);
DREN(i,:)=dren;
DDREN(i,:)=ddren(i,:);
end


figure;
```

```
subplot(2,2,1);
errorbar(t,DREN(:,1),DDREN(:,1),'bo');
set(gca,'xTick',[55927 56293 56658 57023 57388 57754]);
set(gca,'xTicklabel',{'2012','2013','2014','2015','2016','2017'})
set(gca,'xlim',[55927 57754]);
set(gca,'ylim',[-10 10]);
xlabel('Year'), ylabel('U [cm]')
title(name)


subplot(2,2,2);
errorbar(t,DREN(:,2),DDREN(:,2),'go');
set(gca,'xTick',[55927 56293 56658 57023 57388 57754]);
set(gca,'xTicklabel',{'2012','2013','2014','2015','2016','2017'})
set(gca,'xlim',[55927 57754]);
set(gca,'ylim',[-10 10]);
xlabel('Year'), ylabel('E [cm]')
title(name)


subplot(2,2,3);
errorbar(t,DREN(:,3),DDREN(:,3),'co');
set(gca,'xTick',[55927 56293 56658 57023 57388 57754]);
set(gca,'xTicklabel',{'2012','2013','2014','2015','2016','2017'})
set(gca,'xlim',[55927 57754]);
set(gca,'ylim',[-10 10]);
xlabel('Year'), ylabel('N [cm]')
title(name)
end
```

Appendix D

Matlab: Baseline length

```matlab
% programmed for VieVS by:
% Lucia Plank, 7. Sept. 2012

clear all
usesim = 0;
% plotting names of the baseline
plotblnam = 0;
writebas = 1;
% path of files
path = '../';
loadf = 1;
% load process_list
kaf = 6;

% SUBDIRECTORY
subdir = 'AUSTRAL_IVS_2012_2016_S';
```

% PROCESSLIST

```
 load  PROCESSLIST/AUSTRAL_IVS_2012_2016_S.mat


kf = 6; % FOR REAL DATA
clear bas stat
[ns,l] = size(process_list)


if loadf==1
for ip = 1: ns
    fil = process_list(ip,kf:end)
    sessnam(ip,:) = fil;
    load(['../DATA/LEVEL3/',subdir,'/x_',fil,'.mat']);
    load(['../DATA/LEVEL1/',subdir,'/',fil,'_antenna.mat']);


    mjd = x_.coorx(1).mjd;
    clear stat
  % number of stations
    nstat = length(x_.antenna);
    ausc = 0;
    for k = 1:nstat
        stnam = x_.antenna(k).name;
    if strcmp(stnam,'KATH12M ')||strcmp(stnam,'HART15M ')||strcmp(stnam,
        ausc=ausc+1;
    end
  % calculate catalogue coordinates at time of interest


    [xa,ya,za] = corap(antenna,stnam,mjd);
```

```
      stat.apr(k,:) = [xa,ya,za];
      stat.est(k,:) = [x_.coorx(k).val/100,x_.coory(k).val/100,...
                                  x_.coorz(k).val/100]; %[m]
      v = sqrt(x_.coorx(k).val^2+x_.coory(k).val^2+x_.coorz(k).val^2);
%cm
      stat.name(k,1:8) = stnam;
      stat.mx(k,:) = [sqrt((x_.coorx(k).val/v*x_.coorx(k).mx)^2+(x_.coory(

   end


   % calculate corrected values as apriori + estimated corrections
   stat.corr = stat.apr + stat.est;
   isaustr=0;
   % calculate baselines
   % number of baselines
   nbas = nstat*(nstat-1)/2;


   fprintf(' number of baselines in session %4.0f:  %4.0f \n',ip,nbas)


   b = 0;
   if ip==1
   for ib = 1:nstat-1
   for j = ib+1:nstat
      b = b + 1;
      stat1 = stat.name(ib,1:8);
      stat2 = stat.name(j,1:8);
    % length of apriori baseline [m]
```

```
        bas(b).ap = norm(stat.apr(j,:)-stat.apr(ib,:)); % cate+velo
     % length of corrected baseline [m]
        bas(b).corr = norm(stat.corr(j,:)-stat.corr(ib,:));
        bas(b).name = [stat1(1:8),'-',stat2(1:8)];
        bas(b).mjd(ip) = mjd;
        bas(b).isaustr(ip) = isaustr;
        bas(b).mbas = sqrt((stat.mx(j,:).^2+stat.mx(ib,:).^2)./2);
        bas(b).sessnam = fil(1:9);
   end
   end
   else


   for ib = 1:nstat-1
   for j = ib+1:nstat
       stat1 = stat.name(ib,:);
       stat2 = stat.name(j,:);
       basnam1 = [stat1(1:8),'-',stat2(1:8)];
       basnam2 = [stat2(1:8),'-',stat1(1:8)];
       in = 0;
   for f = 1:length(bas)
   if strcmp(bas(f).name,basnam1)||strcmp(bas(f).name,basnam2)
% length of apriori baseline [m]
       bas(f).ap(end+1) = norm(stat.apr(j,:)-stat.apr(ib,:));
% length of corrected baseline [m]
       bas(f).corr(end+1) = norm(stat.corr(j,:)-stat.corr(ib,:));
       bas(f).mjd(end+1) = mjd;
       bas(f).isaustr(end+1) = isaustr;
```

```matlab
            bas ( f ) . mbas (end+1) = sqrt (( stat .mx( j ,:).^2+ stat .mx( ib ,:).^2)./2);
            bas ( f ) . sessnam (end+1,:) = fil (1:9);
            in = 1;
        break
        end
        end
        if in==0; % new baseline
            f = length ( bas )+1; %hana
    % length of apriori baseline [m]
            bas ( f ) . ap (1) = norm( stat . apr ( j ,:)− stat . apr ( ib ,:));
    % length of corrected baseline [m]
            bas ( f ) . corr (1) = norm( stat . corr ( j ,:)− stat . corr ( ib ,:));
            bas ( f ) . name = basnam1 ;
            bas ( f ) . mjd (1) = mjd ;
            bas ( f ) . isaustr (1) = isaustr ;
            bas ( f ) . mbas (1) = sqrt (( stat .mx( j ,:).^2+ stat .mx( ib ,:).^2)./2);
            bas ( f ) . sessnam (1 ,:) = fil (1:9);
        end
        end
        end
        end


        save ([ 'bas_' subdir '.mat'] , 'bas ');
end
else
    load bas_gpsvlbi.mat
end
```

```matlab
% calculate baseline repeatabilities
for i = 1:length(bas)
    bas(i).dbas = bas(i).corr-bas(i).ap;
    bas(i).w = 1./bas(i).mbas;
    bas(i).xq = sum(bas(i).dbas.*bas(i).w)/sum(bas(i).w);
    bas(i).wrms = sqrt(sum((bas(i).dbas-bas(i).xq).^2.*bas(i).w)/sum(bas
    wrms(i) = bas(i).wrms;
    mbas(i) = mean(bas(i).corr);  %[m]
    sbas(i) = std(bas(i).dbas);   %[m]
    basname(i,:) = bas(i).name;
    bas(i).ns = length(bas(i).dbas);
end


for ibas = 1:10
  if ibas==1
     basnam1 = 'HOBART12-WARK12M ';
     basnam2 = 'WARK12M -HOBART12';
     prnam = 'HbWw';
  end
  if ibas==2
     basnam1 = 'HOBART12-KATH12M ';
     basnam2 = 'KATH12M -HOBART12';
     prnam = 'HbKe';
  end
  if ibas==3
     basnam1 = 'KATH12M -YARRA12M';
```

```
      basnam2 = 'YARRA12M–KATH12M ';
      prnam = 'KeYg';
  end
  if ibas==4
      basnam1 = 'WARK12M –YARRA12M';
      basnam2 = 'YARRA12M–WARK12M ';
      prnam = 'WwYg';
  end
  if ibas==5
      basnam1 = 'WARK12M –KATH12M ';
      basnam2 = 'KATH12M –WARK12M ';
      prnam = 'WwKe';
  end
  if ibas==6
      basnam1 = 'HOBART12–YARRA12M';
      basnam2 = 'YARRA12M–HOBART12';
      prnam = 'HbYg';
  end
  if ibas==7
      basnam1 = 'HOBART12–HART15M ';
      basnam2 = 'HART15M –HOBART12';
      prnam = 'HbHt';
  end
  if ibas==8
      basnam1 = 'YARRA12M–HART15M ';
      basnam2 = 'HART15M –YARRA12M';
      prnam = 'YgHt';
```

```matlab
end
if ibas==9
    basnam1 = 'KATH12M -HART15M ';
    basnam2 = 'HART15M -KATH12M ';
    prnam = 'KeHt';
end
if ibas==10
    basnam1 = 'WARK12M -HART15M ';
    basnam2 = 'HART15M -WARK12M ';
    prnam = 'WwHt';
end


for ib = 1:length(bas)
if strcmp(bas(ib).name,basnam1)||strcmp(bas(ib).name,basnam2)
    bb = bas(ib);
    [s,sind] = sort(bas(ib).mjd);
    [raus,ir] = find(abs(bas(ib).dbas)>.15);
    bas(ib).isaustr(ir) = 5;
    [raus,irt] = find(bas(ib).mjd>56597);
    bas(ib).neu(irt) = 1;

    f = figure;
    set(f, 'Units', 'normalized', 'Position', [0.2, 0.1, 0.5, 0.3]);
% min(s)
    t = bas(ib).mjd;
    allind = find(bas(ib).isaustr~=5);
    set(0,'DefaultFigureColor','white')
```

```
set(gca,'FontSize',16)


li = allind;
dbas = bas(ib).dbas(li);
w = 1./bas(ib).mbas(li);
xq = sum(dbas.*w)/sum(w);
erg(ibas).wrms = sqrt(sum((dbas-xq).^2.*w)/sum(w));
erg(ibas).basname = bas(ib).name;


mb = mean(bas(ib).corr(allind)-bas(ib).ap(allind));   % not weighted
wrmsout = erg(ibas).wrms;


aind = allind; saind = allind; sind = allind;

% remove big outliers (residuals)
  V = [(bas(ib).corr(saind)-bas(ib).ap(saind))*100];
  L = [bas(ib).mbas(saind)*100];
  A = [t(saind)];


  v = V';
  l = L';
  a = A';
  VL = [v, l, a];


VL(abs(VL(:,1))>5,:) = [];
VL(abs(VL(:,2))>5,:) = [];
```

```matlab
    v = VL(:,1);
    l = VL(:,2);
    a = VL(:,3);


% remove big outliers (total baselines)
%    Y = [(bas(ib).corr(saind))*100];
%    L = [bas(ib).mbas(saind)*100];
%    S = [(bas(ib).ap(saind))*100];
%    A = [t(saind)];
%
%    y = Y';
%    l = L';
%    s = S';
%    a = A';
%    VL1 = [y, l, s, a];
%    VL1(abs(VL1(:,2))>10,:) = [];
%
%    y = VL1(:,1);
%    l = VL1(:,2);
%    s = VL1(:,3);
%    a = VL1(:,4);


% residuals
    errorbar(a, v, l,'ko','LineWidth',1), hold on

% total basline
%    errorbar(a,y,l,'go','LineWidth',1), hold on;
```

```matlab
%    plot(a,s,'b-','LineWidth',1), hold on

     title(strcat([bas(ib).name,' mean BL offs [cm]:' num2str(mb*100,'%1
     set(gca,'xTick',[55927 56293 56658 57023 57388 57754]);
     set(gca,'xTicklabel',{'2012','2013','2014','2015','2016','2017'})

     set(gca,'xlim',[55927 57754]);
     set(gca,'ylim',[-10 10]); %coordinate all

     ylabel('cm','Fontsize',16)
     set(0,'DefaultFigureColor','white')
     set(gca,'FontSize',12)
     set(gcf,'PaperPositionMode','auto');
     set(gca,'YTickLabel',num2str(get(gca,'YTick').'))

  if writebas==1

 for ibo = 1:length(sind)
     lo = [bas(ib).mjd(ibo),bas(ib).ap(ibo),bas(ib).corr(ibo),bas(ib).mb
     fprintf(1,'%s %s %15.4f %15.4f %15.4f %15.4f %7.4f\n',prnam,bas(ib)

     clear lo
 end
 end
 end
end
end
```

Appendix E

Matlab: Weighted slopes and a $priori$ slopes

```
function Results = weightedfit(data)

data = xlsread('H:\WARK_HOBART_BAS_TEST.xlsx');
x = data(:,3);
x = x-2011;
ap = data(:,4);
y = data(:,5);
stdv = data(:,6);

w = 1./stdv.^2;
S = sum(w);
Sx = sum(w.*x);
Sy = sum(w.*y);
Sxx= sum(w.*x.^2);
Sxy= sum(w.*x.*y);
```

```matlab
Delta = S*Sxx - (Sx)^2;
a = (Sxx*Sy - Sx*Sxy)./Delta;
b = (S*Sxy - Sx*Sy)./Delta;
slope_ap = (ap(4)-ap(1))/(x(4)-x(1));
fprintf('\n slope=%f Int=%f \n',b,slope_ap)
Results.slope = b;
Results.Intercept = a;
Results.Apriori = slope_ap;
y_fit = a + b*x;


% slope errors
x = x';
y = y';
w = w';
modelFun = @(b,x) b(1)+b(2).*x;
start = [9504494; 0];
wnlm = fitnlm(x,y,modelFun,start,'Weight',w);


% plot
figure
clf;set(gcf,'color','w');
whitebg([1 1 1]);
h = errorbar(x+2011,y,stdv,'bo');
title(strcat(['HOBART12-WARK12M']),'Fontsize',12);
hold on;
q = plot(x+2011,y_fit,'g-',x+2011,ap,'m:');
set(gca,'xlim',[2012 2017]);
```

```matlab
xlabel('Year');
ylabel('Baseline, m');
legend([h(1),q(1),q(2)],'Data',sprintf('Weighted slope =%2.1f mm/yr', b*
A priori slope=%2.1f mm/yr \n', slope_ap*1000),'location','Northwest');
set(gca,'FontSize',12);
set(gcf,'PaperPositionMode','auto');
set(gca,'YTickLabel',num2str(get(gca,'YTick').'));


end
```

Appendix F

Matlab: VLBI tropospheric zenith wet delay

```
clear all
% path of files
path = '../';
loadf = 1;
% load process_list
kaf = 6;


% SUBDIRECTORY
  subdir='ALL_AUSTRAL_2012_2016';


% PROCESSLIST
  load PROCESSLIST/ALL_AUSTRAL_2012_2016.mat
  kf = 6; % FOR REAL DATA


clear bas stat
```

```matlab
[ns,l] = size(process_list);


mjd(1:ns,1:5) = 0;
zwd(1:ns,1:5) = 0;
dzwd(1:ns,1:5) = 0;


if loadf==1
 for ip = 1: ns


 fil = process_list(ip,kf:end);
 sessnam(ip,:) = fil;
 % load(['../DATA/LEVEL3/',subdir,'/x_',fil,'.mat']);
 load(['../DATA/LEVEL3/',subdir,'/res_',fil,'.mat']);
 % load(['../DATA/LEVEL1/',subdir,'/',fil,'_antenna.mat']);
 clear stat
 nstat = length(x_.antenna);


 sres = std(res_.mainVal);
 for k = 1:nstat
     stnam = x_.antenna(k).name;
     if strcmp(stnam,'KATH12M ')||strcmp(stnam,'HART15M ')||strcmp(stnam
         if strcmp(stnam,'KATH12M ')
             id = 1;
             mjd = x_.zwd(k).mjd;
             Mjd_KATH(ip) = mjd(1);
             weight = 1./(x_.zwd(k).mx).^2;  % weighted
```

```matlab
      zwd = sum(x_.zwd(k).val.*weight)/sum(weight);
      Zwd_KATH(ip) = zwd;
      dzwd = sqrt(sum((x_.zwd(k).val-zwd).^2.*weight)/sum(weight));
      Dzwd_KATH(ip) = dzwd;
  end
  if strcmp(stnam,'HART15M ')
      id = 2;
      mjd = x_.zwd(k).mjd;
      Mjd_HART(ip) = mjd(1);
      weight = 1./(x_.zwd(k).mx).^2;   % weighted
      zwd = sum(x_.zwd(k).val.*weight)/sum(weight);
      Zwd_HART(ip) = zwd;
      dzwd = sqrt(sum((x_.zwd(k).val-zwd).^2.*weight)/sum(weight));
      Dzwd_HART(ip) = dzwd;
  end
  if strcmp(stnam,'HOBART12')
      id = 3;
      mjd = x_.zwd(k).mjd;
      Mjd_HOBART(ip) = mjd(1);
      weight = 1./(x_.zwd(k).mx).^2;   % weighted
      zwd = sum(x_.zwd(k).val.*weight)/sum(weight);
      Zwd_HOBART(ip) = zwd;
      dzwd = sqrt(sum((x_.zwd(k).val-zwd).^2.*weight)/sum(weight));
      Dzwd_HOBART(ip) = dzwd;
  end
  if strcmp(stnam,'YARRA12M')
      id = 4;
```

```
                    mjd = x_.zwd(k).mjd;
                    Mjd_YARRA(ip) = mjd(1);
                    weight = 1./(x_.zwd(k).mx).^2;   % weighted
                    zwd = sum(x_.zwd(k).val.*weight)/sum(weight);
                    Zwd_YARRA(ip) = zwd;
                    dzwd = sqrt(sum((x_.zwd(k).val-zwd).^2.*weight)/sum(weight));
                    Dzwd_YARRA(ip) = dzwd;
                end
                if strcmp(stnam, 'WARK12M ')
                    id = 5;
                    mjd = x_.zwd(k).mjd;
                    Mjd_WARK(ip) = mjd(1);
                    weight = 1./(x_.zwd(k).mx).^2;   % weighted
                    zwd = sum(x_.zwd(k).val.*weight)/sum(weight);
                    Zwd_WARK(ip) = zwd;
                    dzwd = sqrt(sum((x_.zwd(k).val-zwd).^2.*weight)/sum(weight));
                    Dzwd_WARK(ip) = dzwd;
                end
            end
        end
    end
end


Mjd_KATH( :, ~any(Mjd_KATH,1) ) = [];
Zwd_KATH( :, ~any(Zwd_KATH,1) ) = [];
Dzwd_KATH( :, ~any(Dzwd_KATH,1) ) = [];
```

```
MJD_KATH = Mjd_KATH';
ZWD_KATH = Zwd_KATH';
DZWD_KATH = Dzwd_KATH';


xyz = [ZWD_KATH];
xyz1 = [DZWD_KATH];
XYZ = [ZWD_KATH, DZWD_KATH, MJD_KATH];


XYZ(abs(XYZ(:,2)) > 20,:) = [];


Zwd_KATH = XYZ(:,1);
Dzwd_KATH = XYZ(:,2);
Mjd_KATH = XYZ(:,3);


Mjd_HART( :, ~any(Mjd_HART,1) ) = [];
Zwd_HART( :, ~any(Zwd_HART,1) ) = [];
Dzwd_HART( :, ~any(Dzwd_HART,1) ) = [];


MJD_HART = Mjd_HART';
ZWD_HART = Zwd_HART';
DZWD_HART = Dzwd_HART';


xyz = [ZWD_HART];
xyz1 = [DZWD_HART];
XYZ = [ZWD_HART, DZWD_HART, MJD_HART];


XYZ(abs(XYZ(:,2)) > 20,:) = [];
```

```
Zwd_HART = XYZ( : , 1 );
Dzwd_HART = XYZ( : , 2 );
Mjd_HART = XYZ( : , 3 );


Mjd_HOBART( : , ~any(Mjd_HOBART,1) ) = [ ];
Zwd_HOBART( : , ~any(Zwd_HOBART,1) ) = [ ];
Dzwd_HOBART( : , ~any(Dzwd_HOBART,1) ) = [ ];


MJD_HOBART = Mjd_HOBART';
ZWD_HOBART = Zwd_HOBART';
DZWD_HOBART = Dzwd_HOBART';


xyz = [ZWD_HOBART];
xyz1 = [DZWD_HOBART];
XYZ = [ZWD_HOBART, DZWD_HOBART, MJD_HOBART];


XYZ( abs(XYZ( : ,2)) > 20 ,:) = [ ];


Zwd_HOBART = XYZ( : , 1 );
Dzwd_HOBART = XYZ( : , 2 );
Mjd_HOBART = XYZ( : , 3 );


Mjd_YARRA( : , ~any(Mjd_YARRA,1) ) = [ ];
Zwd_YARRA( : , ~any(Zwd_YARRA,1) ) = [ ];
Dzwd_YARRA( : , ~any(Dzwd_YARRA,1) ) = [ ];
```

```
MJD_YARRA = Mjd_YARRA';
ZWD_YARRA = Zwd_YARRA';
DZWD_YARRA = Dzwd_YARRA';


xyz = [ZWD_YARRA];
xyz1 = [DZWD_YARRA];
XYZ = [ZWD_YARRA, DZWD_YARRA, MJD_YARRA];


XYZ(abs(XYZ(:,2))>20,:)=[];


Zwd_YARRA = XYZ(:,1);
Dzwd_YARRA = XYZ(:,2);
Mjd_YARRA = XYZ(:,3);


Mjd_WARK( :, ~any(Mjd_WARK,1) ) = [];
Zwd_WARK( :, ~any(Zwd_WARK,1) ) = [];
Dzwd_WARK( :, ~any(Dzwd_WARK,1) ) = [];


MJD_WARK = Mjd_WARK';
ZWD_WARK = Zwd_WARK';
DZWD_WARK = Dzwd_WARK';


xyz = [ZWD_WARK];
xyz1 = [DZWD_WARK];
XYZ = [ZWD_WARK, DZWD_WARK, MJD_WARK];


XYZ(abs(XYZ(:,2))>20,:)=[];
```

```matlab
Zwd_WARK = XYZ(:,1);
Dzwd_WARK = XYZ(:,2);
Mjd_WARK = XYZ(:,3);


figure
errorbar(Mjd_KATH,Zwd_KATH,Dzwd_KATH,'bo');
set(gca,'xTick',[55927 56293 56658 57023 57388 57754]);
set(gca,'xTicklabel',{'2012','2013','2014','2015','2016','2017'});
set(gca,'xlim',[55927 57754]);
set(gca,'ylim',[0 40]);
xlabel('Year'), ylabel('zwd [cm]');
title('KATH12M ');


figure
errorbar(Mjd_HART,Zwd_HART,Dzwd_HART,'bo');
set(gca,'xTick',[55927 56293 56658 57023 57388 57754]);
set(gca,'xTicklabel',{'2012','2013','2014','2015','2016','2017'});
set(gca,'xlim',[55927 57754]);
set(gca,'ylim',[0 40]);
xlabel('Year'), ylabel('zwd [cm]');
title('HART15M ');


figure
errorbar(Mjd_HOBART,Zwd_HOBART,Dzwd_HOBART,'bo');
set(gca,'xTick',[55927 56293 56658 57023 57388 57754]);
set(gca,'xTicklabel',{'2012','2013','2014','2015','2016','2017'});
```

```matlab
set(gca,'xlim',[55927 57754]);
set(gca,'ylim',[0 40]);
xlabel('Year'), ylabel('zwd [cm]');
title('HOBART12');


figure
errorbar(Mjd_YARRA,Zwd_YARRA,Dzwd_YARRA,'bo');
set(gca,'xTick',[55927 56293 56658 57023 57388 57754]);
set(gca,'xTicklabel',{'2012','2013','2014','2015','2016','2017'});
set(gca,'xlim',[55927 57754]);
set(gca,'ylim',[0 40]);
xlabel('Year'), ylabel('zwd [cm]');
title('YARRA12M');


figure
errorbar(Mjd_WARK,Zwd_WARK,Dzwd_WARK,'bo');
set(gca,'xTick',[55927 56293 56658 57023 57388 57754]);
set(gca,'xTicklabel',{'2012','2013','2014','2015','2016','2017'});
set(gca,'xlim',[55927 57754]);
set(gca,'ylim',[0 40]);
xlabel('Year'), ylabel('zwd [cm]');
title('WARK12M ');
```

Appendix G

Matlab: Comparison of VLBI and GNSS tropospheric zenith wet delay

```
data = xlsread('H:\15JAN18_30MINS');

t1_vlbi = datetime(2015,1,18,0,0,0);
t2_vlbi = datetime(2015,1,19,0,0,0);
t_vlbi = t1_vlbi:minutes(30):t2_vlbi;

x_vlbi_time = t_vlbi;
x_vlbi_time = char(x_vlbi_time);
x_vlbi_t = datenum(x_vlbi_time,'dd-mmm-yyyy HH:MM:SS');

zwd_vlbi = data(:,3);
err_vlbi = data(:,4);
zwd_vlbi(isnan(zwd_vlbi)) = [];
```

```matlab
err_vlbi(isnan(err_vlbi)) = [];


t1_gps = datetime(2015,1,18,0,0,0);
t2_gps = datetime(2015,1,18,0,0,0);
t3_gps = datetime(2015,1,18,1,0,0);
t4_gps = datetime(2015,1,18,23,0,0);
t5_gps = datetime(2015,1,19,0,0,0);
t6_gps = datetime(2015,1,19,0,0,0);
t_gps_1 = t1_gps:hours:t2_gps;
t_gps_2 = t2_gps:hours:t5_gps;
t_gps_3 = t5_gps:hours:t6_gps;
t_gps = [t_gps_1 t_gps_2 t_gps_3];


% t1_gps = datetime(2015,1,17,0,0,0);
% t2_gps = datetime(2015,1,18,0,0,0);
% t3_gps = datetime(2015,1,18,0,0,0);
% t_gps_1 = t1_gps:hours:t2_gps;
% t_gps_2 = t2_gps:hours:t3_gps;
% t_gps = [t_gps_1 t_gps_2];
x_gps_time = t_gps;
x_gps_time = char(t_gps);
x_gps_t=datenum(x_gps_time,'dd-mmm-yyyy HH:MM:SS');
zwd_gps = data(:,13);
err_gps = data(:,15);
zwd_gps(isnan(zwd_gps)) = [];
err_gps(isnan(err_gps)) = [];
```

```
figure;
errorbar(x_vlbi_t, zwd_vlbi, err_vlbi,'bo');
datetick('x','dd-mmm-yyyy HH:MM:SS','keepticks','keeplimits');
hold on
errorbar(x_gps_t,zwd_gps,err_gps,'g*')
ax = gca;
ax.XTickLabelRotation = 40;
set(gca,'ylim',[0 25]); %coordinate all
xlabel('Time[Hour]'), ylabel('zwd [cm]');
legend('AUSTRAL-VLBI','GPS','Location','Southwest');
title('WARK12M at TimeInterval:30 Mins');
```

Appendix H

Matlab: Earth orientation parameters

```
clear all
% path of files
path= '../';


loadf=1;


% load process_list
kaf=24;


% SUBDIRECTORY
  subdir='SD_sched'; % subdirectory


% PROCESSLIST
  load PROCESSLIST/su_sim.mat
```

```matlab
kf=24; % FOR REAL DATA


clear bas stat


[ns,l]=size(process_list);


mjd(1:ns)=0;
xpol(1:ns)=0;
ypol(1:ns)=0;
dut1(1:ns)=0;
ddut1(1:ns)=0;
nutdx(1:ns)=0;
nutdy(1:ns)=0;
dnutdx(1:ns)=0;
dnutdy(1:ns)=0;


if loadf==1
  for ip=1: ns


    fil=process_list(ip,35:end);
    sessnam(ip,:)=fil;
    load(['../DATA/LEVEL3/',subdir,'/x_',fil,'.mat']);
    load(['../DATA/LEVEL1/',subdir,'/',fil,'_antenna.mat']);
%       fil='16MAY28VA_S100';
%       sessnam(ip,:)=fil;
%       load(['../DATA/LEVEL3/',subdir,'/x_',fil,'.mat']);
%
```

```
%      load ([ '../DATA/LEVEL1/', subdir, '/', fil, '_antenna.mat']);
    clear stat
    nstat = length(x_.antenna);


    for k = 1:nstat
        stnam = x_.antenna(k).name;
        if strcmp(stnam, 'KATH12M ')||strcmp(stnam, 'HART15M ')||strcmp(str
         if strcmp(stnam, 'KATH12M ')
             id=1;
         end
         if strcmp(stnam, 'HART15M ')
             id=2;
         end
         if strcmp(stnam, 'HOBART12')
             id=3;
         end
         if strcmp(stnam, 'YARRA12M')
             id=4;
         end
         if strcmp(stnam, 'WARK12M ')
             id=5;
         end


        mjd = x_.dut1.mjd;
         Mjd(ip) = mjd(2); % we use the second of three consequtive day


         xpol = x_.xpol.val;
```

```
Xpol(ip)=xpol(2); % same here


ypol = x_.ypol.val;
Ypol(ip)=ypol(2);


dxpol = x_.xpol.mx;
DXpol(ip)=dxpol(2);


dypol = x_.ypol.mx;
DYpol(ip)=dypol(2);


dut1 = x_.dut1.val;
 Dut1(ip)=dut1(2);


ddut1 = x_.dut1.mx;
 DDUT1(ip) = ddut1(2);


nutdx = x_.nutdx.val;
Nutdx(ip) = nutdx(2);


nutdy = x_.nutdy.val;
Nutdy(ip) = nutdy(2);


dnutdx = x_.nutdx.mx;
DNutdx(ip) = dnutdx(2);


dnutdy = x_.nutdy.mx;
```

```
        DNutdy(ip) = dnutdy(2);


            end

        end

end

end


        % remove zero rows (R1 SESSION)
        Mjd( :, ~any(Mjd,1) ) = [];
        DNutdx( :, ~any(DNutdx,1) ) = [];
        DNutdy( :, ~any(DNutdy,1) ) = [];
        Dut1( :, ~any(Dut1,1) ) = [];
        DDUT1( :, ~any(DDUT1,1) ) = [];
        DXpol( :, ~any(DXpol,1) ) = [];
        DYpol( :, ~any(DYpol,1) ) = [];
        Xpol( :, ~any(Xpol,1) ) = [];
        Ypol( :, ~any(Ypol,1) ) = [];
        Nutdx( :, ~any(Nutdx,1) ) = [];
        Nutdy( :, ~any(Nutdy,1) ) = [];


        XPOL = Xpol';
        YPOL = Ypol';
        DUT1 = Dut1';
        NUTDX = Nutdx';
        NUTDY = Nutdy';
        DXPOL = DXpol';
        DYPOL = DYpol';
```

```
ddut1 = DDUT1';
DNUTDX = DNutdx';
DNUTDY = DNutdy';
t = Mjd';
xyz = [XPOL, YPOL, DUT1, NUTDX, NUTDY];
xyz1 = [DXPOL, DYPOL, ddut1, DNUTDX, DNUTDY];
XYZ = [xyz, xyz1, t];
% remove big outliers (R1 session and AUSTRAL session)
XYZ(abs(XYZ(:,1))>5,:)=[];
XYZ(abs(XYZ(:,2))>5,:)=[];
XYZ(abs(XYZ(:,3))>5,:)=[];
XYZ(abs(XYZ(:,4))>5,:)=[];
XYZ(abs(XYZ(:,5))>5,:)=[];
XYZ(abs(XYZ(:,6))>5,:)=[];
XYZ(abs(XYZ(:,7))>5,:)=[];
XYZ(abs(XYZ(:,8))>2,:)=[];
XYZ(abs(XYZ(:,9))>2,:)=[];
XYZ(abs(XYZ(:,10))>2,:)=[];

Xpol = XYZ(:,1);
Ypol = XYZ(:,2);
Dut1 = XYZ(:,3);
Nutdx = XYZ(:,4);
Nutdy = XYZ(:,5);
DXpol = XYZ(:,6);
DYpol = XYZ(:,7);
DDUT1 = XYZ(:,8);
```

```
DNutdx = XYZ(: ,9);
DNutdy = XYZ(: ,10);
Mjd = XYZ(: ,11);
% remove big outliers (AUSTRAL SESSIONS)
Xpol(abs(Xpol(1,:))>5)=[];
Ypol(abs(Ypol(1,:))>5)=[];
Dut1(abs(Dut1(1,:))>1)=[];
Nutdx(abs(Nutdx(1,:))>2)=[];
Nutdy(abs(Nutdy(1,:))>2)=[];
DXpol(abs(DXpol(1,:))>5)=[];
DYpol(abs(DYpol(1,:))>5)=[];
DDUT1(abs(DDUT1(1,:))>1)=[];
DNutdx(abs(DNutdx(1,:))>2)=[];
DNutdy(abs(DNutdy(1,:))>2)=[];


figure
errorbar(Mjd,Xpol,DXpol,'bo')
set(gca,'xTick',[55927 56293 56658 57023 57388 57754]);
set(gca,'xTicklabel',{'2012','2013','2014','2015','2016','2017'})
set(gca,'xlim',[55927 57754]);
set(gca,'ylim',[-2 2]); % coordinate all
xlabel('Year'), ylabel('xpol [mas]')
title('IVS-R4 EOP: xpol')


figure
errorbar(Mjd,Ypol,DYpol,'bo')
set(gca,'xTick',[55927 56293 56658 57023 57388 57754]);
```

```
set(gca,'xTicklabel',{'2012','2013','2014','2015','2016','2017'})
set(gca,'xlim',[55927 57754]);
set(gca,'ylim',[-2 2]); % coordinate all
xlabel('Year'), ylabel('ypol [mas]')
title('IVS-R4 EOP: ypol')


figure
errorbar(Mjd,Dut1,DDUT1,'bo')
set(gca,'xTick',[55927 56293 56658 57023 57388 57754]);
set(gca,'xTicklabel',{'2012','2013','2014','2015','2016','2017'})
set(gca,'xlim',[55927 57754]);
set(gca,'ylim',[-0.2 0.2]); % coordinate all
xlabel('Year'), ylabel('dut1 [ms]')
title('IVS-R4 EOP: dut1')


figure
errorbar(Mjd,Nutdx,DNutdx,'bo')
set(gca,'xTick',[55927 56293 56658 57023 57388 57754]);
set(gca,'xTicklabel',{'2012','2013','2014','2015','2016','2017'})
set(gca,'xlim',[55927 57754]);
set(gca,'ylim',[-3 3]); % coordinate all
xlabel('Year'), ylabel('nutdx [mas]')
title('IVS-R4 EOP: nutdx')


figure
errorbar(Mjd,Nutdy,DNutdy,'bo')
set(gca,'xTick',[55927 56293 56658 57023 57388 57754]);
```

```
set(gca,'xTicklabel',{'2012','2013','2014','2015','2016','2017'})
set(gca,'xlim',[55927  57754]);
set(gca,'ylim',[-3  3]); % coordinate  all
xlabel('Year'), ylabel('nutdy [mas]')
title('IVS-R4 EOP: nutdy')
```